

# Dark matter search in a Beam-Dump eXperiment (BDX) at Jefferson Lab

*The BDX Collaboration*

M. Battaglieri<sup>\*†</sup>, A. Bersani, B. Caiffi, A. Celentano<sup>†</sup>, R. De Vita<sup>†</sup>, E. Fanchini,  
L. Marsicano, P. Musico, M. Osipenko, F. Panza, M. Ripani, E. Santopinto,  
M. Taiuti

*Istituto Nazionale di Fisica Nucleare, Sezione di Genova  
e Dipartimento di Fisica dell'Università, 16146 Genova, Italy*

V. Bellini, M. Bondí, M. De Napoli<sup>†</sup>, F. Mammoliti, E. Leonora, N. Randazzo,  
G. Russo, M. Sperduto, C. Sutera, F. Tortorici

*Istituto Nazionale di Fisica Nucleare, Sezione di Catania, Catania, Italy*

N. Baltzell, M. Dalton, A. Freyberger, F.-X. Girod, V. Kubarovsky, E. Pasyuk,  
E.S. Smith<sup>†</sup>, S. Stepanyan, M. Ungaro, T. Whitlatch

*Jefferson Lab, Newport News, VA 23606, USA*

E. Izaguirre<sup>†</sup>

*Perimeter Institute for Theoretical Physics, Waterloo, Ontario, Canada, N2L 2Y5*

G. Krnjaic<sup>†</sup>

*Center for Particle Astrophysics, Fermi National Accelerator Laboratory, Batavia, IL  
60510*

D. Snowden-Ifft

*Occidental College, Los Angeles, California 90041, USA*

---

<sup>\*</sup>Contact Person, email: Marco.Battaglieri@ge.infn.it

<sup>†</sup>Spokesperson

D. Loomba

*University of New Mexico, Albuquerque, New Mexico, NM*

M. Carpinelli, V. Sipala

*Università di Sassari e Istituto Nazionale di Fisica Nucleare, 07100 Sassari, Italy*

P. Schuster, N. Toro

*Stanford Linear Accelerator Center (SLAC), Menlo Park, CA 94025, US*

R. Essig

*C.N. Yang Inst. for Theoretical Physics, Stony Brook University, NY*

M.H. Wood

*Canisius College, Buffalo NY 14208, USA*

M.Holtrop, R. Paremuzyan

*University of New Hampshire, Durham NH 03824, USA*

G. De Cataldo, R. De Leo, D. Di Bari, L. Lagamba, E. Nappi, R. Perrino

*Istituto Nazionale di Fisica Nucleare, Sezione di Bari e Dipartimento di Fisica dell'Università, Bari, Italy*

I. Balossino, L. Barion, G. Ciullo, M. Contalbrigo, P. Lenisa, A. Movsisyan,  
F. Spizzo, M. Turisini

*Istituto Nazionale di Fisica Nucleare, Sezione di Ferrara e Dipartimento di Fisica dell'Università, Ferrara, Italy*

F. De Persio, E. Cisbani, F. Garibaldi, F. Meddi, G. M. Urciuoli

*Istituto Nazionale di Fisica Nucleare, Sezione di Roma e Gruppo Collegato Sanità, e Università La Sapienza, Italy*

D. Hasch, V. Lucherini, M. Mirazita, S. Pisano

*Istituto Nazionale di Fisica Nucleare, Laboratori Nazionali di Frascati, P.O. 13, 00044 Frascati, Italy*

G. Simi

*Istituto Nazionale di Fisica Nucleare, Sezione di Padova, Padova, Italy*

A. D'Angelo, L. Lanza, A. Rizzo, C. Schaerf, I. Zonta

*Istituto Nazionale di Fisica Nucleare, Sezione di Roma-TorVergata e Dipartimento di Fisica dell'Università, Roma, Italy*



A. Filippi

*Istituto Nazionale di Fisica Nucleare, Sezione di Torino, Torino, Italy*

S. Fegan

*Institut für Kernphysik, Johannes Gutenberg-Universität Mainz, 55128 Mainz, Germany*

M. Kunkel

*Nuclear Physics Institute and Juelich Center for Hadron Physics, Forschungszentrum  
Juelich, Germany*

M. Bashkanov, P. Beltrame, A. Murphy, G. Smith, D. Watts, N. Zachariou, L. Zana  
*Edinburgh University, Edinburgh EH9 3JZ, United Kingdom*

D. Glazier, D. Ireland, B. McKinnon, D. Sokhan

*University of Glasgow, Glasgow G12 8QQ, United Kingdom*

L. Colaneri

*Institut de Physique Nucleaire d'Orsay, IN2P3, BP 1, 91406 Orsay, France*

S. Anefalos Pereira

*Instituto de Fisica, Universidade de São Paulo, Brasil*

A. Afanasev, B. Briscoe, I. Strakovsky

*The George Washington University, Washington, D.C., 20052*

N. Kalantarians

*Department of Physics, Hampton University, Hampton VA 23668, USA*

L. Weinstein

*Old Dominion University, Department of Physics, Norfolk VA 23529, USA*

K. P. Adhikari, J. A. Dunne, D. Dutta, L. El Fassi, L. Ye

*Mississippi State University, Mississippi State, MS 39762, USA*

K. Hicks

*Ohio University, Department of Physics, Athens, OH 45701, USA*

P. Cole

*Dept. of Physics, Idaho State University, Pocatello, ID 83201 USA*

S. Dobbs

*Northwestern University, Evanston, IL 60208, USA*

C. Fanelli

*Massachusetts Institute of Technology, Cambridge, MA 02139, USA*

## Abstract

MeV-GeV dark matter (DM) is theoretically well motivated but remarkably unexplored. This proposal presents the MeV-GeV DM discovery potential for a  $\sim 1 \text{ m}^3$  segmented CsI(Tl) scintillator detector placed downstream of the Hall A beam-dump at Jefferson Lab, receiving up to  $10^{22}$  electrons-on-target (EOT) in 285 days. This experiment (Beam-Dump eXperiment or BDX) would be sensitive to elastic DM-electron and to inelastic DM scattering at the level of 10 counts per year, reaching the limit of the neutrino irreducible background. The distinct signature of a DM interaction will be an electromagnetic shower of few hundreds of MeV, together with a reduced activity in the surrounding active veto counters. A detailed description of the DM particle  $\chi$  production in the dump and subsequent interaction in the detector has been performed by means of Monte Carlo simulations. Different approaches have been used to evaluate the expected backgrounds: the cosmogenic background has been extrapolated from the results obtained with a prototype detector running at INFN-LNS (Italy), while the beam-related background has been evaluated by GEANT4 Monte Carlo simulations. The proposed experiment will be sensitive to large regions of DM parameter space, exceeding the discovery potential of existing and planned experiments in the MeV-GeV DM mass range by up to two orders of magnitude.

# Contents

<b>1</b>	<b>Introduction</b>	<b>8</b>
<b>2</b>	<b>LDM search in beam-dump experiments</b>	<b>10</b>
2.1	Important Variations . . . . .	13
2.1.1	Inelastic Dark Matter (iDM) . . . . .	13
2.1.2	Leptophilic $A'$ and Dark Matter . . . . .	13
2.2	Muon Anomalous Magnetic Moment . . . . .	14
2.3	Production and Detection . . . . .	14
2.4	Overview of experimental searches . . . . .	17
2.4.1	CMB . . . . .	18
2.4.2	Light Degrees of Freedom . . . . .	19
2.4.3	B-Factories . . . . .	19
2.4.4	High Energy Colliders . . . . .	20
2.4.5	Visible Decays . . . . .	20
2.4.6	Solar Neutrino Bounds . . . . .	20
2.4.7	Missing Energy Experiments . . . . .	20
2.4.8	Direct Detection Experiments . . . . .	21
2.4.9	Beam dump experiments . . . . .	21
2.5	The Unique Capabilities of BDX at JLab . . . . .	23
<b>3</b>	<b>Proposed measurement</b>	<b>25</b>
3.1	The Hall-A beam dump . . . . .	25
3.2	The BDX detector . . . . .	26
3.2.1	The electromagnetic calorimeter . . . . .	27
3.2.2	The active VETO system . . . . .	30
3.2.3	The lead vault . . . . .	31
3.3	Trigger and data acquisition . . . . .	32
3.4	Computing resources . . . . .	34
3.5	The event reconstruction framework . . . . .	35
3.6	A new facility for beam-dump experiments at JLab . . . . .	36
3.6.1	Building and access to detector . . . . .	36
3.6.2	Detector size . . . . .	37
3.6.3	Shielding from the beam dump and overburden . . . . .	38
3.6.4	Cost estimate . . . . .	38
<b>4</b>	<b>Signal and background rates</b>	<b>44</b>
4.1	Simulations of the experimental set-up . . . . .	44
4.2	Signal . . . . .	44

4.2.1	$\chi$ production	45
4.2.2	$\chi$ interaction	46
4.2.3	Detector response	47
4.3	Beam related background	50
4.3.1	Beam-related background for electron recoil	52
4.3.2	Beam-related background for nuclear recoil	55
4.4	Beam unrelated background	56
4.4.1	Cosmic background estimate	56
4.4.2	Background reduction strategies	57
<b>5</b>	<b>Expected results</b>	<b>60</b>
5.1	BDX expected reach	60
5.1.1	Expected signal and measured background	60
5.1.2	The BDX reach	62
5.2	Systematic checks	65
<b>6</b>	<b>Summary and Conclusions</b>	<b>69</b>
<b>A</b>	<b>Evidence and production of dark matter</b>	<b>70</b>
A.1	Generic features of the theory of Light Dark Matter	73
A.2	Defining thermal targets	74
A.3	Excluding scalar mediated direct annihilation	75
A.4	Vector mediated models	76
A.5	LDM candidates with vector mediator	77
<b>B</b>	<b>The BDX prototype</b>	<b>80</b>
B.1	The BDX prototype	81
B.2	Simulation of the BDX prototype	86
B.2.1	The crystal response	87
B.2.2	The IV and OV response	87
B.3	The INFN-CT and LNS configurations	88
B.4	Cosmic muons and cosmic neutrons	90
B.5	Results of cosmogenic background	91
B.5.1	Results from INFN-CT data	91
B.5.2	Results from LNS data	92
B.6	Results of on-beam measurements	96
<b>C</b>	<b>DRIFT-BDX</b>	<b>103</b>
C.1	Capabilities	103
C.2	Detector	103

C.3	Backgrounds . . . . .	105
C.4	Signature . . . . .	108
C.5	Conclusion . . . . .	109
<b>D</b>	<b>Required equipment and future plans</b>	<b>111</b>
D.1	The BDX Collaboration . . . . .	111
D.2	Required equipment . . . . .	111
D.3	Further improvements and tests . . . . .	113
<b>E</b>	<b>Cover letter for BDX proposal submission to PAC44</b>	<b>116</b>

# 1 Introduction

We propose a beam-dump experiment to search for light (MeV-GeV) Dark Matter (DM). DM in this mass range is motivated by both experimental and theoretical considerations. On the theory side, simple extensions to the Standard Model (SM) can accommodate DM-SM interactions that yield the observed DM cosmological abundance. On the experimental side, such models also generically feature particles that explain the currently discrepant value of the muon’s anomalous magnetic moment and resolve anomalies in astrophysical observations, while simultaneously evading cosmological and direct-production constraints.

This experiment could be performed by placing a detector downstream of one of the JLab experimental Halls to detect DM particles that could be produced by the electron beam in the dump, pass through surrounding shielding material, and deposit visible energy inside the detector by scattering off various target particles or — if unstable — by decaying inside the detector volume. A new underground facility placed  $\sim 20m$  downstream of the beam dump of the experimental Hall-A will host the detector, serving as a general-purpose facility for any future beam-dump experiments. The run would be completely parasitic without affecting the normal operations and the physics program of the Hall. The most striking signal that this experiment would look for consists of events with  $\sim$  GeV electromagnetic energy deposition. With the detector and the experimental set-up we are proposing, this signal will be easily detected over a negligible background. This striking signature can arise in two classes of models: in those where DM scatters elastically off atomic electrons in the detector, and in those where the DM can scatter inelastically in the detector and subsequently de-excite in the active detector material into GeV-scale electron pairs, leading to the electromagnetic energy deposition. It will also be possible to detect the small signal produced by a light DM particle scattering off a nucleon. However the detection thresholds need to be fixed at values as low as possible ( $\sim$  MeV), where spurious signals from beam-related (neutrinos) and cosmogenic (muons, neutrons and neutrinos) backgrounds limit the measurement sensitivity of the DM-nucleon scattering channel. Nevertheless sensitivity to a broad range of possible DM interactions could provide a tool for systematic and consistency checks.

The physics motivation for light DM is presented in Sec. 2 and, for completeness, more details are reported in Appendix A. Also in Sec. 2, we describe the uniqueness of BDX to test a wide class of DM models and how its sensitivity can exceed that of other experiments proposed at FNAL, CERN, and LNF. Section 3 describes the proposed experimental set-up: the Hall-A beam-dump, the detector, the data acquisition, the off-line analysis and the proposed new underground facility downstream of the dump. Section 4 describes the model for DM production in the dump and DM interaction in the detector as well as detailed estimates of beam unrelated (cosmo-

genic) and beam-related backgrounds. Cosmogenic backgrounds have been evaluated extrapolating results obtained in a dedicated measurement performed at INFN-LNS with a prototype of the BDX detector. All details are reported in Appendix B. Beam-related background estimates were based on GEANT4 Monte Carlo simulations of the beam interaction in the Hall-A beam-dump and the downstream shielding. Projections, counting rates for signal and background, and the expected reach of BDX are reported in Sec. 5. Finally, an alternative detection technology based on a gaseous TPC (the DRIFT-BDX detector) is described in Appendix C. We illustrate how a prototype that fits in the new proposed facility would complement the main BDX detector, elaborate on the detection concept and show how it could provide powerful cross-checks on backgrounds in the beam dump lab.

## 2 LDM search in beam-dump experiments

In this section we motivate the search for sub-GeV light Dark Matter (LDM) using an electron beam at Jefferson Lab. The theoretical viability of LDM as well as a more thorough description of the simple models that can accommodate all existing data are presented in Appendix A. In this proposal, we focus on models of LDM where LDM has non-gravitation interactions with the Standard Model (SM). These additional interactions are responsible for generating the correct DM abundance through the well known mechanism of thermal freeze-out [1].

The requirement of a thermal origin is a strict requirement on LDM models, as it sets a *minimum* interaction strength between DM and the SM. Combined with the requirement to only consider extensions of the SM that respect the known SM symmetries, the model parameter space in the paradigm of thermal-origin DM greatly simplifies. By and large the most viable model of LDM for exploration is that where LDM interacts with the SM through a “dark photon”,  $A'$ . The dark photon,  $A'$ , kinetically-mixes with the Standard Model (SM) hypercharge. LDM particles, denoted by Dirac-fermions  $\chi$  and  $\bar{\chi}$  for concreteness, are produced via the real or virtual decay of the  $A'$ . Note that the phenomenology discussed below is equally applicable to spin 0 LDM as well.

We use this scenario as the basis for studying the sensitivity of the experiment. The Lagrangian for this setup is [2]

$$\mathcal{L}_{A'} \supset -\frac{1}{4}F'_{\mu\nu}F'^{\mu\nu} + \frac{\epsilon_Y}{2}F'_{\mu\nu}B_{\mu\nu} + \frac{m_{A'}^2}{2}A'_\mu A'^\mu + g_D A'_\mu J_\chi^\mu + g_Y B_\mu J_Y^\mu, \quad (1)$$

where  $F'_{\mu\nu} \equiv \partial_\mu A'_\nu - \partial_\nu A'_\mu$  is the dark photon field strength,  $B_{\mu\nu} \equiv \partial_\mu B_\nu - \partial_\nu B_\mu$  is the hypercharge field strength,  $g_D \equiv \sqrt{4\pi\alpha_D}$  is the dark gauge coupling, and  $J_\chi^\mu$  and  $J_Y^\mu$  are the DM and SM hypercharge matter currents, respectively. After electroweak symmetry breaking, the kinetic mixing term, proportional to  $\epsilon_Y$ , induces mixing with the photon and  $Z$  boson

$$\frac{\epsilon_Y}{2}F'_{\mu\nu}B_{\mu\nu} \longrightarrow \frac{\epsilon}{2}F'_{\mu\nu}F_{\mu\nu} + \frac{\epsilon_Z}{2}F'_{\mu\nu}Z_{\mu\nu}, \quad (2)$$

where  $\epsilon \equiv \epsilon_Y \cos\theta_W$ ,  $\epsilon_Z \equiv \epsilon_Y \sin\theta_W$ , and  $\theta_W$  is the weak mixing angle. As a result, we get dark photon interactions with dark and visible matter

$$g_D A'_\mu J_\chi^\mu + g_Y B_\mu J_Y^\mu \longrightarrow A'_\mu (g_D J_\chi^\mu + \epsilon e J_{\text{EM}}^\mu), \quad (3)$$

where  $J_{\text{EM}}^\mu$  is the usual SM electromagnetic current and we have omitted terms higher order in  $\epsilon$ . The phenomenological features of this model are:

- The SM fermions acquire an effective “milli-charge” under the short-range force carried by  $A'$ , namely  $\epsilon e$ .



- The phenomenology in the LDM sector will depend on how DM couples to  $A'$ , *i.e.*, what is the dark current  $J_\chi^\mu$ . Two broad categories could ensue: DM couples to  $A'$  *diagonally*, or *off-diagonally*. For instance, if DM is a spin 1/2 fermion, as written in Eq. 1, these two categories correspond to whether DM is Dirac or Majorana, respectively. For Dirac-like DM, DM, which we denote also by  $\chi$ , can be produced along with its antiparticle,  $\bar{\chi}$ , through on-shell or off-shell production of  $A'$ . In the Majorana scenario, the DM, now represented by  $\chi_1$ , is produced along with an excited state  $\chi_2$  also through the  $A'$ . We will focus on these two categories separately, as they lead to distinct signatures. We note that the phenomenological signatures we focus on are quite generic, as they also can be realized in the case where DM is a spin 0 boson as well. We discuss these scenarios in more detail in Appendix A.

In the paradigm of a thermal origin for DM, DM would have acquired its current abundance through annihilation directly/indirectly into the SM. Here, we focus on the direct annihilation regime, in which  $m_\chi < m_{\text{MED.}}$ , where  $m_{\text{MED.}}$  would correspond to  $m_{A'}$  in the model we are focusing on (see Appendix A for more details). The annihilation rate scales as (see Fig. 1)

$$(\text{“direct” annihilation}) \quad \langle \sigma v \rangle \sim \frac{g_D^2 g_{\text{SM}}^2 m_\chi^2}{m_{\text{MED}}^4}, \quad (4)$$

and offers a clear, predictive target for discovery or falsifiability since the dark coupling  $g_D$  and mass ratio  $m_\chi/m_{\text{MED}}$  are at most  $\mathcal{O}(1)$  in this  $m_{\text{MED}} > m_\chi$  regime, so there is a *minimum* SM-mediator coupling compatible with a thermal history; larger values of  $g_D$  require non-perturbative dynamics in the mediator-SM coupling or intricate model building.

In the direct annihilation regime, up to order-one factors, the minimum annihilation rate requirement translates into a minimum value of the dimensionless combination

$$y \equiv \frac{g_D^2 g_{\text{SM}}^2}{4\pi} \left( \frac{m_\chi}{m_{\text{MED}}} \right)^4 \gtrsim \langle \sigma v \rangle_{\text{relic}} m_\chi^2, \quad (5)$$

which, up to order one factors, is valid for every DM/mediator variation provided that  $m_{\text{DM}} < m_{\text{MED.}}$ . We will use this target throughout this document to assess experimental sensitivity to various LDM scenarios; reaching at least this benchmark sensitivity is necessary to discover or falsify a large class of simple direct annihilation models.

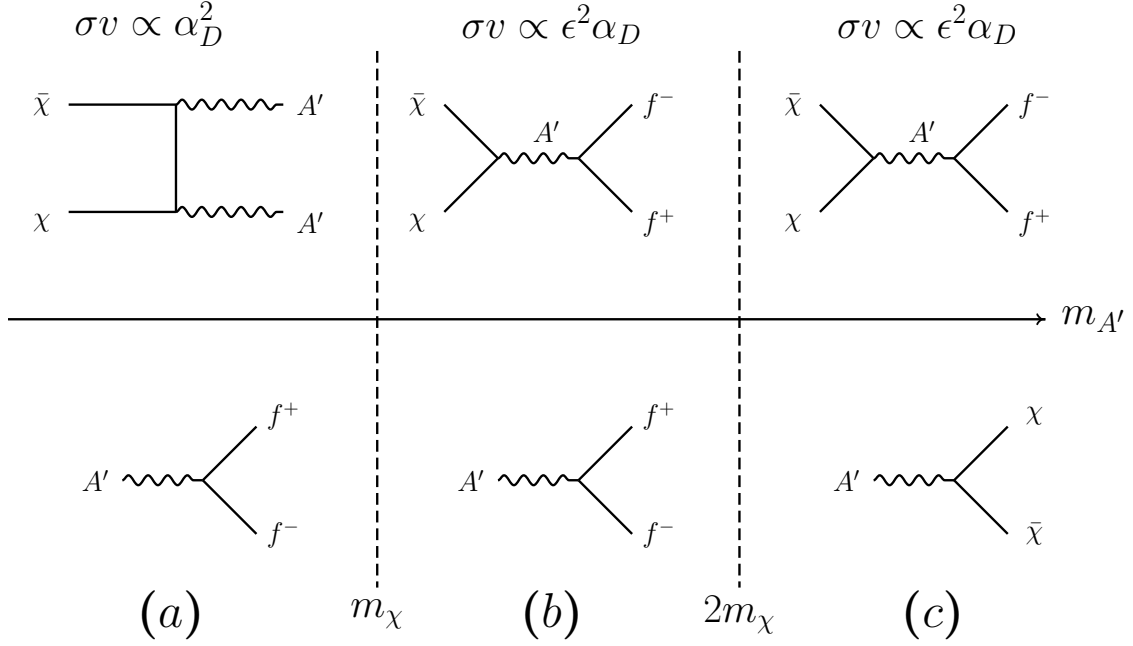
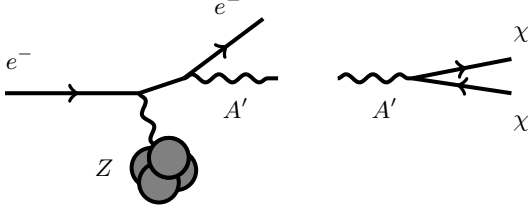


Figure 1: Classification of dominant DM annihilation and mediator decay channels in the benchmark dark photon ( $A'$ ) mediated scenario for different  $m_{A'}/m_{\chi}$  ratios where  $f$  is a charged SM fermion – similar categorizations exist for other mediators. Also, the same classification holds for Majorana-DM, with the substitution  $(\chi, \bar{\chi}) \rightarrow (\chi_1, \chi_2)$ . **(a)** In the left column, the mediator is lighter than the DM, so for  $\epsilon \ll g_D$  the dominant annihilation is in the “secluded” channel, which is independent of the mediator coupling to the SM. This scenario has no direct thermal target; every arbitrarily small values of  $\epsilon$  are compatible with a thermal annihilation rate. **(b)** The middle column represents the  $m_{\chi} < m_{A'} < 2m_{\chi}$  window in which the annihilation rate is sensitive to  $\epsilon$  but the mediator decays visibly. This regime has a predictive thermal relic target, which can be tested by probing sufficiently small values of  $\epsilon$  in searches for visibly decaying dark photons (e.g. HPS, APEX, Belle II). **(c)** The right column where  $m_{A'} > 2m_{\chi}$  offers ample parameter space with a predictive thermal target and features mediators that decay *invisibly* to DM states. Since  $\sigma v \propto \epsilon^2 \alpha_D$  this scenario has a thermal target which can be probed by testing sufficiently small values of this combination at BDX, whose signal yield scales as the same combination of input parameters.

## $A'$ Production in Target



## DM Scattering in Detector

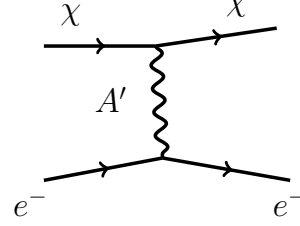


Figure 2: a)  $\chi\bar{\chi}$  pair production in electron-nucleus collisions via the Cabibbo-Parisi radiative process (with  $A'$  on- or off-shell) and b)  $\chi$  scattering off an electron in the detector.

## 2.1 Important Variations

### 2.1.1 Inelastic Dark Matter (iDM)

If the  $A'$  couples to a DM fermion with both Dirac and Majorana masses, the leading interaction is generically off-diagonal and

$$A'_\mu J_{DM}^\mu \rightarrow A'_\mu \bar{\chi}_1 \gamma^\mu \chi_2, \quad (6)$$

where the usual Dirac fermion  $\chi$  decomposes into two Majorana (“pseudo-Dirac”) states  $\chi_{1,2}$  with masses  $m_{1,2}$  split by an amount  $\Delta$ . This kind of scenario is well motivated for LDM which is safe from CMB constraints [3], and has striking implications for possible signatures at BDx.

### 2.1.2 Leptophilic $A'$ and Dark Matter

A similar scenario involving a vector mediator arises from gauging the difference between electron and muon numbers under the abelian  $U(1)_{e-\mu}$  group. Instead of kinetic mixing, the light vector particle here has direct couplings to SM leptonic currents

$$A'_\beta J_{SM}^\beta \rightarrow g_V A'_\mu (\bar{e} \gamma^\beta e + \bar{\nu}_e \gamma^\beta \nu_e - \bar{\mu} \gamma^\beta \mu + \bar{\nu}_\mu \gamma^\beta \nu_\mu), \quad (7)$$

where  $g_V$  is the gauge coupling of this model, which we normalize to the electric charge,  $g_V \equiv e$  and consider parameter space in terms of  $e$ , like in the case of kinetic mixing. Note that here, the  $A'$  does not couple to SM quarks at tree level, but it does couple to neutrinos, which carry electron or muon numbers. Note also that this scenario is one of the few combinations of SM quantum numbers that can be gauged without requiring additional field content. Assigning the DM  $e - \mu$  number yields the

familiar  $g_D A'_\beta J_{\text{DM}}^\beta$  interaction as in Eq. 1. Both of these variations can give rise to thermal LDM as discussed above.

## 2.2 Muon Anomalous Magnetic Moment

It is well known that a light, sub-GeV scale gauge boson (either a kinetically mixed dark photon, or a leptophilic gauge boson that couples to muons) can ameliorate the  $\sim 3.5\sigma$  discrepancy between the theoretical prediction and experimental observation of the muon's anomalous magnetic moment [4]. Although there are many active efforts to search for dark photons independently of their connection to dark matter, the success of these efforts relies on the assumption that the  $A'$  is the lightest particle in its sector and that its primary decay channel only depends on  $\epsilon$ . Furthermore, if the  $A'$  decays predominantly to SM particles, this explanation of the  $(g-2)_\mu$  anomaly has been ruled out (see discussion in Sec. 5).

If, however, the  $A'$  couples to a light DM particle  $\chi$  ( $m_{A'} > m_\chi$ ), then the parameter space for reconciling theory and experiment with regard to  $(g-2)_\mu$  remains viable. For large values of  $\alpha_D$ , this explanation of the anomaly is under significant tension with existing constraints, but for  $\alpha_D \ll \alpha_{\text{EM}}$  this explanation is still viable and most of the remaining territory can be tested with BDX@JLab (see discussion in Sec. 5).

In the remainder of this section, we review the salient features of LDM production at an electron fixed-target facility. Secondly, we give an overview of the status of LDM models parameter space, and the capabilities of present, and near future proposals to make progress in the field. Finally, we highlight how BDX uniquely fits in this developing field.

## 2.3 Production and Detection

Whether the dark sector is quite simple or has a rich structure of light particles, the fixed-target phenomenology of stable  $\chi$ s (or unstable  $\chi$ s with lab-frame lifetimes  $\gtrsim \mu\text{s}$ ) is well-described by the simplest case — the Lagrangian from Eq. 1. Here the label  $\chi$  could refer to scalar or fermion LDM, with diagonal or off-diagonal couplings to  $A'$ .

In this theory,  $\chi$ s can therefore be pair-produced radiatively in electron-nucleus collisions in the dump (see Fig. 2a). A fraction of these relativistic particles then scatter off nucleons, nuclei, or electrons in the detector volume (see Fig. 2b), positioned downstream from the dump or target.

If  $m_{A'} < 2m_\chi$ , the dominant  $\chi$  production mechanism in an electron fixed-target experiment is the radiative process illustrated in Fig. 2a) with off-shell  $A'$ . In this regime, the  $\chi$  production yield scales as  $\sim \alpha_D \epsilon^2 / m_\chi^2$  ( $\alpha_D \equiv g_D^2 / 4\pi$ ), while  $\chi$ -nucleon

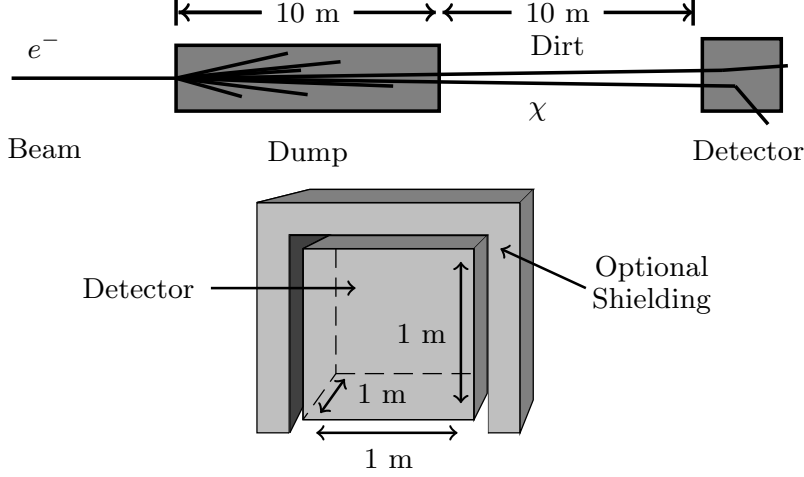


Figure 3: Schematic of the experimental setup. A high-intensity multi-GeV electron beam impinging on a beam-dump produces a secondary beam of dark sector states. In the basic setup, a small detector is placed downstream with respect to the beam-dump so that muons and energetic neutrons are entirely ranged out.

scattering in the detector via  $A'$  exchange (see Fig. 2b)) occurs with a rate proportional to  $\alpha_D \epsilon^2 / m_{A'}^2$  over most of the mass range. Thus, the total signal yield scales as

$$N_\chi \sim \frac{\alpha_D^2 \epsilon^4}{m_\chi^2 m_{A'}^2}. \quad (8)$$

If  $m_{A'} > 2m_\chi$ , the secondary  $\chi$ -beam arises from radiative on-shell  $A'$  production followed by  $A' \rightarrow \bar{\chi}\chi$  decay. In this regime, the  $\chi$  production and the detector scattering rates are respectively proportional to  $\epsilon^2 / m_{A'}^2$  and  $\alpha_D \epsilon^2 / m_{A'}^2$ , and the signal yield scales as

$$N_\chi \sim \frac{\alpha_D \epsilon^4}{m_{A'}^4}. \quad (9)$$

Thus, for each  $\alpha_D$  and  $m_{A'}$ , we can extract an  $\epsilon$ -sensitivity corresponding to a given scattering yield.

A generic sketch of a beam dump experiment is shown in Fig. 3, where the DM particles are produced in the beam dump and traverse unimpeded through sufficient material that eliminates all SM particles aside from neutrinos. They then scatter in the shielded detector downstream. The experimental signal is an electromagnetic

shower induced by  $\chi$ -electron scattering. Because the electron is light and the  $\chi$  are energetic, scattered electrons typically carry GeV-scale energy and are therefore subject to much lower backgrounds than nucleon scattering. Figure 4 shows the lepton recoil energy for different choices of  $M_\chi$  and  $M_{A'}$ . Indeed, for models with kinetically mixed mediators which produce both electron- and nucleon-scattering signals, electron-recoil searches at BDX will have the greatest sensitivity. As such, the experimental detection of the low-energy scattered nucleons is a secondary goal of the experiment because it provides an alternative probe of LDM production and is sensitive to some models that have distinctive signals primarily in nucleon-scattering. However, backgrounds from cosmic-ray neutrons are expected to limit the sensitivity in this channel.

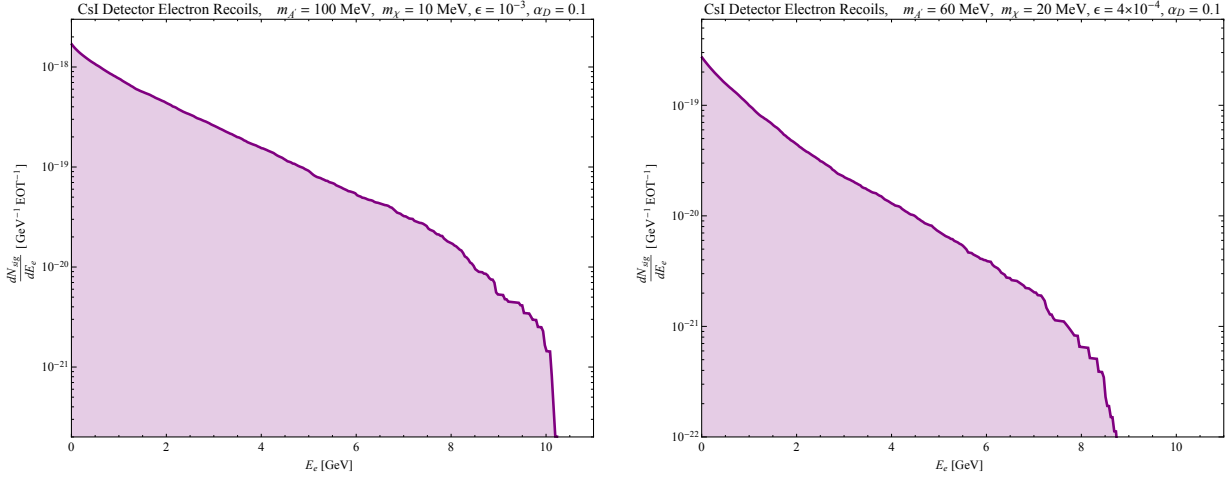
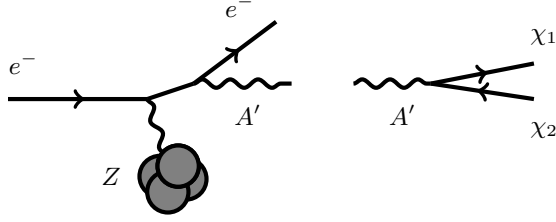


Figure 4: Signal energy distributions of scattered electrons for the two choices of  $M_\chi$  and  $M_{A'}$ . The distributions are based on a simulated population of  $\chi$  particles after applying geometric acceptance.

To close this discussion of dark matter models and their signals, we comment on the simple and well-motivated case of majorana LDM with off-diagonal couplings. In this scenario, (a) the electron beam produces  $\chi_1\chi_2$  pairs, (b) for sufficiently large mass splittings  $\Delta \equiv m_2 - m_1$ , the  $\chi_2$  decays to  $\chi_1 e^+ e^-$  inside the detector, and (c) the  $\chi$ -scattering processes in the detector are inelastic (e.g.  $\chi_1 p \rightarrow \chi_2 p$ ), with a total deposited energy that is often dominated by the energetic  $e^+ e^-$  pair from the subsequent  $\chi_2$  decay. Like the electron scattering process, this inelastic scattering signal can be searched for with very low background rates. Fig. 5 illustrates the production and detection signature of models of majorana LDM.

## $A'$ Production in Target



## iDM Scattering in Detector

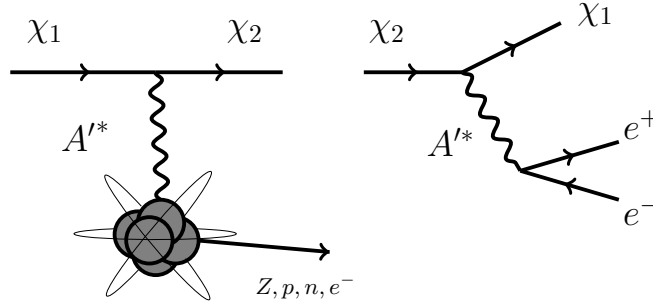


Figure 5: Top: Same as Fig. 2, but for an *inelastic* Majorana DM scenario in which the  $A'$  decays to a pair of different mass eigenstates. The unstable  $\chi_2$  decays in flight, so the flux at the detector is dominated by  $\chi_1$  states which upscatter off electron, nucleon, and nuclear targets (bottom) to regenerate the  $\chi_2$  state. Subsequently, the  $\chi_2$  promptly de-excites in a 3-body  $\chi_2 \rightarrow \chi_1 e^+ e^-$  process, depositing significant  $\sim$  GeV scale electromagnetic signal inside the BDX detector.

## 2.4 Overview of experimental searches

In this section, we discuss current and near future experimental programs and highlight the uniqueness of BDX at JLab. The search for LDM covers the space represented by two masses ( $m_{A'}$  and  $m_\chi$ ) and two couplings ( $\alpha_D$  and  $\epsilon$ ), an example of which is shown in Fig. 6. The colored areas have been ruled out by various experiments, but leave open regions which can be probed by BDX. Moreover, Fig. 7 illustrates some of the parameter space in LDM models that can still explain the discrepant value of  $(g - 2)$  of the muon, in particular the  $m_{A'} \gg m_\chi$  and  $\alpha_D \gg \epsilon$  regime.

In the following we describe the various searches and comment on their sensitivity.

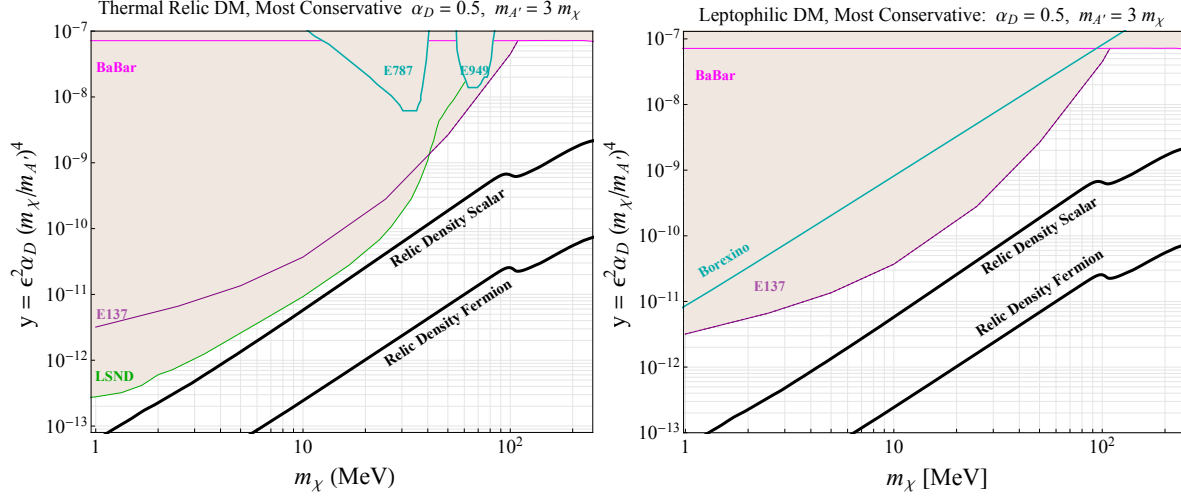


Figure 6: Example of the viable parameter space for light dark matter in the representative kinetically-mixed and leptophilic scenarios alongside appropriate constraints. The parameter space is characterized by two masses ( $m_{A'}$  and  $m_\chi$ ), the coupling of the  $A'$  to the LDM particle  $\chi$ ,  $\alpha_D$ , and the kinetic mixing represented by  $\epsilon$ . The “ $y$ ” variable on the vertical axis is chosen because it is proportional to the annihilation rate, so the thermal target (solid black) is fixed for a given choice of  $m_\chi$ . As we will see, for low background rates, BDX becomes sensitive to unexplored regions of the parameter space.

The paradigm of DM interactions with the SM offers three broad possibilities to search for it: accelerators, direct, and indirect detection. The first relies on production of DM, either directly, or through the production and decay of a mediator such as the  $A'$ . The second approach seeks to directly detect the interaction of DM particles from the halo, as they pass through the earth. In the third, DM annihilation in the early Universe could affect cosmological observations; or alternatively, in the present day, DM could annihilate in dense regions such as the center of our galaxy — giving rise to final state SM particles that one can look for. We briefly discuss previous, current, and near-future efforts in the search for LDM. For more details, see Ref. [3].

#### 2.4.1 CMB

While DM annihilation freezes out before the era of recombination, residual annihilations can re-ionize hydrogen and distort the high- $\ell$  CMB power spectrum [5, 6, 7, 8, 9]. These data can be used to constrain the total power injected by DM annihilations [9], which scales as the DM annihilation cross-section (hence proportional to  $y$ ) and can be invariantly compared with the relic density target. Dirac fermion DM annihilating



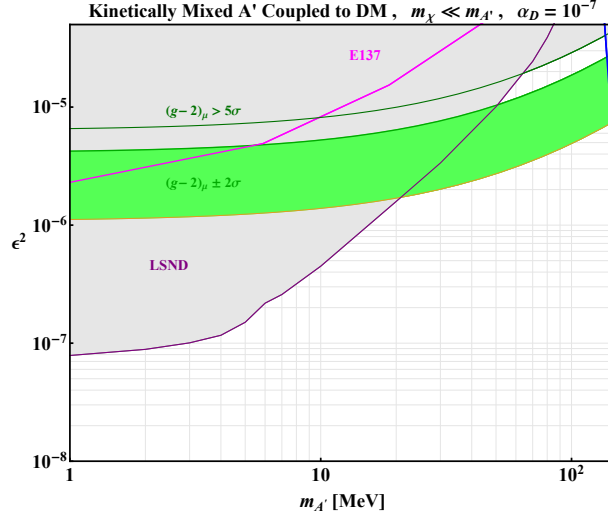


Figure 7: Viable parameter space for sub-GeV DM coupled to a kinetically mixed  $A'$  for  $\alpha_D \ll \epsilon$ . Here,  $\alpha_D \equiv g_D^2/4\pi$ , where  $g_D$  is the DM coupling to the mediator. The green band represents the parameter space that can explain  $g - 2$  of the muon.

through an  $s$ -channel  $A'$  is ruled out by Planck 2015 data [10], but the other scenarios remain viable. In particular, the Majorana LDM scenario is viable because the DM annihilation rate during the CMB epoch is sharply suppressed relative to its value at freeze out, and the scalar DM scenario is allowed because annihilation in this case is suppressed by the DM velocity  $v^2$ , *e.g.*, p-wave annihilation.

#### 2.4.2 Light Degrees of Freedom

There is an indirect bound on light DM  $\lesssim 10$  MeV that remains in thermal equilibrium with SM radiation (but not neutrinos) during BBN [11]. This bound is more model dependent than accelerator probes because it can be evaded with additional sources of dark sector radiation (*e.g.* sterile neutrinos).

#### 2.4.3 B-Factories

Mono-photon and missing-energy production at B-factories sets a limit on models of LDM. The BaBar search for an (untagged)  $\Upsilon(3S) \rightarrow \gamma + \text{invisible}$  [12] constrains the process  $e^+e^- \rightarrow \gamma + A'^{(*)} \rightarrow \gamma\chi\bar{\chi}$  [13, 14]. Since the  $A'$  production rate only depends on  $\epsilon$  and the beam energy, one must make a choice for  $m_\varphi/m_{A'}$  and  $\alpha_D$  to build the  $y$  variable using these data; smaller choices of either quantity would overstate the BaBar constraint.

#### 2.4.4 High Energy Colliders

Electroweak precision tests at LEP can constrain the existence of a new massive photon. In particular, kinetic mixing induces a shift in the mass of the  $Z^0$  boson, and the constraint depends on  $\epsilon$  and only mildly on  $m_{A'}$  [15, 16]. At the LHC, light DM can be produced in association with a QCD jet. Recasting a CMS DM search [17] in the monojet and missing energy channel places a constraint on the  $y$  vs.  $m_\chi$  plane. These constraints do not scale with  $y$  so one must choose a specific value of  $m_\chi/m_{A'}$  and  $\alpha_D$  in constructing  $y$  for colliders.

#### 2.4.5 Visible Decays

Direct searches for the new mediator, *resonance searches* of Mediator  $\rightarrow$  SM SM, can also target models of LDM. This realm can arise in a model where the mass hierarchies are  $m_{\text{DM}} > m_{A'} > m_{e^\pm}$  or whenever  $\epsilon \gg g_D$ . Many experiments have been performed searching for an  $A'$  boson with mass in the range 1 – 1000 MeV and coupling,  $\epsilon$ , in the range  $10^{-5} - 10^{-2}$ . Several different and complementary approaches were proposed (for a summary, see [18] and references therein), and indeed JLab has a strong presence with APEX [19], HPS [20], and DarkLight [21].

#### 2.4.6 Solar Neutrino Bounds

If the  $A'$  is a leptophilic gauge boson that also couples to neutrinos (e.g. as the mediator of a  $U(1)_{e-\mu}$  gauge group, or similar variations including  $U(1)_{\mu-\tau}$  or  $U(1)_{B-L}$  which are in the same class of models), it can affect the rate of solar neutrino scattering in the Borexino detector [22]. This constraint is shown in Fig. 7 (bottom) in the context of the  $U(1)_{e-\mu}$  model.

#### 2.4.7 Missing Energy Experiments

A recently proposed experiment at CERN SPS [23, 24], now known as NA64, would also search for invisible  $A'$  decay. The experiment employs an innovative technique, by having the primarily  $e^-$  beam from the SPS, with energy between 10 and 300 GeV, impinging on an *active* beam-dump, made by a calorimeter based on scintillating fibers and tungsten, ECAL1. An almost-hermetic detector would be located behind the active beam-dump. The detector is made by a charged particle veto counter, a decay volume, two scintillating fiber counters, a second electromagnetic calorimeter ECAL2, and an hadronic calorimeter. The primary goal of the experiment is to search for the  $A'$  production in the active dump through a Brehmstrahlung-like process, followed by the decay to  $e^+e^-$ . The signature for these events is a signal in ECAL1 and two clusters in ECAL2, from the  $A'$  decay products. The same experiment, could

also search for  $A'$  invisible decays by exploiting the detector hermeticity, and requiring a single hit in ECAL1 from the  $e^-$  radiating the  $A'$ . The projected sensitivity for  $3 \cdot 10^{12}$  electrons makes this experiment one of BDX's direct competitors for search of LDM with diagonal couplings to  $A'$ .

Note, however, that the case of Majorana LDM (off-diagonal couplings) can be problematic for missing energy experiments, because the DM signal in this scenario,  $e^- + \text{target} \rightarrow e^- + \text{target} + \chi_1 \chi_2$  with  $\chi_2$  later decaying to  $\chi_1 e^+ e^-$ , is mimicked precisely by their most problematic background from the reaction  $e^- + \text{target} \rightarrow e^- + \text{target} + \gamma$  with  $\gamma$  converting to  $e^+ e^-$  in their detector.

A class of experiments that looks for missing mass from the reaction  $e^+ + e^- \rightarrow \gamma + (A' \rightarrow \bar{\chi} \chi)$  originating from a positron beam have been proposed at both Frascati and at Cornell [25]. While this signature is a rather clean one, namely a bump search, these experiments are limited to energies and rates that may limit their ability to constraint parameter space consistent with DM's current abundance [26].

#### 2.4.8 Direct Detection Experiments

Elastic DM-nuclear interactions are constrained by recent results from CRESST [27], whose low threshold allows for sensitivity down to a few 100s of MeV in DM mass. New ideas for direct detection of DM off of electrons have been proposed in recent years however, and while these searches are currently background-limited [28, 29], new techniques have the potential to in principle also target the thermally-motivated parameter space of light DM that BDX can access for elastically-scattering DM. However, for majorana LDM, the sensitivity of direct detection experiments is quite limited. This is because tree-level scattering is inelastic and kinematically forbidden for mass splittings of order  $\Delta \gtrsim \text{KeV}$ ; elastic scattering arises from a one-loop box diagram which scales as  $y^2$  and is also invariant on the  $y$  vs.  $m_\chi$  plane.

#### 2.4.9 Beam dump experiments

We now discuss beam-dump experiments. First we focus on results from the re-analysis of old data, and later on a current effort at a proton-beam-dump experiment.

##### Reanalysis of old data

The considerable sensitivity of beam-dump experiments to light dark matter is underscored by the reach of existing neutrino experiments [30, 31, 32, 33, 34]. For example, the LSND measurement of electron-neutrino scattering [35] can be used to derive the most stringent constraints to date on the parameter space for invisibly-decaying dark mediators that couple to both baryons and leptons [31]. That experi-

ment delivered  $\sim 10^{23}$  800 MeV protons to the LANSCE beam-dump. For very low mass  $A'$ s and dark matter sufficiently light ( $100\text{MeV} \lesssim m_{A'} \lesssim 2m_\chi$ ), the produced neutral pions have a small exotic decay into  $A'$ s which then decay to  $\chi$ . The  $\chi$  can then scatter off electrons in the LSND detector via  $A'$ -exchange. However, the sensitivity of LSND vanishes if the mediator couples only to leptons or baryons and is weakened if its coupling to either is suppressed.

Recently it was shown that electron-beam fixed target experiments could offer powerful sensitivity to a broad class of dark sector scenarios with particle dark matter in the MeV – GeV mass range [13, 36, 22]. Electron beam-dump experiments are complementary to dedicated efforts at proton beam facilities, have comparable DM scattering yield, can run parasitically and on a smaller scale than proton-beam counterparts, and benefit from negligible beam-related backgrounds. Such searches can dramatically improve sensitivity to MeV-to-GeV mass dark matter and other long-lived weakly coupled particles, extending well beyond the reach of proposed neutrino-factory experiments and Belle-II projections. The power of electron beam dump experiments in this context is illustrated by the existing sensitivity of the SLAC E137 experiment [37]. That experiment was sensitive to invisibly decaying dark mediators produced in fixed target collisions involving 20 GeV electrons and the E137 beam-dump [38]. Despite the rather high energy threshold ( $\sim 3$  GeV) required to see secondary scattering of dark matter particles off electrons, and the small geometric acceptance, E137 has already probed mediator mixings beyond that probed by proton beam-dumps at intermediate masses. In a year of parasitic running, BDX will receive roughly 100 times the charge deposited on E137, with a comparable solid angle, higher-density detector, and lower energy threshold.

## Current beam-dump experiments

The MiniBooNE experiment, originally designed to study neutrino oscillations, recently completed a test run to demonstrate the feasibility for MeV DM [33] search. In the experiment, the primary 8.9 GeV proton beam from the FNAL accelerator impinged on a 50-m long iron beam-dump. Dark matter particles are produced through neutral mesons decay ( $\pi^0, \eta$ ), where one of the photons converts to an  $A'$  that, in turns, decays to a  $\chi\bar{\chi}$  pair. These particles can then scatter on the electrons or nuclei in the MiniBooNE detector, placed 490 m downstream the beam-dump. The otherwise dominant neutrinos background, generated by charged mesons decay in flight, was reduced by a factor of  $\simeq 70$  directing the proton beam straight on the dump, instead of the original beryllium target. With the support of the FNAL PAC, MiniBoone is currently seeking to collect  $\sim 10^{20}$  protons on target in this beam-dump mode and will continue taking data in this mode this year.

## 2.5 The Unique Capabilities of BDX at JLab

While the field of light DM interacting with the SM is making rapid progress, BDX at JLab offers a series of unique possibilities unmatched by proposed competitors. First, thanks to the world-leading capability of CEBAF’s intense beam, electron beam-dump experiments have the potential to reach ever smaller couplings between the mediator and the SM thanks to the luminosities offered by JLab’s Hall A or C — this is unmatched by any of the potential competitors that feature an electron beam with an energy in the few-GeV range. As to proton beam-dump experiments, electron beams offer comparable signal yields and do not suffer from the same level of neutrino backgrounds that proton beam-dump experiments do. In particular, BDX could improve the sensitivity over LSND for LDM masses above the  $m_{\pi^0}/2$  threshold. Importantly however, in a real sense, electron beam-dump experiments target parameter space that’s orthogonal to that probed by proton beam-dump experiments, as the former are sensitive to models with  $A'$  with leptophilic couplings. Similarly, proton beam-dumps have the ability to uniquely probe leptophobic models.

It is important to mount beam dump searches even when electron-scattering direct detection experiments may constrain overlapping parameter space. First, we re-iterate that direct detection experiments using noble-liquid detectors are currently background-limited, while semiconductor-based detectors still need to demonstrate sensitivity to detecting the expected single- or few-electron events from DM-electron scattering. It therefore still needs to be demonstrated that direct detection can indeed cover thermal-origin motivated DM parameter space. In the event that these new techniques do achieve their potential, we actually view it as a strength of this program that a discovery in an accelerator-based experiment could also be observed by a direct detection counterpart. In fact, this multi-pronged approach is recognized as being essential in searching for Weak-scale WIMPs. Moreover, there is a class of models that each technique is uniquely suited for. For example, the Majorana DM scenario described above is a strength of BDX and a weakness of direct detection. In this class of models, the ground state  $\chi_1$  is unable to upscatter into the excited state  $\chi_2$  for mass splittings  $\Delta$  above some KeV, thereby shutting off the leading interaction at direct detection experiments. Conversely, models of ultralight DM are a particular strength of direct detection. Therefore, the two approaches must be seen as complementary in nature.

Even within electron-beam accelerator experiments, a beam-dump setup can offer superior sensitivity to Majorana DM models than missing energy/mass experiments, despite the signal yields for the latter scaling more favourably ( $\epsilon^2$  vs  $\epsilon^4\alpha_D$  for missing energy/mass and beam-dump, respectively). For missing energy experiments, production of DM in the active target would proceed via  $e^- + N \rightarrow e^-(A' \rightarrow \chi_1\chi_2)$ . The de-excitation of the  $\chi_2$  inside the active detector from the reaction  $\chi_2 \rightarrow \chi_1\ell\ell$  would

mimic the most problematic background for that class of experiments: bremsstrahlung events with a photon converting to  $e^+e^-$ . In contrast, at a beam-dump experiment, the  $\chi_1$  produced in the dump could upscatter in the detector via the reaction  $\chi_1 + \text{target} \rightarrow \chi_2 + \text{target}$ . If the excited state de-excites inside BDX, that would lead to an even more striking signal — one recoil-target such as an electron, nucleus or nucleon, and the two electrons from the de-excitation from  $\chi_2$ .

Moreover, the sensitivity of BDX for LDM with diagonal couplings is competitive with the projected reach of NA64’s most advanced phase of running, proposed by NA64 to start running no earlier than in 2020 [39] — although not approved by CERN yet.

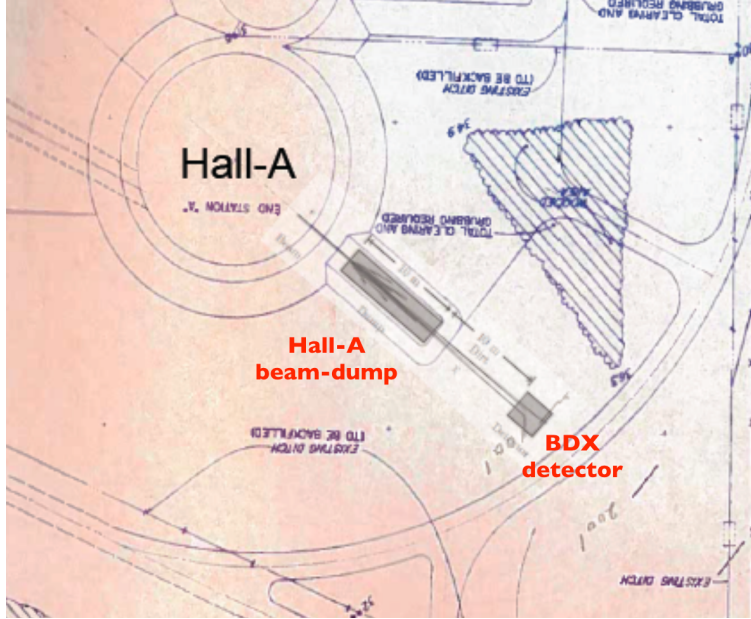


Figure 8: The possible location of BDX detector at  $\sim 20\text{m}$  from the Hall-A beam dump.

### 3 Proposed measurement

The proposed experiment would require a  $1\text{ m}^3$ -scale detector volume, located  $\sim 20$  meters downstream of the dump of a high-intensity multi-GeV electron beam, and could run parasitically. We studied in detail the option of a new underground facility located downstream of the Hall-A beam dump. See Fig. 8 for a schematic representation of the experimental setup. BDX will use the electron scattering of a DM  $\chi$  particle in a state-of-the-art electromagnetic calorimeter with excellent forward geometric acceptance, to greatly extend dark matter sensitivity beyond that available to the high threshold/low acceptance E137 setup or to existing proton beam-dumps. Being also sensitive to low-energy nuclear recoil, BDX will use it as cross check of any possible findings. The approach makes good use of Jefferson Lab upgrade to 11 GeV energies with the new CEBAF scheduled to deliver up to about  $65\mu\text{A}$  currents.

#### 3.1 The Hall-A beam dump

The Hall-A at JLab is expected to receive from CEBAF a 11 GeV electron beam with a maximum current of about  $65\mu\text{A}$ . The maximum available energy that focus the  $\chi$  beam towards the detector together with a sizeable current that allows to collect the desired charge in the shortest amount of time, makes the Hall-A the optimal choice



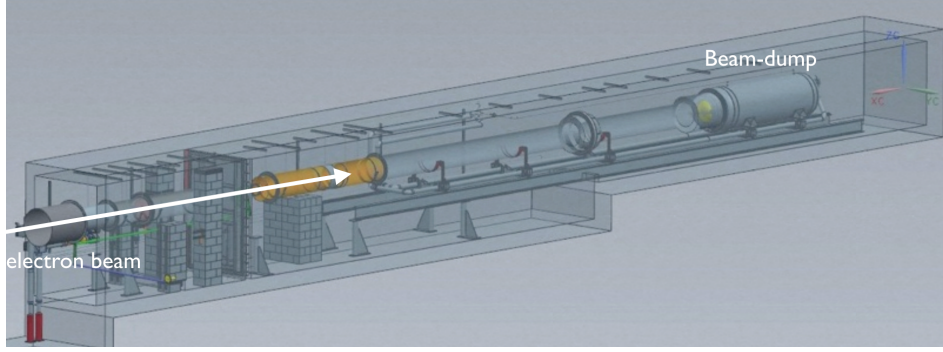


Figure 9: The Hall-A beam-dump enclosure in the concrete tunnel.

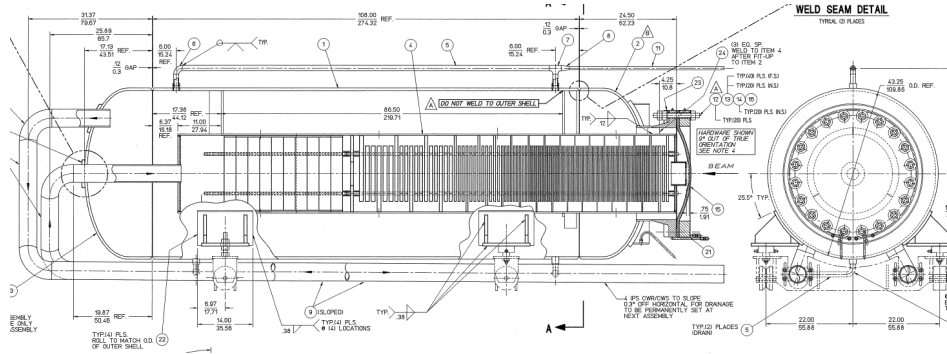


Figure 10: A detailed drawing of the Hall-A beam dump.

for a beam dump experiment at JLab.

The Hall-A beam-dump is enclosed in a concrete tunnel at the end of the beam transport line. A rendering of the dump and the last fraction of the beam line is shown in Fig. 9. The dump is made by a set of about 80 aluminum disks, each approximately 40 cm in diameter of increasing thickness (from 1 to 2 cm), for a total length of approximately 200 cm, followed by a solid Al cylinder 50cm in diameter and approximately 100 cm long. They are both cooled by circulating water. The full drawing of the beam-dump is shown in Fig. 10. To increase the radiation shielding, the thickness of the concrete tunnel surrounding the Al dump is about 4-5 m thick.

### 3.2 The BDX detector

The BDX detector is made by two main components: an electromagnetic calorimeter used to detect signals produced by the interacting dark matter, and a veto detector used to reduce the cosmic background. The veto detector consists of a passive layer of lead sandwiched between two instrumented layers of scintillators. The lead shielding



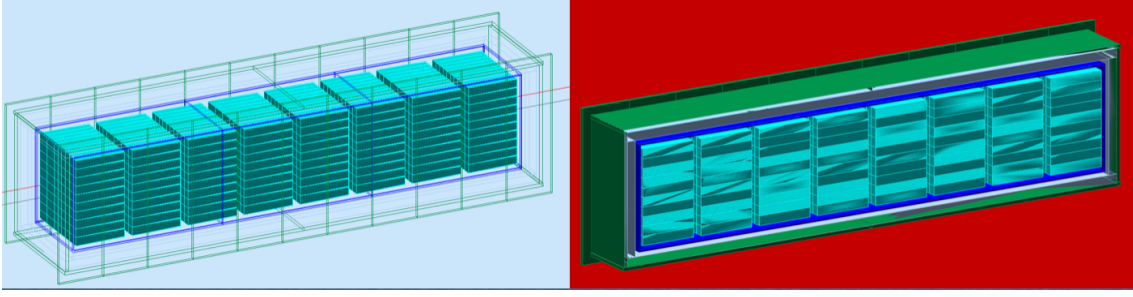


Figure 11: A GEANT4 implementation of the BDX detector. On the right, the Outer Veto is shown in green, the Inner Veto in blue, the lead in gray and the crystals in cyan.

reduces the sensitivity to low-energy environmental background (mainly low energy photons). A sketch of the BDX detector is shown in Fig. 11. The detector concept has been validated by a campaign of measurement at INFN - Sezione di Catania and Laboratori Nazionali del Sud (LNS) with a prototype, extensively discussed in Appendix B.

### 3.2.1 The electromagnetic calorimeter

The core of the BDX detector is an electromagnetic calorimeter sensitive to both the  $\chi$ -electron and  $\chi$ -nucleon scatterings. The signal expected in the two cases are quite different: a few GeV electromagnetic shower in the first and a low energy (few MeV) proton/ion recoil in the latter. Among the different options we chose a high-density, inorganic crystal scintillator material to reduce the detector footprint, fitting in the new proposed facility for beam-dump experiments at JLab (see Sec. 3.6). The combination of a low threshold (few MeV) sensitivity for high ionizing particles (light quenching not higher than few percents), a reasonable radiation length (few centimeters), together with a large light yield limits the choice to few options: BGO, BSO, CsI(Tl) and BaF<sub>2</sub><sup>‡</sup>. Considering that the request of about 1 cubic meter of active volume would drive costs of any possible options in the range of few million dollars, and that the timeline for producing and testing thousands of crystals would be of the order of several years, we decided to reuse crystals from an existing calorimeter. Former experiments that still have the desired amount of crystals available from decommissioned EM calorimeters include: BaBar at SLAC (CsI(Tl)), L3 at CERN (BGO) and CLEO at Cornell (CsI(Tl)). After consulting with the management of the different laboratories, we identified the BaBar option as the most suitable for a BDX detector. In particular, the BaBar EM end-cap calorimeter, made by 820 CsI(Tl)

<sup>‡</sup>We are not considering some new very expensive crystals such as LYSO or LaBr.

Parameter	Values
Radiation length	1.85 cm
Molière radius	3.8 cm
Density	4.53 g/cm <sup>3</sup>
Light yield	50,000 $\gamma$ /MeV
Light yield temp. coeff.	0.28%/°C
Peak emission $\lambda_{\max}$	565 nm
Refractive index ( $\lambda_{\max}$ )	1.80
Signal decay time	680 ns (64%)
	3.34 $\mu$ s (36%)



Figure 12: Picture of a BaBar CsI(Tl) and table of properties.

crystals for an equivalent volume of about 1 cubic meter, matches perfectly the BDX requirement. The excellent performance of the BaBar calorimeter [40], together with the willingness of the SLAC management for an intra-DOE-Laboratories loan, makes this option technically suitable and practical, with minimal paperwork involved<sup>§</sup>. Details about the crystals dismounting procedure are not reported in this proposal, but from preliminary contacts with the SLAC personnel in charge of BaBar decommissioning [41], we have been ensured to receive all the necessary support in term of tools (a manipulator to extract modules with crystals from the frame) and information for a safe and efficient procedure. Funds and labour to reassemble crystals in a suitable way will be provided by the BDX Collaboration.

Crystals, that comes in different shapes and tapering, due to the projective geometry of the BaBar calorimeter, will be inserted in new regular-parallelepiped aluminum alveolus in order to have regular elements easy to assemble in variable-size arrays. The average size of each crystal is (4.7 x 5.4 x 32.5) cm<sup>3</sup> while the alveolus size is (5 x 5.5 x 33) cm<sup>3</sup>. Details about individual crystal properties are available in Refs. [40, 42]. The table in Fig. 12 reports the main parameters of the BaBar CsI(Tl) crystals.

The reference setup used in this proposal foresees 8 modules of 10x10 crystals each (800 total), arranged with the long size along the beam direction. This arrangement has a cross section of 50x55 cm<sup>2</sup> for a total length of 295 cm. Tacking advantage of the partially forward-focused  $\chi$  beam, the parallelepiped shape of the detector is preferable to a cube-like arrangement to maximise the  $\chi$ -electron interaction length.

<sup>§</sup>An *Expression of Interest* for the BaBar end cap calorimeter crystals has already been signed between the BDX Collaboration and SLAC management. As a consequence, 22 CsI(Tl) crystals have been shipped from SLAC to INFN in order to assemble a 4x5 ecal prototype.

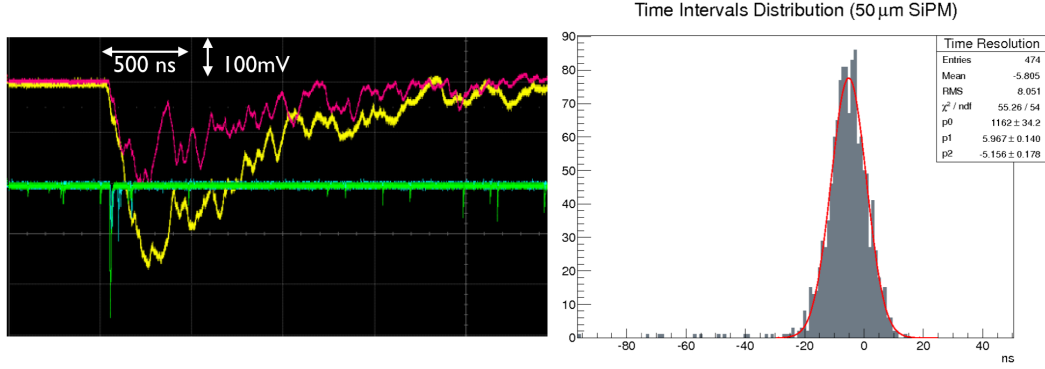


Figure 13: Left: A typical signal released by a crossing muon. Right: time distribution of cosmic muons; the spread is all due to the crystal performance since the trigger introduces negligible jitter.

A former BaBar EM cal crystals has been extensively tested in Genova to assess performances and to define the most suitable readout. In fact, the BaBar readout scheme used a pair of silicon diodes (Hamamatsu S2744-08) with unitary gain, that required a sophisticated ASIC-based amplification (complemented with a custom CAMAC-based readout electronics) to provide the integrated signal with no access to time information. The limited availability of the original FE electronic spares, as well as the absence of timing information, imposed a new readout scheme. We decided to bypass the pin diodes and place in the opposite crystal face a new readout sensor. Considering the slow scintillation time of the CsI(Tl) ( $\sim 2 - 3 \mu\text{s}$ ) we decided to use a fast readout sensor able to track the (faster) scintillation signal rise time (10-20 ns). Regular PMTs were excluded for the extra-length that would have been added to the crystal size. SiPMs represent a viable alternative providing an excellent timing and single photo-electron sensitivity. Considering the sizeable CsI(Tl) light yield a small area sensor (e.g.  $6 \times 6 \text{ mm}^3$ ) satisfies the BDX requirements providing a cheap and high-performing solution. SiPM will be coupled to custom trans-impedance amplifiers already used in the prototype tested in Catania (see Appendix B) Results of our tests performed coupling a BaBar crystal to  $3 \times 3 \text{ mm}^3$  SiPMs with different pixel size (25 and  $50 \mu\text{m}$ ) are reported in Fig. 13. They show that a light yield of  $\sim 10 \text{ phe/MeV}$  and a time resolution of about 6-7 ns (for cosmic muons) is achievable. The use of 4-times larger sensors ( $6 \times 6 \text{ mm}^3$ ), now commercially available, would make the SiPM option even more suitable for the BDX needs. The limited timing achievable with CsI(Tl) crystals does not represent a limitation for BDX since a tight time coincidence between the detector and the beam (bunches separated by 4 ns) would require a time resolution of tens of ps, difficult to achieve with any organic crystals for small

energy deposition.<sup>¶</sup>

All the results discussed in this proposal do not consider any change to the beam structure. However, from a preliminary discussion with JLab Accelerator Division [43], we concluded that it may be possible to operate the CEBAF accelerator in such a way that a reduction of a factor 5 in the beam-unrelated background would be feasible, even with the above timing resolution (see Sec.5.)

### 3.2.2 The active VETO system

The EM calorimeter is operated inside two hermetic layers of plastic scintillator veto (see Fig. 14). Between the Inner (IV) and Outer Veto's (OV) a layer of lead prevents low energy photons from hitting the crystal. The OV consists of 2cm-thick plastic scintillator, coupled to a single-side PMT with a plexiglass light guide. Due to the sizeable size requested to cover the whole calorimeter and to preserve the possibility of changing the geometry, the OV is segmented in many different paddles. In particular, the top and the bottom are divided in two parts while the lateral sides are made by 11 paddles per side. The upstream and downstream covers are made by the same plastic scintillator thickness but read by a PMT located at the center, directly glued on the surface. The paddle's geometry for the reference configuration has been inspired by size and arrangement of the prototype tested in Catania (see Appendix B).

The IV consists of a hermetic box comprised of 6 1-cm thick plastic scintillator paddles. To avoid the PMT encumbrance and keep the size of the OV as small as possible, the lateral paddles are read on one side by 4 SiPM. Grooves on the surface host two 1mm WLS fibers to convoy the scintillation light to the SiPM. This solution presents many advantages: the reduced attenuation length ( $\sim 6$  m) allow to limit the number of paddles not requiring further segmentation; the redundancy resulting by the light transmission inside the clear plastic makes any single SiPM inefficiency negligible (a hit on a paddle is acknowledged when at least one of the four SiPMs fires). The upstream and downstream covers have a spiral-like groove. The WLS fibers are read by one SiPM per paddle located on the scintillator surface. The compact design of the IV results in a fully hermetic plastic scintillator box. As for the OV, all these solutions were tested on the prototype currently running in Catania (see Appendix B).

---

<sup>¶</sup>Plastic scintillator would have been a good alternative in term of light yield, timing and costs but the reduced density would require a detector almost 5 time bigger in length making this choice impractical.

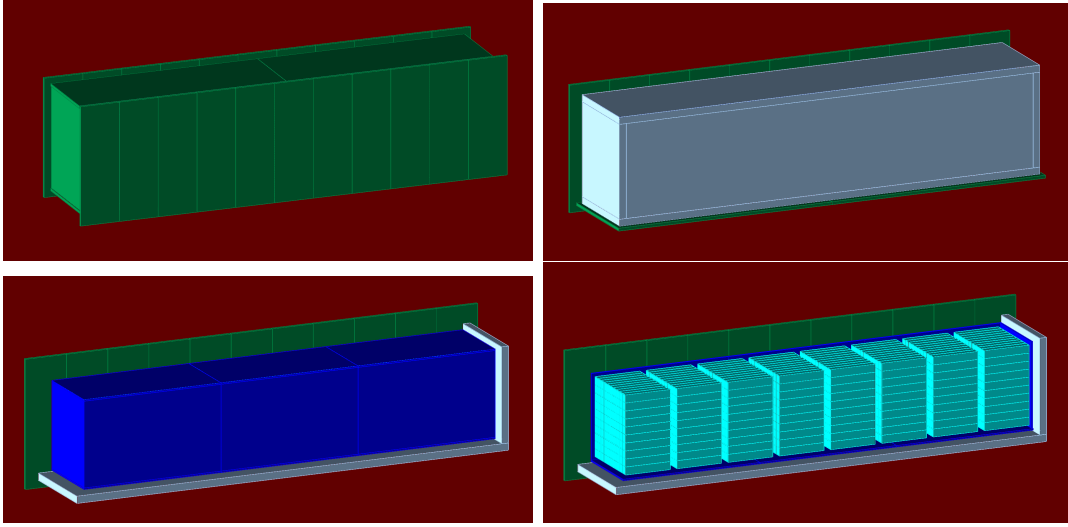


Figure 14: The BDX detector. The Outer Veto is shown in green: side paddles are read from the top by a PMT coupled to a light guide, the top and the bottom paddles are read by a PMT on the side coupled to a light guide and the upstream and downstream paddles are read by a PMT directly attached to the large face of the scintillator (PMT and guides are not shown in the drawing). The Inner Veto is shown in blue: side, top and bottom scintillators are read by 4 SiPM placed on the sides, coupled to WLS fibers glued to 4 parallel grooves; the upstream and downstream paddles have a spiral-like groove with two SiPM coupled to both sides (SiPM and grooves are not shown). The lead vault is shown in gray. Crystals arranged in 8 blocks of 10x10, are shown in light blue. Each crystal is read by a SiPM directly attached on the front face (not shown).

### 3.2.3 The lead vault

In between the two active vetos a 5cm thick layer of lead prevents low energy photons to reach the crystal. The “sandwich” configuration, with the lead between IV and OV, has been chosen to track the cosmic muons in the OV that may produce spallation in the dead material. It also acts as radiator for high energy photons produced by cosmic muon spallation, whose charge component is then detected by the IV. The lead vault has only a tiny clear window on the bottom side to let the calorimeter and IV cables to exit. Some lead bricks placed in front of the aperture mitigates the direct exposure to the external background. As discussed for the two veto’s, also the lead vault has been implemented in the prototype and tested in Catania.

### 3.3 Trigger and data acquisition

The trigger and data acquisition (TDAQ) system must be compatible with the specificity of the experiment, where the traditional concept of “event” is less applicable. Basically, the main trigger condition will be defined as any crystal signal exceeding a certain threshold. When this condition is met, the signal from crystals that crossed the threshold must be read, to determine hit energy and time, together with signals from all the active-veto counters. For the latter, the system must be designed to acquire also potential signals that occurred up to  $\mathcal{O}(10)$   $\mu\text{s}$  before the crystal hit time. In this way, it is possible to reconstruct a complete “story” of the event, thus allowing identification and rejection of all the possible background topologies - including rare effects such as muon decays, delayed neutron hits, etc.

Given these requirements, we foresee a TDAQ system based on Flash to Analog Digital Converters (FADCs). These devices continuously sample the input signal at a rate  $R$ , working as a multi-channel digital oscilloscope. In the basic operation mode, when a trigger is delivered to a FADC board, all the samples within a programmable acquisition window - properly shifted with respect to the trigger time - are reported. The use of a multi-buffer architecture allows the system to work with almost zero dead-time. Most FADC boards can also run online signal-processing algorithms on an on-board FPGA, thus making these devices very versatile.

The TDAQ system design here discussed is based on the 16-channels, 250-MHz sampling rate VME FADC board developed by the JLab Fast Electronics group [44]. The main characteristics are reported in Table 1. Each FADC in a crate can communicate with a central crate trigger board through a fast (2.5Gb/s) serial line (VXS), both for trigger formation and for events readout. FADC and related “ancillary” trigger boards have been already extensively used to setup the TDAQ system for various experiments at Jefferson Laboratory: GlueX, CLAS12, HPS, . . . . The latter, in particular, exploits the FADC online-processing capabilities in a sophisticated, FPGA based, trigger system.

The following parameters, obtained from the BDX prototype measurements in Catania, were considered while designing the system:

- 1000 CsI(Tl) crystals, each read by a SiPM. Signal rate: 5 Hz / crystal
- 100 active veto channels, each read by a SiPM. Signal rate: 30 Hz / counter

The simplest TDAQ system for the BDX experiment, as discussed before, implements as main trigger condition the OR from the discriminated crystal signals above a certain threshold. This algorithm is already implemented in the standard FADC and trigger boards firmware. In order to maximize the information for each event, the largest readout window (8  $\mu\text{s}$ ) is employed for both crystal and active veto signals. The following readout modes are foreseen:

Parameter	Value
Sampling rate	250 MHz
Voltage range	Selectable: 500 mV, 1 V, 2 V
Dynamics	12 bits
Acquisition buffer	8 $\mu$ s
Readout window	2 $\mu$ s (up to 8 $\mu$ s with custom firmware[45])

Table 1: JLab FADC250 board main parameters

- For the crystals, signals are read in so-called “raw-mode”: for every trigger, all the 2048 samples in the 8  $\mu$ s acquisition window are reported, with no online elaboration. This gives maximum flexibility for the off-line analysis.
- For the active veto channels, signals are processed by an online pulse-integration algorithm implemented on the FPGA<sup>\*\*</sup>. The algorithm reports, for each pulse exceeding a programmed threshold, the pulse area, amplitude, and threshold-crossing time. Up to four distinct pulses per channel per event can be reported.

The event and data rate are estimated with the very conservative assumption of having completely uncorrelated signals, i.e. adding the individual rates from all the crystals.

- The overall trigger rate will be  $R_{trg} = 5 \text{ Hz/crystal} \cdot 1000 \text{ crystals} = 5 \text{ kHz}$ .
- The data size of each crystal signal is:  $D_{crs} = 2048 \text{ samples} \cdot 12 \text{ bit/sample} = 3 \text{ kB}$ . The total data rate from crystals is:  $DR_{crs} = D_{crs} \cdot R_{trg} = 14 \text{ MB/s}$ .
- The data size of a FADC-integrated pulse is  $D_{veto} \simeq 12\text{B}$ . Assuming (conservatively) that  $N_{veto}/10$  veto counters report a pulse for each trigger, the total data rate from these is:  $DR_{veto} = N_{veto} \cdot D_{veto} \cdot R_{trg} = 1 \text{ MB/s}$ .
- The total event rate is:  $DR_{tot} \simeq 1.1 \cdot (DR_{crs} + DR_{veto}) = 16 \text{ MB/s}$ . A 10% overhead has been assumed for event-related information (event time, indexes of channels, ...)

---

<sup>\*\*</sup>This algorithm already exists in the FADC250 firmware, and has been extensively tested for short ( $\mathcal{O}(100 \text{ ns})$ -wide) pulses.



These values are completely compatible with the existing hardware, firmware and software, thus allowing the implementation of the TDAQ system with no major efforts. The list of the required equipment is reported in Appendix D.

The proposed solution has the advantage of being robust and achievable with already-existing technologies. However, given the flexibility provided by FADCs and trigger boards - in particularly the newly developed VXS Trigger Processor (VTP) -, we also plan to investigate an alternative, trigger-less readout mode. The rough scheme of this evolved setup is the following: every time a crystal or a plastic scintillator counter signal exceeds a local threshold, a corresponding raw-waveform (within a proper acquisition window), is reported, via VXS bus, to the central VTP board, together with a fine time-stamp. The VTP sees, therefore, a “continuous stream” of raw-waveforms from all the channels in the VME crate, and will report it via a fast optical link (34 Gb/s) to one (or more) VTP boards in a master trigger crate, collecting data from all the detector channels. On this board, the continuous datastream is analyzed by different online algorithms, to identify and save “events” of interest. Preliminary estimates of the foreseen data rate show that this solution is, in principle, possible for the BDX detector. We plan to investigate it further, working in collaboration with the JLab fast electronic group.

### 3.4 Computing resources

The computing resources needed by the experiment were estimated as follows. Assuming a rate of 5 kHz, as outlined in the previous section, the total number of recorded triggers that we expect to accumulate in four years of data taking is of the order of  $5 \cdot 10^{11}$ . Based on the reconstruction software performance achieved on the Catania prototype data and on Monte Carlo data, we estimated the time needed to reconstruct one event on a modern CPU to be of the order of 10 ms. The total number of CPU-hours needed to reconstruct the entire BDX data set is therefore of the order of  $2 \cdot 10^6$  including 50% contingency. Additional  $6 \cdot 10^6$  CPU hours will be needed for the Monte Carlo simulation of about  $10^{11}$  EOT (single event simulation time of 200 ms). Based on the estimated data size and rate, the overall volume of collected data for four years of running amounts to approximately 2 PB. We assume the data recorded in the first year, i.e. 20% or 400 TB, would be permanently saved to tape. For the remaining 80%, online software, that will be developed and optimized based on the first year of data, will be used to filter the portion of the data where potentially interesting events are found, with a data reduction factor of one order of magnitude. The total permanent storage needed for real data will be of 600 TB, including 80 TB of reconstructed data and 20 TB of Monte Carlo data. In addition, approximately 100 TB of disk space would be needed to temporarily store raw and reconstructed data, and Monte Carlo events.



### 3.5 The event reconstruction framework

The main requirement of the BDX event reconstruction and framework is the possibility of developing a modular code, where different pieces, each related to a simple task, can be assembled together. This modular design allows to de-couple the problem of defining the global reconstruction scheme from the actual implementation of the single tasks, and, at the same time, permits to change the first without the necessity of rewriting the latter. Finally, a modular architecture is also well suited for a collaborative development effort.

The framework should also be designed to fully exploit modern computer-science technologies that can significantly speed-up the reconstruction procedure (multi-threading, multi-processing, etc.). Finally, the compatibility with other common software tools, such as ROOT, is highly desirable.

After consulting with experts in software development, we identified the “JLab Data Analysis Framework” (JANA) as a convenient software package to develop the reconstruction code [46]. JANA is a software package written in C++ that provides the mechanism by which various pieces of the reconstruction software are brought together to fully reconstruct the data. This is motivated in large part by the number of independent detector subsystems that must be processed in order to reconstruct an event. The choice of the Hall-D GlueX experiment to use this as the basis for the development of the corresponding reconstruction software clearly demonstrates the “maturity” of this code. Furthermore, the choice of using an already existing code - with proper modifications to tailor it for BDX - has the clear advantage of availability of experts support and possibility to re-use already developed parts. A preliminary version of the reconstruction software, to handle data from the BDX prototype measurements (see Appendix B), has been already implemented.

The JANA framework is built upon the idea of data factories. The general idea is the following: when data is requested from a factory (i.e. an order is placed) the factory's stock is first checked to see if the requested items already exist. In JANA, a factory only makes one type of object, so if the objects have already been made for this event, const pointers to them are passed back. Otherwise, it must manufacture (instantiate) the objects. The manufacturing procedure itself needs first to get the “parts” from which to build its own objects. These parts are objects produced by other factories. Eventually, one gets down to requesting objects that are not produced by a factory but rather, originate from the data source (event file or online TDAQ system). In this scheme, therefore, the overall reconstruction scheme is defined by the specific chain of factories involved in the process, starting from the highest-level, i.e. the event builder, down to the lowest-level ones, i.e. those associated with each sub-detector. Multiple reconstruction schemes, possible sharing the same factories, can be implemented in parallel, each scheme being associated, for example, to analysis

tasks.

## 3.6 A new facility for beam-dump experiments at JLab

### 3.6.1 Building and access to detector

We present the reference layout of the infrastructure and civil construction needed for the BDX experiment behind Hall A. This concept, referred to as “C1”, grew out of feedback and comments to early ideas for the civil design [47, 48] and the BDX Letter-of-Intent [49]. This reference C1 is used to determine overall dimensions and shielding in order to estimate costs and locate the detector relative to the Hall A beamdump. While dimensions are consistent with the proposed experiment, specific details for the detector should be obtained from other sections. We expect that this concept will evolve as the results of simulation are feed back into the concept for civil construction.

The present concept provides full personnel access to the detector at the basement level of the BDX building. The location of the detector is sufficiently deep, that it is unlikely that there would be any significant savings by installing the detector into a shaft without personnel access. There is only about 5 m of concrete shielding surrounding the Hall A dump (see Fig. 15) and therefore it is likely that additional shielding will be required if the detector is placed close to the beam dump source. Thus there may be considerable excavation required even if a very narrow shaft is used for the detector. This would also be true if the shaft is constructed at an angle (see Fig. 4 of Ref. [47]) since it is probably easier to dig a large ditch and backfill than to dig a tunnel at an incline. The difficulties and complications that come from limited access and restoring cosmic-ray shielding every time the detector is serviced can be avoided by starting with a concept that has a shaft for moving the detector underground and a personnel access to service the detector once installed. A sketch of the plan view is given in Fig. 16 and a sketch of the elevation view is given in Fig. 17.

This concept includes an above-ground building with a crane to lower the detector underground and stair access to the underground room with the detector during operation (see Fig. 16). The detector would be lowered down through an access shaft and then rolled into a room, which is shielded from cosmic rays by the overburden. This room is accessible using the stair connection to the underground (see Fig. 17). Electronic racks would likely reside underground with only fiber connections to the outside world. The environment for the entire building would be controlled for proper operation of the detector and electronics.

Component	Size	Number
CsI(Tl) crystals	$5 \times 5 \times 30 \text{ cm}^3$	100/module
Module	$15 \times 15 \times 30 \text{ cm}^3$	10
Calorimeter	$50 \times 50 \times 300 \text{ cm}^3$	1
Active veto	$100 \times 100 \times 350 \text{ cm}^3$	1

Table 2: List of components of the reference detector and their dimensions. Note that the detector design has evolved considerably and this table should be taken only as a rough basis for infrastructure sizing.

### 3.6.2 Detector size

The following detector design has been considered as the basis for infrastructure sizing and cost estimates. We underline that this is just a conservative approximation of the final detector design reported in the proposal, only used for the aforementioned purpose. We assumed that the detector will fit into a volume of  $100 \times 100 \times 350 \text{ cm}^3$ . The detector was sized based on early concepts based on the promising and compact option to re-use the Thallium-doped CsI crystals from the BaBar end cap calorimeter at SLAC [40], with improved SiPM-based readout. The weight of the calorimeter is about 3.4 metric tons. The reference dimensions are shown in Table 2.

For the active cosmic-ray shield we used reference dimensions from the Los Alamos beam dump experiment E645 [50]. It consists of an outer layer of active scintillator and an inner passive layer of lead. The E645 experiment used about 15 cm for both the lead and scintillator layers. We took the thicknesses of each layer to be 5 cm, based on simulations for the proposal. The total weight of the lead shield is 5.5 metric tons.

The number of electronics channels for this detector is of order one thousand for the calorimeter and one hundred for the active veto (see Table 2). The power consumption per calorimeter channel (SiPM preamp) is about 0.1 W. For the veto system, with the conservative assumption of using PMTs for both the inner and the outer veto, the power consumption is about 2 W/channel. This result in a total power consumption of about 300 W for the whole detector. The digitizing electronics power consumption (with about 70 16-channels digitizing boards) is about 4 kW<sup>††</sup>. These are only rough guesses, but more precise estimates must wait for a full electronics design.

---

<sup>††</sup>The power dissipated with an “empty” crate containing a CPU is about 80 W, and the nominal power consumption for the 16-channel JLab Flash 250 MHz is 58 W/board.

### 3.6.3 Shielding from the beam dump and overburden

Various considerations for the shielding from the beam dump and overburden to shield from cosmic rays are discussed in Ref. [47]. The detector is located sufficiently far from the beam dump and there is sufficient shielding in the form of concrete (150 cm) and iron (660 cm) to reduce any conventional particle source to acceptable levels. The amount of overburden is assumed to be a minimum of 10 meters of water equivalent (mwe). At the depth of the beam (762 cm), 10 mwe of overburden is achieved by covering the underground room up to grade level.

### 3.6.4 Cost estimate

A preliminary cost estimate was conducted based on dimensions described above. The estimate is based on the cost of existing buildings, estimates for the MEIC project and RSMEANS Facilities Construction Cost Data 2015. The cost estimate was made by T. Whitlatch. C. Whitlatch and R. Yasky from Facilities Management kindly provided access to cost information and helpful discussions on facility requirements. The estimate includes the following features

- excavation, dewatering, backfill and compaction of soil
- walls below grade, underground room at beam level
- personnel access and stairs
- above-ground building with 15 t crane
- HVAC, plumbing, piping, LCW, electrical distribution and lighting
- Encasing and burying iron shielding blocks (assumes block availability)
- Road, parking lot and power substations

The total estimated cost is \$1.3M. A breakdown of the cost estimate can be found in Figs. 18 and 19.

## Hall A Beam Dump / C1

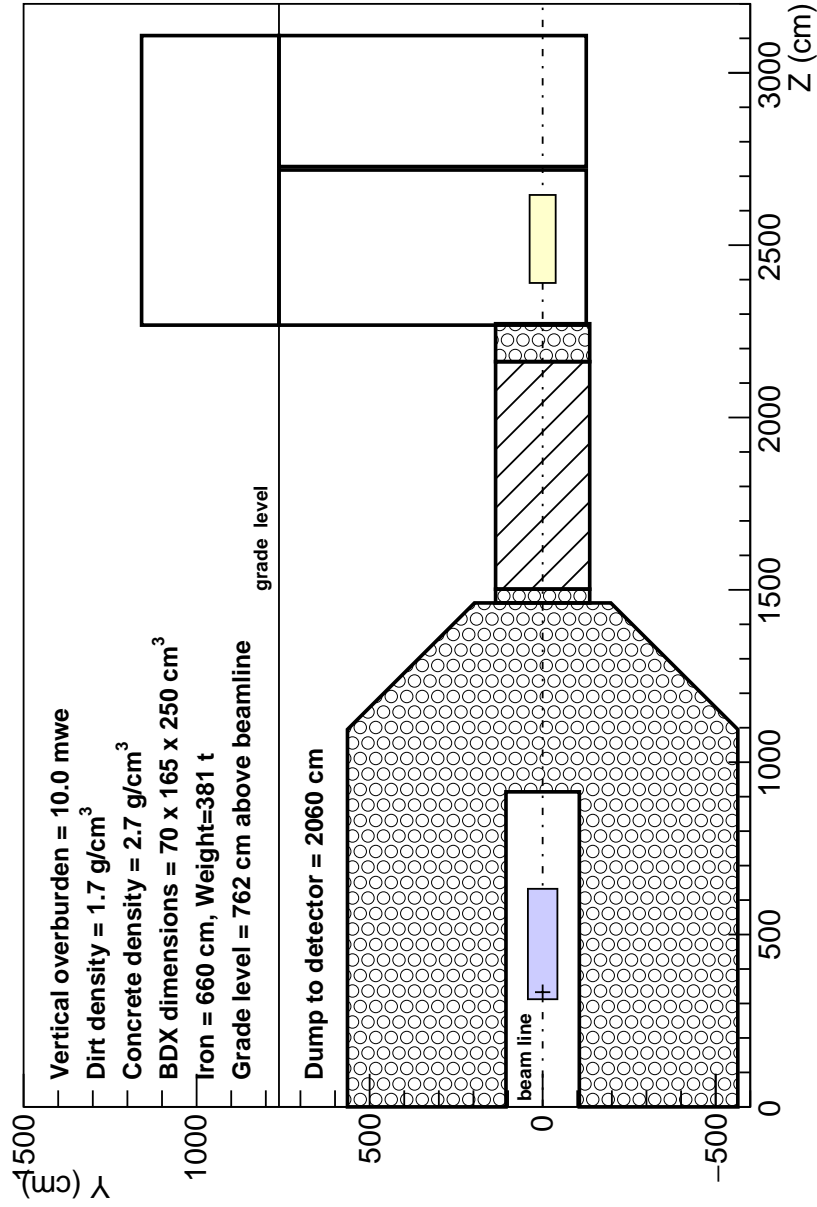


Figure 15: Elevation sketch of civil concept C1. This view includes the Hall A beam dump proper and surrounding concrete, filling material between the beam dump and the BDX experiment, the detector in the underground room and staircase area. General parameters and assumptions are specified on the drawing.

## C1 plan for BDx

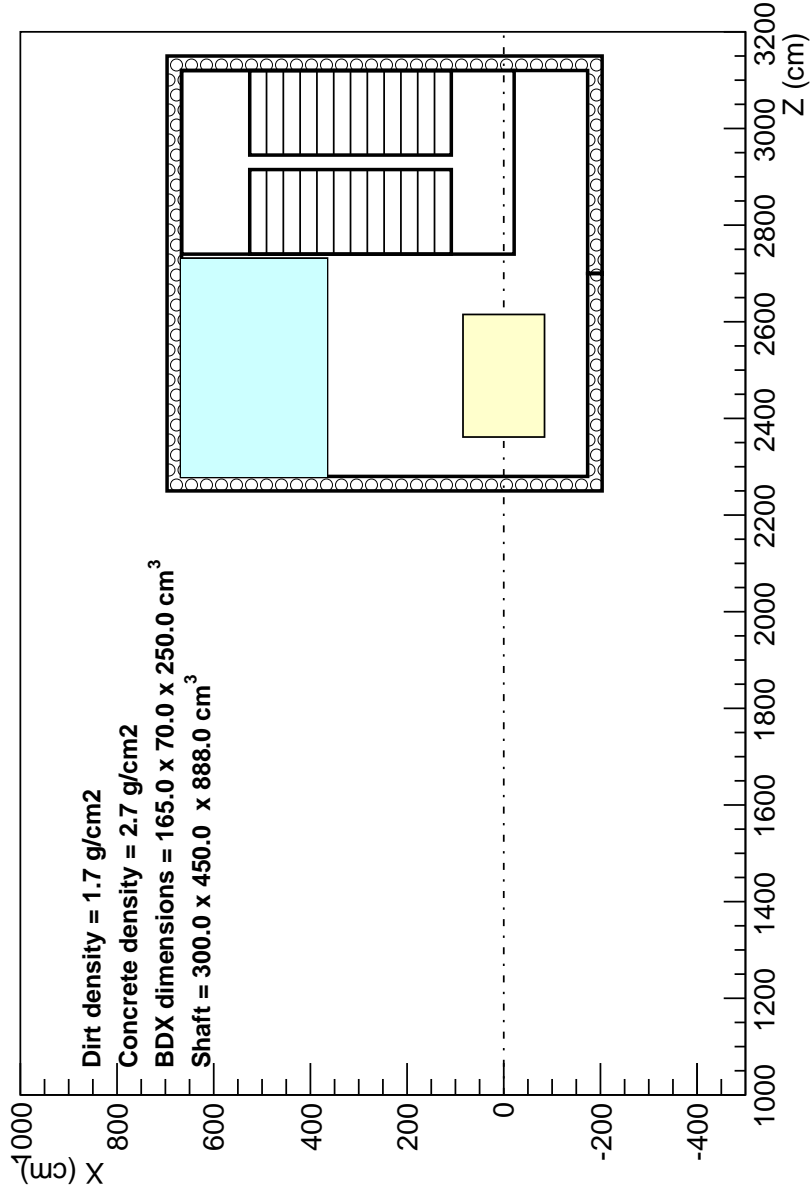


Figure 16: Plan sketch of civil concept C1. The vertical shaft for access to the underground room is shown in light blue. The detector outline, including cosmic-ray shield is shown in light yellow. Access stairs are included for access to the underground room. General parameters and assumptions are specified on the drawing.

## C1 elevation for BDX

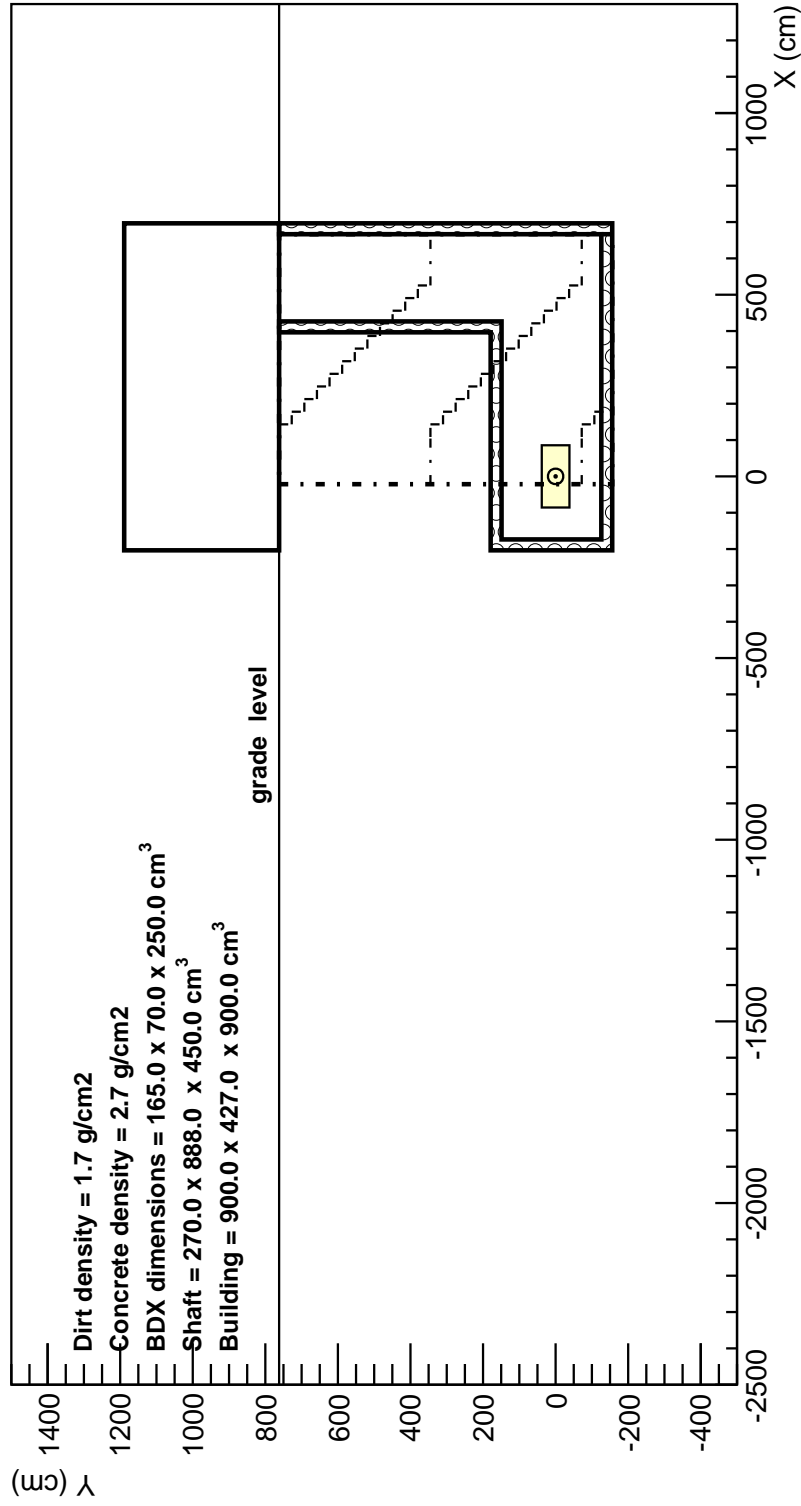


Figure 17: Cross sectional sketch perpendicular to the beam of civil concept C1. The vertical shaft is shown to the north of the detector room. After lowering the detector to the underground room, the detector would be rolled inside into the underground room that is shielded against cosmic-rays. The access stairs are shown schematically with dashed lines, which allow access to the underground room. General parameters and assumptions are specified on the drawing.

WBS Description Height, Feet Width, Feet Length, Feet Total kVA No. of Bldgs LCW Cooling Plant Size (kVA) 5/19/2016 Added Pavement, SEG block install, utilities to feed the building

1 BDX Access building Houses power supplies & mechanical equipment Personnel & equipment access to the tunnel at Elev 11 feet; Const depth 30' Similar to North Access Building #67

Jefferson Lab - Facilities Management										
Item No.	Description	Height, Feet	Width, Feet	Length, Feet	Quantity	Units	Unit Cost	Direct Cost (\$)	Dawtr WD	Comments
1	Excavation	30	86.0	125.0	11,944	CY	5.42	64,703		No shoring or dewatering. Assume 30' deep, 1:1 Slope, with SEG shielding
2	Dewatering				35	Day	1,650.00	58,541		Prorate for calendar days, no VOC treatment
3	Backfill w/ compaction				11,713	CY	4.22	49,477		10 Excavation minus disposed
4	Dispose of Excess Soil	30.0	13.0	16.0	231	CY	4.66	1,078		Volume of underground structure
5	6" Perforated Pipe Foundation Drain			29.0	58	LF	8.80	510		Concurrent w/ other work
6	3" Mud Slab Concrete	0.25	26.5	29.5	7	CY	191.68	1,387		3' beyond floor slab
7	Floor Slab - at tunnel level	1.5	26.0	29.0	42	CY	294.00	12,315		Assume SF is 50% grade level floor SF.
8	Walls below grade - equip access	30.0	1.5	84.0	140	CY	543.81	76,133		1 Plus alcove
9	Walls below grade - people access	30.0	1.5	76.0	127	CY	543.81	68,883		1 ~15' x 24' area, 18" thick
10	Detector Alcove concrete	4.0	15.0	14.0	31	CY	543.81	16,919		1 ~10' x 20' area, 18" thick
11	SEG block encasement	10.0	1.5	120.0	67	CY	543.81	36,254		1 ~10' x 25' area, 18" thick walls, bottom and top
12	Stairs, Clp, w/ landing, with nosings				4	Flight	4,125.00	16,500		Walls at roof & floor
13	Waterstop			160.0	320	LF	5.91	1,892		1 Walls
14	Waterproofing Membrane	30.0		76.0	2,280	SF	2.43	5,540		0 Under slab
15	Bentonite Waterproofing	1.5	26.0	29.0	919	SF	2.40	2,205		1 With Membrane
16	Protection Board	30.0		76.0	2,280	SF	2.06	4,686		0 With Bentonite
17	Drain Board	1.5	26.0	29.0	919	SF	1.30	1,190		6' slab
18	Floor Slab, grade level at access	0.5	26.0	29.0	11	CY	650.00	7,270		1' fill
19	Gravel Fill w/ Compaction	1.0			3	CY	42.26	122		6' slab no 2nd floor
20	Floor Slab on Grade, Thicken Edge				78	SF	8.90	695		
21	Floor Slab - at second floor		0.0	0.0	-	SF	7.03	-		
22	Concrete Floor Sealer				1,586	SF	0.54	856		
23	Structural Steel Framed Bldg		26.0	32.0	832	SF	14.88	12,380		
24	Metal Insulated Wall Panels	14.0		116.0	1,624	SF	22.70	36,865		includes bathroom
25	Masonry Interior Walls	10.0		168.0	1,680	SF	14.65	24,609		
26	Install SEG shielding				36	ea	500.00	18,000		
27	Metal Deck Roof		26.0	32.0	832	SF	1.85	1,538		
28	Insulated Roofing System		26.0	32.0	832	SF	9.86	8,204		
29	Flashing		26.0	32.0	116	LF	27.15	3,149		
30	Interior Metal Stud & GWB walls				-	SF	5.89	-		All interior walls are CMU
31	Personnel Doors				3	EA	1,762.25	5,287		
32	Overhead Service Doors				1	EA	5,425.00	5,425		
33	Railings, Steel, 3 rail				102	LF	51.50	5,253		
34	Wall Rail				60	LF	27.00	1,620		
35	Grating		26.0	32.0	83	SF	15.04	1,251		Assume 10% of floor area

Page 1

Figure 18: Cost estimate for civil concept C1. Page 1.



Page 2

Figure 19: Cost estimate for civil concept C1. Page 2.

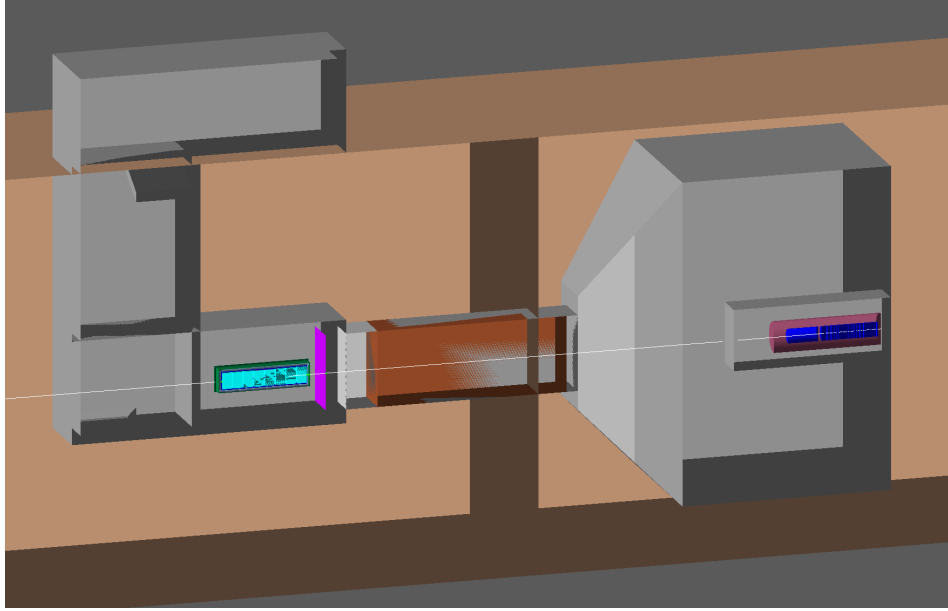


Figure 20: Implementation of the BDX detector and Hall-A dump in GEMC. The white line shows the beam centerline.

## 4 Signal and background rates

### 4.1 Simulations of the experimental set-up

The proposed detector, the new underground facility and the Hall-A beam-dump geometry have been implemented in GEANT4 within GEMC simulation package [51]. In the following sections we present results concerning the expected rates from interaction of a  $\chi$  particle, beam-related background and cosmogenic background. Figure 20 shows the geometry as implemented in simulations.

### 4.2 Signal

The expected number of signal events measured in the detector was estimated through a Monte Carlo calculation, according to the model for LDM production and detection described in Sec. 2.3. The calculation involves three steps. First, the evaluation of the number of  $\chi$  particles electro-produced in the beam dump, through on-shell or off-shell  $A'$  mediator. Then, the calculation of the interaction rate in the detector. Finally, the estimation of the actual detection efficiency for the scattered electrons and protons. All these numbers -  $\chi$  production yield,  $\chi$  scattering rate, detector efficiency - depends on four parameters: the mass of the  $\chi$  ( $m_\chi$ ), the mass of the exchanged  $A'$

( $m_{A'}$ ), the coupling constant between the electron and the  $A'$  ( $\varepsilon$ ) and the coupling constant between the  $\chi$  and the  $A'$  ( $\alpha_D$ ). However, the kinematics only depends on the two masses;  $\varepsilon$  and  $\alpha_D$  are only related to the absolute event yield. Therefore, calculations were performed with fixed values of these parameters, and final results were rescaled accordingly.

#### 4.2.1 $\chi$ production

The  $\chi$  production process in the beam-dump was simulated using a modified MadGraph4 version [52]. The software was used to generate LDM events produced in electron-aluminum nucleus collisions,  $e^-N \rightarrow e^-NA' \rightarrow e^-N\chi\bar{\chi}$  (where  $N$  is a nucleus with  $Z = 13$ ,  $A = 27$ ), and to calculate the total LDM production cross section. MadGraph was modified to include the aluminum nucleus form factor as found in [53], which accounts for coherent scattering, as well as for nuclear and atomic screening.

The most common solution to account for the finite dump thickness adopted in similar calculations is to use the “single-radiation length approximation” ([13, 22], i.e. to consider an effective length equal to one radiation length, neglecting showering and energy loss effects. This strategy was, for example, adopted in the original E-137 re-analysis [38]. Instead, we performed a detailed study of the primary electron beam interactions in the beam dump, finding non-negligible corrections to the aforementioned approximation.

We proceeded as follows. First, we used the GEANT4 beam-dump simulation to sample the flux of electrons and positrons in the dump, as a function of energy, at different depths (measured in radiation length units,  $t$ ). To simplify the calculation, we adopted a simplified model of the beam-dump design, considering a uniform Aluminum cylinder. However, since all the results are reported in radiation length units, and the showering process dependence on the material is almost all contained in this quantity, we do not expect sizeable effects due to this choice. The result of the calculation was the differential energy spectrum of electrons and positrons as a function of the depth in the dump, normalized to the number of primary particles,  $\frac{dN}{dE}(t)^{\ddagger\ddagger}$ .

From this quantity, the total number of  $\chi - \bar{\chi}$  pairs produced per incident electron can be calculated as:

$$N_{\chi-\bar{\chi}} = \frac{N_{Av}}{A} \rho \cdot X_0 \int_0^{T_{dump}} dt \int_{E_{min}}^{E_0} dE \sigma(E) \frac{dN}{dE}(t) \quad (10)$$

where  $\rho \cdot X_0$  is the product of the  $Al$  density and radiation length (24.01 g/cm<sup>2</sup>),  $T_{dump}$  is the dump length in  $X_0$  units,  $\sigma(E)$  is the total cross section for the  $e^-N \rightarrow$

---

<sup>$\ddagger\ddagger$</sup> Positrons were included in the calculation since they can produce  $\chi - \bar{\chi}$  pairs in the dump just like electrons.

$e^- NA' \rightarrow e^- N\chi\bar{\chi}$  process,  $E_0$  is the primary electron energy, and  $E_{min}$  is the threshold energy. Given the  $t$ -dependence of  $\frac{dN}{dE}(t)$ , it is safe to perform the calculation with  $T_{dump} \rightarrow +\infty$ . This expression can be simplified by introducing the quantity  $\langle \frac{dN}{dE} \rangle \equiv \int_0^{T_{dump}} dt \frac{dN}{dE}(t)$ , that does not depend on  $\sigma(E)$ . The “single-radiation length approximation” is equivalent to  $\langle \frac{dN}{dE} \rangle = 1 \cdot \delta(E - E_0)$ . In terms of this average flux the  $\chi$  yield is:

$$N_{\chi-\bar{\chi}} = \frac{N_{Av}}{A} \rho \cdot X_0 \int_{E_{min}}^{E_0} dE \sigma(E) \langle \frac{dN}{dE} \rangle \quad (11)$$

For each  $m_{A'} - m_\chi$  combination, we estimated the total  $\chi$  yield and the corresponding energy spectrum by numerically integrating the above expression. We performed multiple MadGraph4 simulations at discrete energies  $E_i$ , weighting each result by  $\langle \frac{dN}{dE} \rangle_{E_i}$ , and then summing the different energy bins. The comparison of the  $\chi$  energy spectra obtained with this procedure and with the “single-radiation length approximation” is shown in Fig. 21 for two choices of  $m_\chi$  and  $m_{A'}$ . The effect of including the showering mechanism in the calculation is clearly visible: the  $\chi$  energy spectrum becomes more pronounced at lower energies and the absolute number of  $\chi$  particles increases, due to emission from secondaries. The net effect of this in the foreseen event rate is discussed in the next session.

#### 4.2.2 $\chi$ interaction

The  $\chi$  interaction in the detector was evaluated through a custom code, handling both the  $\chi - e^-$  and the  $\chi - p$  scattering processes. The program, given the incident  $\chi$  flux for a given set of model parameters, computes the expected event rate within the detector for both topologies. It also provides a set of Monte Carlo events, containing scattered electrons and protons in the detector volume, generated according to the foreseen kinematics. These are then passed to the full detector simulation, implemented with GEANT4, in order to evaluate the experimental detection efficiency.

The corresponding cross-sections were implemented in the code, according to the formulas described in [13]. For the  $\chi - p$  quasi-elastic process, we parametrized the nuclear effects by introducing an “effective” nuclear form-factor and an average 8 MeV binding energy (computed from the corresponding values for Cs and I nuclei). The energy spectrum of recoiling electrons and protons, computed for  $m_\chi = 10$  MeV,  $m_{A'} = 30$ , is shown in Fig. 22, comparing the “single-radiation length approximation” with the full beam-dump simulation. For the  $\chi - e^-$  scattering process, the energy distribution is much more pronounced at lower values when the beam showering is considered. The total number of expected events is 30% higher when the contribution of secondary electrons and positrons in the beam-dump is considered, with respect to the simple “single-radiation length approximation”. However, the fraction of events

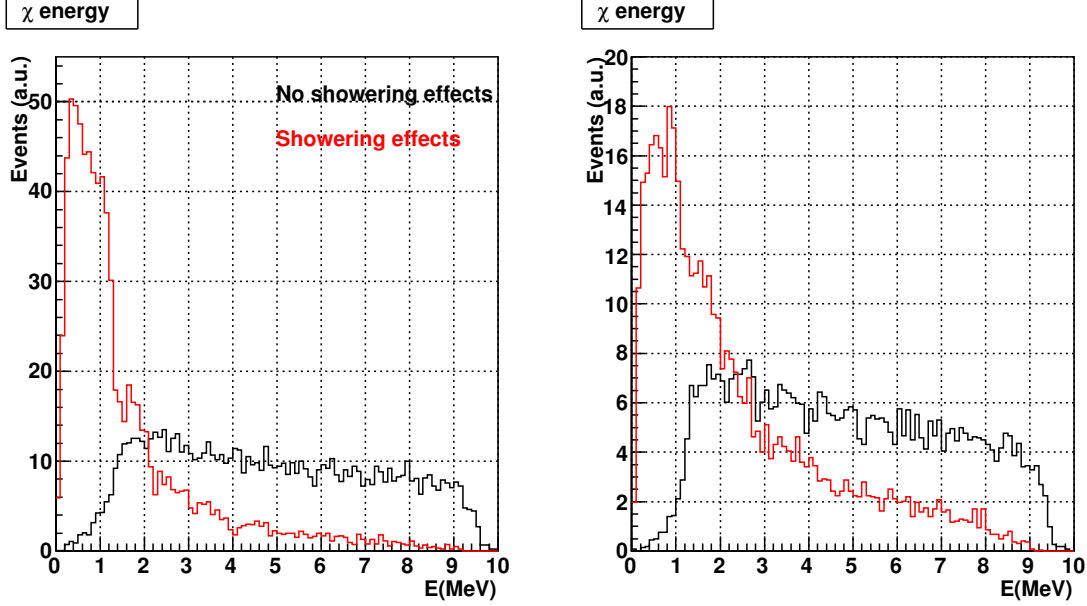


Figure 21: Energy spectrum of  $\chi$  particles produced in the beam dump, comparing the “single-radiation length approximation” (black) with the full beam-dump simulation (red). Left panel:  $m_\chi = 10$  MeV,  $m_{A'} = 30$  MeV. Right panel:  $m_\chi = 100$  MeV,  $m_{A'} = 300$  MeV. Vertical-axis units in the two panels are different.

with scattered electron energy greater than 300 MeV (500 MeV) is 40% (70%) less, resulting in a total event yield 10% (20%) lower (with the difference increasing if an even higher energy threshold is used). For the  $\chi - p$  process the difference between the two cases is less pronounced.

#### 4.2.3 Detector response

The BDX detector response to scattered electrons and protons has been studied with the aforementioned GEANT4-based simulation code. For each combination  $m_\chi - m_{A'}$ , the detection efficiency has been evaluated, for different selection cuts. For the  $\chi - e^-$  channel we considered the electrons scattered inside the detector volume with energy greater than 300 MeV. For this class of events, we evaluated the detection efficiency as a function of the energy deposited in a single crystal, which is the seed of the electromagnetic shower produced by the scattered electron inside the BDX calorimeter. Fig. 23 (top panel) shows the integrated efficiency extracted for  $m_\chi = 30$  MeV and  $m_{A'} = 90$  MeV. The blue curve represents the efficiency when we require the presence of a seed with an energy deposited greater than 300 MeV. The other curves indi-

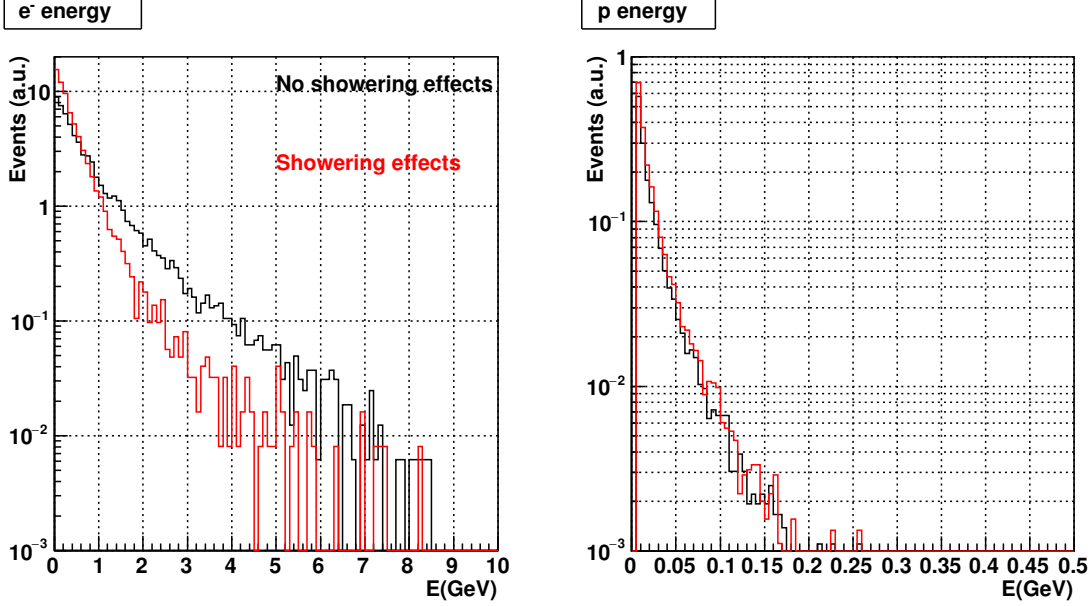


Figure 22: Energy spectrum of scattered electrons (left) and protons (right) in the detector, comparing the “single-radiation length approximation” (black) with the full beam-dump simulation (red). Both plots correspond to  $m_\chi = 10$  MeV,  $m_{A'} = 30$  MeV. Vertical-axis units in the two panels are different.

cate the efficiency when we also require the veto anticoincidences. In particular, the detection efficiency for  $E_{seed} > 300$  MeV with the Inner Veto ( $\epsilon_{(E_{seed} > 300 \text{ MeV})}^{IV}$ ) or the Outer Veto ( $\epsilon_{(E_{seed} > 300 \text{ MeV})}^{OV}$ ) in anti-coincidence is about 14% and 31%, respectively. In the  $m_\chi - m_{A'}$  parameter space covered by BDX, the two efficiencies vary in the following range:  $\epsilon_{(E_{seed} > 300 \text{ MeV})}^{IV} \sim 10 \div 20$  % and  $\epsilon_{(E_{seed} > 300 \text{ MeV})}^{OV} \sim 20 \div 35$  %. It is worth noticing that the  $\chi - e^-$  scattering generates events in the calorimeter with a clear topology. For example, Fig. 24 shows two distinct features expected for these events. Due to the natural collimation of the  $\chi$  beam, most of the crystals involved in the e.m. showers are the central ones (left panel). Moreover, the e.m. showers are expected to be produced mostly along the beam direction. The right panel of Fig. 24 shows the angle between the beam axis and the direction of the e.m. shower, here defined as the direction formed by the energy weighted positions ( $x_{cl}, y_{cl}$ ) of two clusters detected in two different modules of the calorimeter.

For the  $\chi - p^-$  scattering events, the bottom panel of Fig. 23 shows the integrated detection efficiency as a function of the proton energy, for the same  $m_\chi - m_{A'}$  combination. The efficiency is calculated for events where the proton recoil energy is greater than 20 MeV. In the  $\chi - e^-$  events, where the e.m. showers produced inside

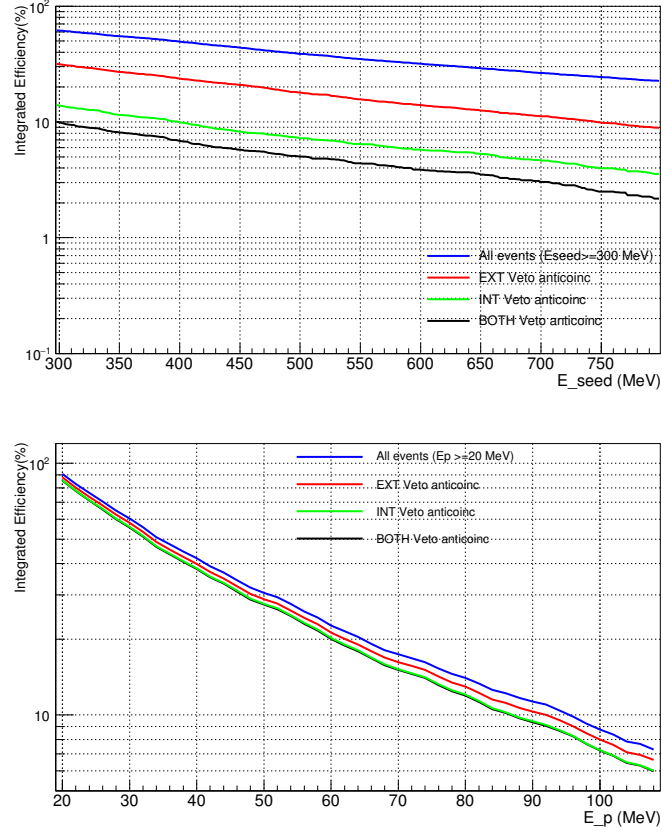


Figure 23: Top panel: Integrated detection efficiency for  $\chi - e^-$  scattering events with  $E_{e^-} > 300$  MeV,  $m_\chi = 30$  MeV and  $m_{A'} = 90$  MeV, as a function of  $E_{seed}$ . The blue curve indicates the efficiency obtained by requiring the presence of a seed with an energy deposited greater than 300 MeV. The red, green and black curves are the efficiencies when we also require the anti-coincidence of the outer, inner or both vetos, respectively. In the simulations we assumed a 1% inefficiency for each veto detector. Bottom panel: Integrated detection efficiency for  $\chi - p$  scattering events with  $E_p > 20$  MeV and for the same  $m_\chi - m_{A'}$  combination.

the detector have a sizable probability to fire a veto detector, the anticoincidence conditions reduce the efficiency by a factors of  $3/5$ . As expected, on the other side, the low recoil energy of the protons result in an efficiency which is only slightly reduced when we impose the absence of any signal in the veto detectors.

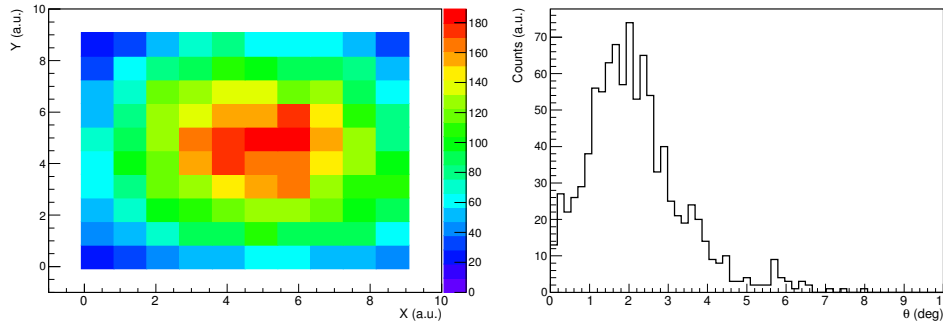


Figure 24: Left panel: an  $(x,y)$  view of the calorimeter where each square represents one crystals. The color scale indicates, in arbitrary units, the number of times a crystal is fired for  $\chi - e^-$  scattering events. Right panel: Angular distribution of the e.m. showers with respect to the beam direction.

### 4.3 Beam related background

The beam-related background was studied with a multi-step approach, focusing first on the potential background for the electron recoil measurement and then on nuclear recoil. In the first case, we consider particles with energy of the order of 500 MeV or higher, while in the second case particles with energy greater than 10 MeV.

To evaluate these backgrounds, the interaction of the 11 GeV electron beam in the dump was simulated and the flux of secondaries was studied as a function of the distance from the dump. For this purpose, the flux of particles was sampled over planes perpendicular to the beam direction as shown in Fig. 25. Since the simulation of the electromagnetic shower produced by the electron beam is very intensive in terms of CPU usage, with this approach it is not possible to accumulate a statistics comparable with that expected for the present experiment ( $\sim 10^{22}$  EOT). A total of  $\sim 0.5 \cdot 10^9$  11 GeV EOT were simulated. The resulting particle fluxes for the 500 MeV and 10 MeV thresholds are shown in Fig. 26. In these plots,  $Z = 0$  corresponds to the upstream end of the aluminum dump, while the detector is located at  $Z = 20$  m. Neutrinos are the dominant contribution to the overall particle flux. With the 500 MeV threshold, we also observe muons and neutrons that reach the iron absorber, while no photons are found. On the other hand, with the lower threshold a non-zero photon flux is observed. With this statistics, the only particles that are found reaching the detector area are  $\nu$  and  $\bar{\nu}$ , predominantly from pion and muon decays at rest. This is shown by the energy spectrum of the different neutrino species reported on the left panel of Fig. 27. Pion decays at rest result in a monochromatic set of  $\nu_\mu$  and  $\bar{\nu}_\mu$  of 30 MeV. Neutrinos from  $\mu$  decay share a total energy of 105.1 MeV ( $M_\mu - M_e$ ), which results in an upper limit for the energy of the  $\nu_\mu$  and  $\nu_e$ , and of their



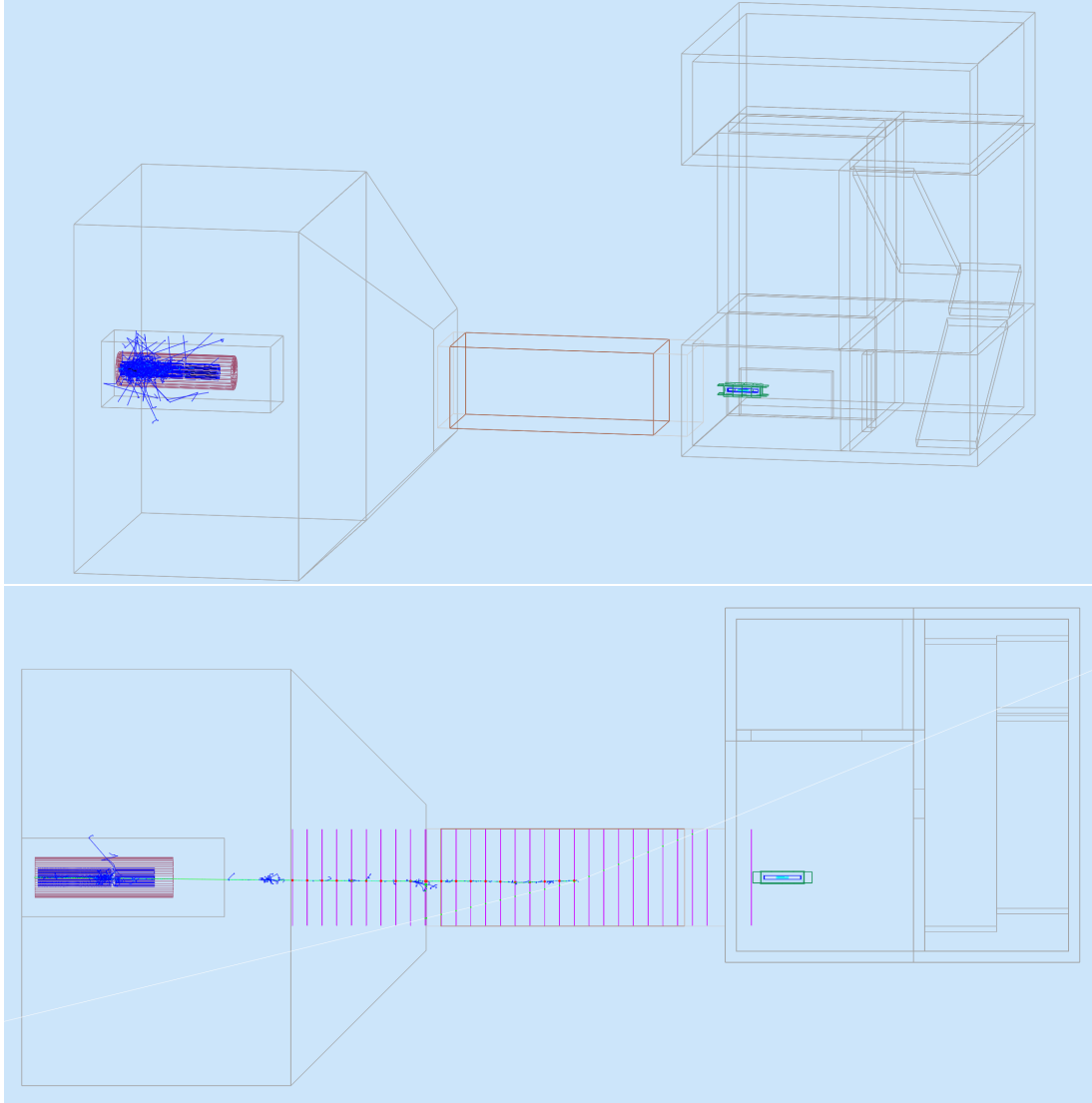


Figure 25: GEANT4 visualization of the electromagnetic shower produced by a 11 GeV electron in the dump (top) and of a 10 GeV muon (bottom). The vertical magenta lines indicate the position of the planes where the secondary flux is sampled.

anti-particles. The origin of these neutrinos inside the beam-dump are shown in the right panel of Fig. 27.

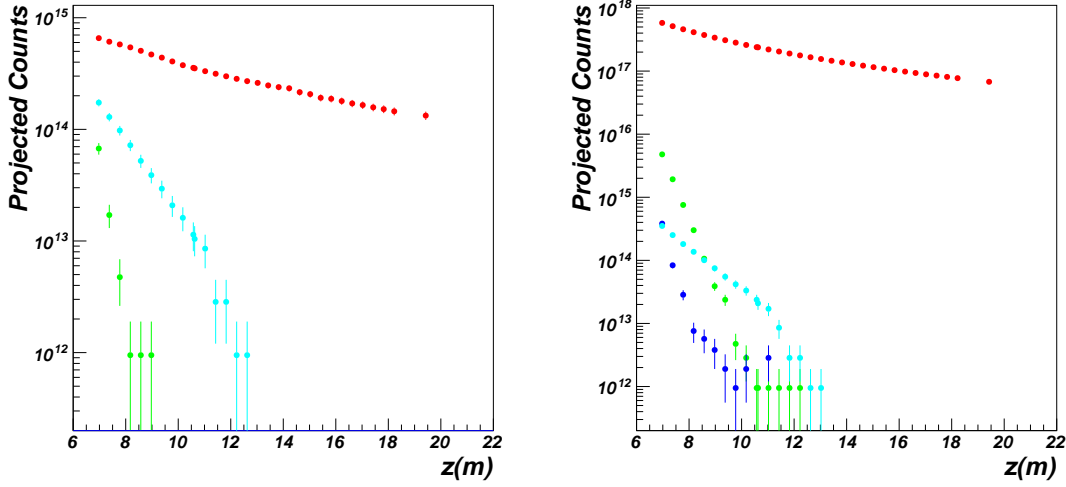


Figure 26: Number of secondary particles produced by the interaction of the 11 GeV electrons as a function of the distance from the upstream end of the dump. The reported counts are normalized to  $10^{22}$  EOT. The left and right plots show the results with a 500 MeV and 10 MeV threshold on the particle energy, respectively. The different colors correspond to different particle types: neutrinos in red, muons in cyan, neutrons in green and photons in blue.

#### 4.3.1 Beam-related background for electron recoil

To evaluate the expected background for the electron recoil measurement, we first evaluated the contribution from neutrinos. As shown by the left panel of Fig. 26, the expected number of neutrinos is of the order of  $\sim 1.7 \cdot 10^{14}$ . These are mostly  $\nu_\mu$  and  $\bar{\nu}_\mu$ , with only about 3-4%  $\nu_e$  and  $\bar{\nu}_e$ . In this energy range, neutrinos interact mostly via charged current, with the dominant processes being quasi-elastic scattering and resonance production on the nucleon, and cross sections of the order of  $\sigma_{\nu N} \sim 10^{-38} \text{ cm}^2$  [54]. These neutrinos can therefore scatter in the BDX detector, producing a muon or an electron of similar energy that can be detected. Muons with energy of the order of hundreds of MeV will lose energy via ionization leaving a “track” in the detector that can be distinguished from the electron recoil signal. Electrons will instead induce an electromagnetic shower, resulting in the same signature of the  $\chi$  interaction. The expected rate of such electrons produced by neutrino interaction can be estimated as:

$$N_{BG}^\nu(E_\nu \geq E_{min}) = N(\nu_e, E_\nu \geq E_{min}) \sigma_{\nu N} \mathcal{N}_A \rho_{CSI} L \epsilon_e \quad (12)$$

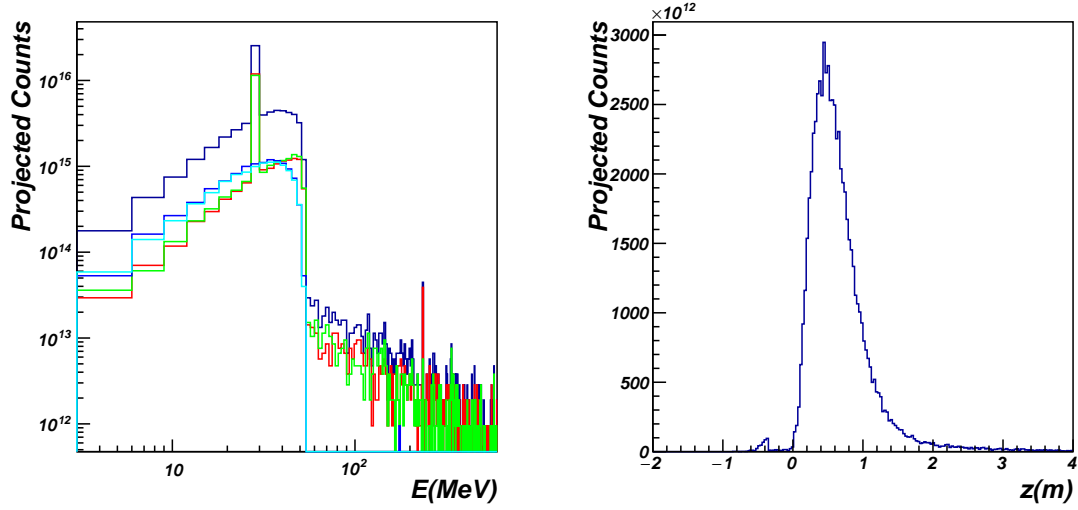


Figure 27: Left: energy spectrum of beam-related neutrinos reaching the detector; the dark-blue histogram shows the total spectrum while the red, green, blue and cyan histograms correspond to the  $\nu_\mu$ ,  $\bar{\nu}_\mu$ ,  $\nu_e$  and  $\bar{\nu}_e$  spectra, respectively. Right: the vertex of the decaying primary particles ( $\mu$  and  $\pi$ ) starting at the beam-dump location and extending for 1m downstream. The reported counts are normalized to  $10^{22}$  EOT.

where  $N(\nu_e, E_\nu \geq E_{min})$  is the number of  $\nu_e$  and  $\bar{\nu}_e$ , with energy above a minimum value  $E_{min}$  corresponding to the chosen electron-recoil threshold, that reach the detector,  $\rho_{CsI} = 4.51 \text{ g/cm}^3$  is the CsI density,  $L = 260 \text{ cm}$  is the detector length and  $\epsilon_e$  is the efficiency for the detection of the electromagnetic shower that we have assumed to be of the order of 20%, similarly to the efficiency estimated for the  $\chi$ -induced electron recoil showers. The results for different values of  $E_{min}$  are reported in Table 3 and indicate that the neutrino background for  $10^{22}$  EOT is  $\mathcal{O}(10)$ .

While this is an irreducible background for the experimental configuration we are considering, additional simulation studies we performed indicate that the neutrino production rate would be strongly suppressed if the dump was made by high  $Z$  material instead of aluminum: with the same dump layout but replacing aluminum with copper or tungsten for instance, the estimated neutrino background would be a factor 5 or 20 lower, respectively, i.e. of  $\mathcal{O}(2)$  or  $\mathcal{O}(1)$ . The replacement of the dump material may be therefore considered for possible upgrades of the experimental setup.

Additional background that may affect the electron-recoil measurement, may come from energetic muons or neutrons. As shown by the left panel of Fig. 26, the number of neutrons decreases very rapidly as the distance from the dump increases and, performing an exponential extrapolation of the projected counts, we estimated that

$E_{min}$	$N(\nu_e, E_\nu \geq E_{min})$	$N_{BG}^\nu(E_\nu \geq E_{min})$
200 MeV	$7.7 \cdot 10^{12}$	11
250 MeV	$7.4 \cdot 10^{12}$	11
300 MeV	$7.0 \cdot 10^{12}$	10
350 MeV	$6.6 \cdot 10^{12}$	9

Table 3: Beam-related background for the electron-recoil measurement due to neutrinos. The reported counts are for  $10^{22}$  EOT.  $N(\nu_e, E_\nu \geq E_{min})$  and  $N_{BG}^\nu(E_\nu \geq E_{min})$  correspond to the number of  $\nu_e$  and  $\bar{\nu}_e$  that reach and interact in the detector, respectively. In estimating the number of neutrino interactions, we conservatively used a cross section of  $10^{-38}$  cm<sup>2</sup>, independently of the minimum energy.

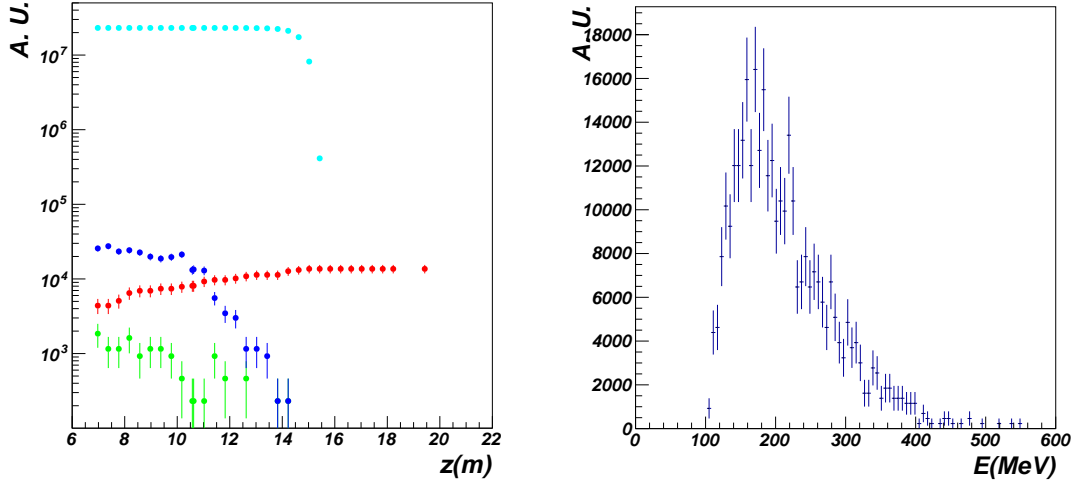


Figure 28: Left: neutrino (red), neutron (green), gamma (blue) and muon (cyan) fluxes as a function of the distance from the dump resulting from the simulations of 10 GeV muons. Here only particles with kinetic energy greater than 500 MeV are considered. Note that the BDX detector would be located at 20 m from the dump. Right: muon energy spectrum at  $Z \sim 16$  m

no neutrons with energy of the order of hundreds of MeV would reach the detector. Muon counts decrease more slowly, consistently with the high penetrating power of these particles, and range out at  $Z \sim 12$  m. To further check whether high energy muons or their secondaries can reach the detector area, 10 GeV muons, that could be produced via pair production by high energy photons, were generated at the center of

the dump and the flux of particles produced was sampled as a function of the distance from the dump as in the original simulations. The resulting particle profiles shown in Fig. 28 indicate that the muon range is of the order of 16 m, i.e. significantly smaller than the distance between the detector and the dump. Close to the maximum range, the energy of the muons is strongly degraded being less than 300 MeV in average at  $Z \sim 16$  m. The flux of secondaries produced by the 10 GeV muons, with the exception of neutrinos, dies within a similar distance.

### 4.3.2 Beam-related background for nuclear recoil

Potential contributions to the nuclear recoil measurement are due to particles with kinetic energy greater than the measurement threshold of 10 MeV. As shown by the right panel of Fig. 26, the most abundant particles are also in this case neutrinos, with total projected counts of  $\sim 7 \cdot 10^{16}$  for  $10^{22}$  EOT and approximately equal counts for the different neutrino species. Neutrinos with energy in the range 10-100 MeV mainly interact by CC interaction ( $\bar{\nu}A \rightarrow e^+A'$ ) with a cross section of about  $\sigma_{\bar{\nu}A} \sim 10^{-41} \text{ cm}^2$ . Assuming a detection efficiency of  $\epsilon_{e^+} = 5\%$  with 10 MeV threshold, the corresponding background rate can be estimated as:

$$N_{BG}^{\nu}(E_{\nu} = 10 - 100 \text{ MeV}) = N(\nu_e, E_{\nu} = 10 - 100 \text{ MeV}) \sigma_{\bar{\nu}A} \mathcal{N}_A 1/A \rho_{CSI} L \epsilon_{e^+} \sim 0.25, (13)$$

which is negligible with respect to the background counts expected from higher energy neutrinos estimated in the previous section.

Other contributions could arise from photons and neutrons that may propagate through the iron absorber. Based on the simulations of the 11 GeV electron simulation, we found that a significant fraction of the photons and neutrons that are found at the largest  $Z$  values are muon secondaries. To verify whether these could reach the detector area, a dedicated simulation study was performed generating muons at  $Z = 16$  m with energy corresponding to the average of the spectrum shown in the right panel of Fig. 28: for 1 M muons generated, we observed no photons and neutrons exiting the iron absorber. Another estimate can be performed extrapolating the particle counts shown in the right panel of Fig. 26. For photons, the exponential extrapolation indicate that the expected counts at the detector position are less than  $10^{-5}$  for  $10^{22}$  EOT, i.e. negligible with respect to other contributions. We should note that, performing this extrapolation, we are not considering the degradation of particle energies as they propagate in the absorber. To take this into account for neutrons, we performed additional simulation studies with the following procedure. We selected the largest  $Z$  position where significant neutron statistics was found and we simulated mono-chromatic neutrons, with energy corresponding to the maximum kinetic energy previously observed, originating at the same position and traveling along the

$Z$  axis. This procedure was repeated twice, allowing us to study the neutron propagation probability to the detector area. The result, shown in Fig. 29, indicate that the expected neutron counts in the detector area are negligible.

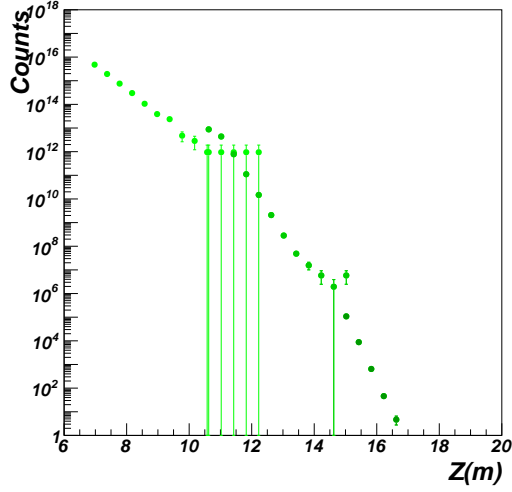


Figure 29: Projected neutron counts as a function of the distance from the dump upstream end. See the text for details on the simulation procedure. The estimated counts in the detector area, i.e.  $Z = 20$  m, are negligible with respect to other contributions.

## 4.4 Beam unrelated background

Beam-unrelated background is mainly due to cosmic neutrons, cosmic muons and their decay products, including rare decays of muons producing gamma's between the passive shield and the active veto. Both direct cosmic flow (muon and neutron) and secondaries particles (muon, neutron and gamma) contribute to the beam-unrelated background count rate in the detector.

### 4.4.1 Cosmic background estimate

The cosmogenic background rates expected in the BDX experiment have been evaluated by extrapolating the results obtained with the BDX prototype in Catania LNS measurements. The similar experimental set-up (including overburden) as well as a full prototype that incorporates all the elements of the BDX detector (active veto's, lead shielding, BaBar CsI(Tl) crystals) provide a solid base for a realistic, although conservative, estimate of the expected rates. Details of the experimental conditions

Energy threshold	Extrapolated rate	Projected counts (285 days)
200 MeV	$(3.0 \pm 1.2) \cdot 10^{-5}$ Hz	$(740 \pm 300)$
250 MeV	$(2.3 \pm 1.0) \cdot 10^{-6}$ Hz	$(57 \pm 25)$
300 MeV	$(1.9 \pm 0.9) \cdot 10^{-7}$ Hz	$(4.7 \pm 2.2)$
350 MeV	$(1.5 \pm 0.9) \cdot 10^{-9}$ Hz	$(0.037 \pm 0.022)$

Table 4: The expected cosmogenic background rates on the BDX detector when the IV anti-coincidence is requested.

Energy threshold	Extrapolated rate	Projected counts (285 days)
5 MeV	$(37 \pm 1) \cdot 10^1$ Hz	$(9.1 \pm 0.2) \cdot 10^9$
10 MeV	$(1.5 \pm 0.1)$ Hz	$(3.7 \pm 0.2) \cdot 10^7$
20 MeV	$(0.5 \pm 0.1)$ Hz	$(1.2 \pm 0.2) \cdot 10^7$
50 MeV	$(0.3 \pm 0.1)$ Hz	$(0.7 \pm 0.2) \cdot 10^7$

Table 5: The expected cosmogenic background rates on the BDX detector when the IV and the OV anti-coincidence is requested.

and data analysis are reported in Appendix B. The extrapolation has been performed by scaling the experimental rates of a single crystal to the 800 crystals comprising the full detector. This is certainly an upper limit on the expected rates since this assumes crystal-to-crystal fully uncorrelated counts, which overestimates the case for  $\chi$ -e scattering. Tables 4 and 5 report some of the rates at different threshold energies for high energy and low energy, which are relevant for  $\chi$ -e scattering and  $\chi$ -nucleon, respectively. In the tables there is also the projection of the counts integrated over the expected beam-on time. For energy thresholds higher enough, between 300-350 MeV, the number of cosmogenic background counts reduces to zero. Thus, by choosing the appropriate energy threshold for the  $\chi$ -e scattering channel we could consider zero background. However, in order to be conservative, in the next Section we will determine the sensitivity and the reach of the proposed BDX experiment considering  $N^{\text{cosmic}} = 3$ .

#### 4.4.2 Background reduction strategies

**Time-Correlation** Beam-unrelated background can be, in principle, rejected by requiring a time coincidence between the RF signal and the event recorded by the

detector. The background reduction factor,  $R$ , can be expressed as the ratio between the time coincidence window width ( $3\sigma_T$ ) and  $\Delta T$ :

$$R = \frac{3\sigma_T}{\Delta T} \quad (14)$$

Considering the time response of CsI(Tl) crystals, the almost-CW structure of the CEBAF beam does not allow to take full advantage of this technique. In fact the bunch separation expected with the 12 GeV operations is  $\Delta T=4.0$  ns to be compared with the measured time resolution of BDX detector of  $\sigma_T \sim 6$  ns for 30 MeV deposited energy. As already mentioned, a detector based on inorganic scintillators with such a good time resolution would be prohibitive in term of costs (at least for a first generation of beam dump experiments) while the use of faster organic scintillator would lead to a significant increase of the detector footprint (a factor of 5 in length) impacting on the size of the new facility. Some dense crystals, such as the  $\text{BaF}_2$  do have a fast scintillation component in the range of  $\sim 1$  ns although with lower light output ( $\sim 10^3 \gamma/\text{MeV}$ ) and peaked in UV region ( $\sim 220$  nm) but further studies are requested to demonstrate the feasibility. If we stick to the current detector design, a significant background reduction (a factor of 5-10) would only be achieved by running the CEBAF machine in a different mode with a beam macro-structure of  $1\mu\text{s}$  and keeping the bunch micro-structure of 250 Mhz, preserving the average current of 40-50  $\mu\text{A}$ . While we are investigating the technical feasibility of this option with the Accelerator Division, we are aware that this would probably require a dedicated beam time preventing BDX to run parasitically to the already approved Hall-A physics program. If technically possible this would represent a valuable alternative for a dedicated, cosmogenic background-free second-generation beam-dump experiment at Jefferson Lab.

In the following, we are not considering any background rejection due to the timing cuts.

**Directionality** Beside time-correlation, directionality could help in reducing the cosmogenic background. In fact the angular distributions of cosmic muons (and their decay products) and cosmic neutrons are peaked around the vertical (the angular distributions are proportional to  $\cos^2 \theta$  and  $\cos^3 \theta$  respectively) while the  $\chi$ s are expected to follow the beam direction. Furthermore, MC simulations indicate that an electromagnetic shower produced inside the detector, pointing downstream, such as the one produced in the  $\chi$ -e scattering, has a peculiar shape, direction and energy distribution easily distinguishable from a cosmic hit (see e.g. Fig. 24). Thus, a thorough analysis of background events collected during the experiment will certainly allow to reject some of the cosmic background. For example, this capability is heavily exploited by



the DRIFT-BDX detector to enhance sensitivity, as described in Appendix C. However in the following, keeping a conservative attitude, we are not considering any background suppression associated with directionality using the calorimeter.

## 5 Expected results

In this Section we present the expected reach of the BDX experiment. Results are reported as upper limit on exclusion plot. The region above the lines is excluded since the model, with the chosen parameters, predicts a number of counts larger than the observed. Each line corresponds to a model-predicted yield comparable or exceeding the expected background. This is true in case of null results. If any excess is observed, a thorough statistical analysis will be necessary to claim a positive result. Leaving this discussion to the future, in the last section we just report a list of systematic checks that the BDX experiment will be able to perform to corroborate any possible findings.

### 5.1 BDX expected reach

Here we consider an experimental set-up that takes advantage of the maximum beam current available at JLab ( $\sim 65\mu\text{A}$ ) compatible with the Hall-A beam-dump power limit ( $\sim \text{MW}$ ), at the maximum available energy (11 GeV) for a full parasitic run that will collect  $10^{22}$  EOT. This would correspond to a total time of  $2.5 \cdot 10^7$  s (285 calendar days or 41 weeks).

#### 5.1.1 Expected signal and measured background

In order to place limits, we must determine the uncertainties in the background yields. The cosmic-ray rate will be determined when the beam is off, both during accelerator running periods (assuming a nominal 50% delivery) and also between running periods when the accelerator is off. We assume that the experiment will run over a period of about 4 years (208 weeks of calendar time), resulting in 167 weeks of data when the beam is off and 41 weeks with beam on. The beam off data will be used to determine the average cosmic-ray background,  $N_{BG}^{cosmic}$ , and subtract it from the beam on data. The beam related backgrounds, primarily due to  $\nu_e$  interactions, will be calculated using MC and normalized to the measured rate of  $\nu_\mu$  interactions, which are almost 30 times higher. The uncertainty in the calculation of the beam background,  $\sigma_{BG}^{beam}$ , will dominate the limits that can be set. The estimated excess of events above background is given by

$$N_{excess} = N^{beam} + N^{cosmic} - N_{BG}^{beam} - N_{BG}^{cosmic} \quad (15)$$

$$\sigma_{excess} \simeq \sqrt{N^{beam} + N^{cosmic} + (\sigma_{BG}^{beam})^2 + \frac{1}{4}N^{cosmic}}, \quad (16)$$

where the total number of registered counts,  $N = N^{beam} + N^{cosmic}$ , is separated out into its two components for ease of discussion. The estimated beam and cosmic-

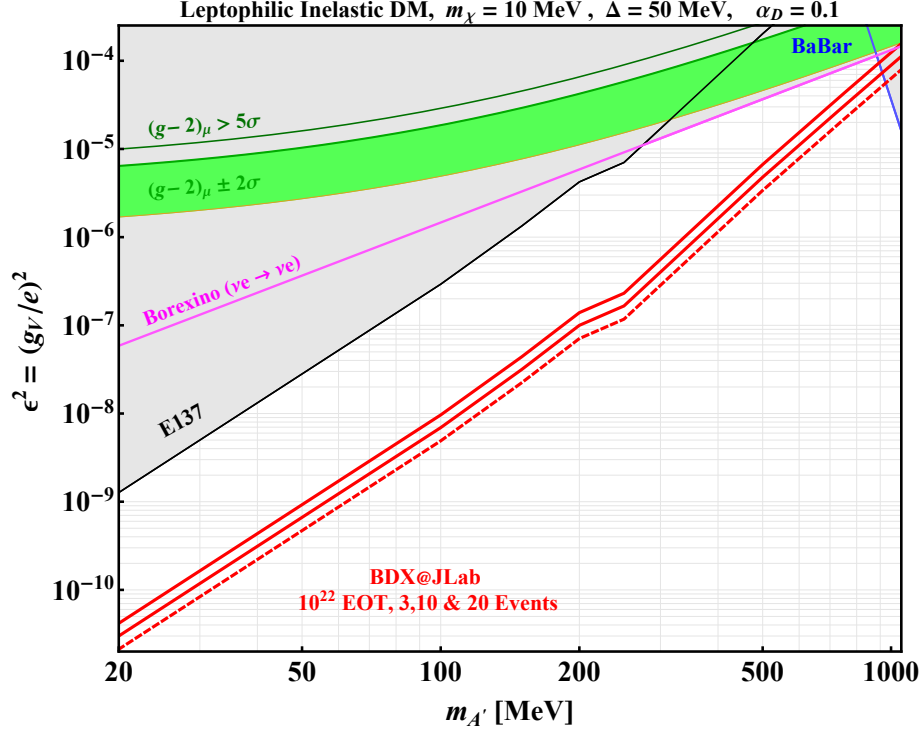


Figure 30: Red curves show 3, 10, and 20 event BDX yield projections for leptophilic scenario.

ray backgrounds are denoted by consistent notation. The cosmic-ray background is estimated from beam off data assuming we have collected four times the amount of beam on.

Curves on the exclusion plots report the predicted counts by the models described in Sec. 2. They all include the efficiency evaluated in Sec. 4.2.3 for the detection of an electromagnetic shower with energy deposited in the seed crystal greater than 300 MeV. The region on the plots below the curves is excluded at the  $2\sigma$  level when

$$N_{Model} > 2\sigma_{excess} \sim 11 - 17 \text{ counts}, \quad (17)$$

where we have taken

$$N^{beam} = 8 \quad (18)$$

$$N^{cosmic} = 3 \quad (19)$$

$$\sigma_{BG}^{beam} \sim (0.5 - 1) \times N^{beam} \quad (20)$$

The exclusion plots indicate levels of sensitivity between 3 and 20 counts, which span the expected range given above.

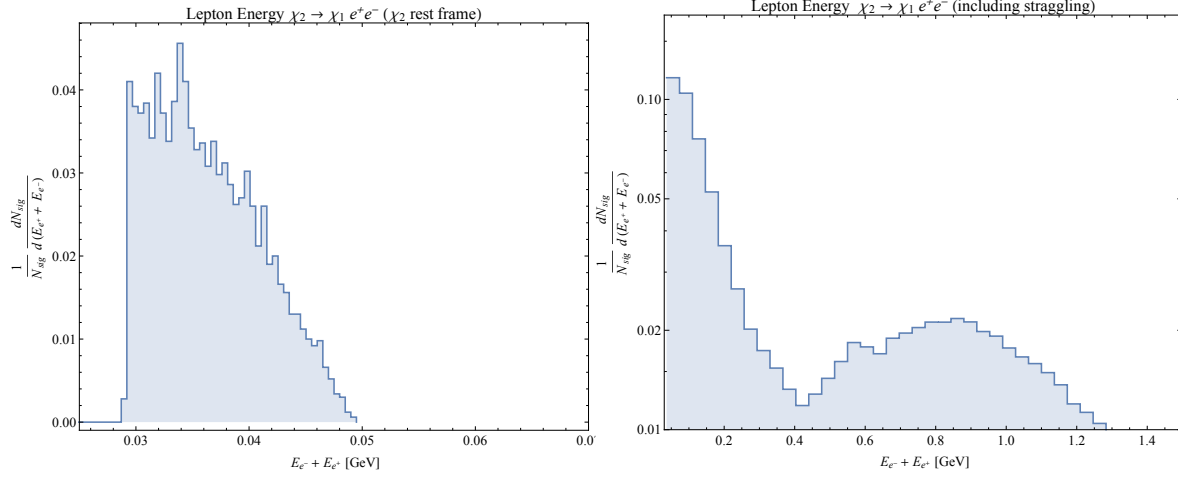


Figure 31: Energy spectrum for  $e^+e^-$  pair from the inelastic signal inside the BDX detector. For concreteness, here we assume  $m_{\chi_1} = 10$  MeV,  $m_{\chi_2} = 60$  MeV,  $m_{A'} = 100$  MeV,  $\alpha_D = 0.1$  and  $\epsilon = 8.3 \times 10^{-5}$ , which corresponds to the BDX 10 event sensitivity for this parameter point in Fig. 30.

It is worth pointing out that the energy threshold for signal identification (and beam-related background) as well as the number of counts related to the cosmic background will be tuned during the experiment to the most favourable value that maximises the BG/SIGNAL ratio. In fact, with the proposed BDX data acquisition scheme, the entire detector readout (full waveform of crystals and veto's) will be triggered by any signals in any crystals corresponding to an energy deposited of less than 1 MeV preserving for the off-line analysis the most complete information about every collected event.

Thus the experiment will be detecting nucleon recoil events with thresholds below 10 MeV. However, our present estimation of cosmic-ray backgrounds indicate that the sensitivity of this reaction is not competitive with the primary search for electron recoils. Nevertheless, the data will be acquired and analysed to provide checks and complementary information to the main signal.

### 5.1.2 The BDX reach

In case of no positive observation, the accumulated data would provide very stringent limits on the DM parameters space. Figure 30 shows the BDX sensitivity to a leptophilic  $U(1)_{e-\mu}$  gauge boson ( $A'$ ) coupled to a Majorana current of DM states charged under  $e - \mu$  number with masses  $\chi_1 = 10$  MeV and  $\chi_2 = 60$  MeV. In this scenario, the gauge boson is radiatively produced in electron-nucleus collisions in the

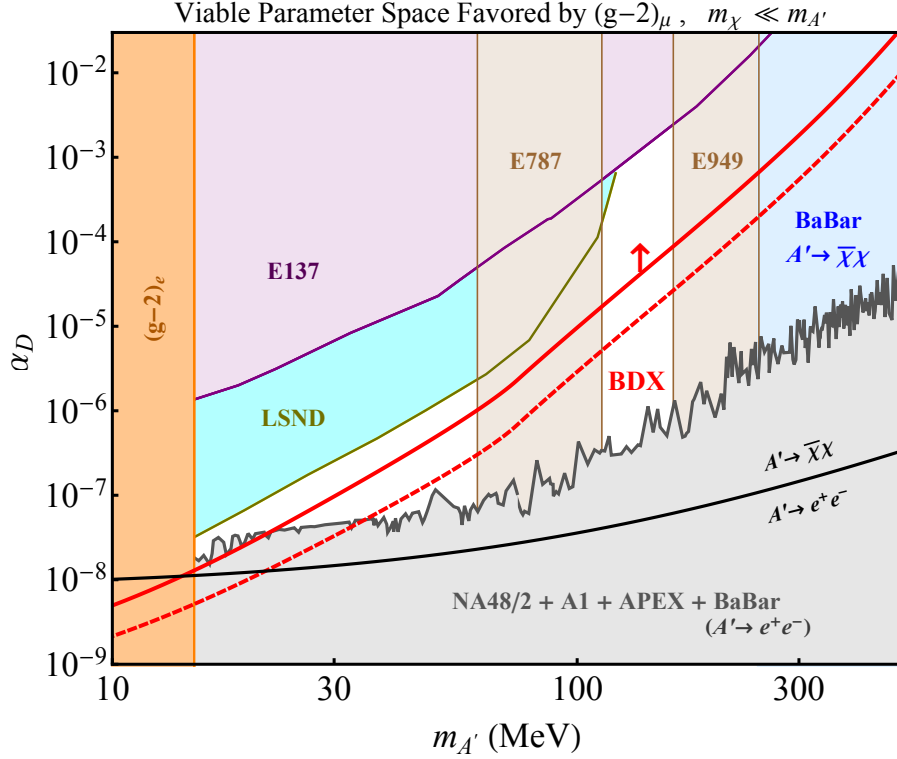


Figure 32: Red curves show 3 and 10 event BDX yield projections for a dark-photon ( $A'$ ) whose kinetic mixing parameter  $\epsilon$  is conservatively fixed to the *smallest* value that resolves the longstanding  $(g - 2)_\mu$  anomaly. The black curve represents the  $\text{Br}(A' \rightarrow e^+e^-) = \text{Br}(A' \rightarrow \chi\chi)$  contour. Testing the remaining unshaded parameter space suffices to discover a dark photon responsible for the anomaly, or to decisively rule out such an explanation regardless of how the  $A'$  decays. The parameter space covered by BDX is the area above the red lines, as indicated by the arrow.

beam-dump and decays promptly to yield  $\bar{\chi}_1\chi_2$  pairs. The heavier  $\chi_2$  state is unstable and short lived, so the flux of DM particles at the detector consists entirely of  $\chi_1$  states, which up-scatter off detector electrons, nucleons, and nuclei, thereby converting to  $\chi_2$  states which decay via  $\chi_2 \rightarrow \chi_1 e^+e^-$  transitions and deposit significant ( $\sim$  GeV) electromagnetic energy inside the detector. The energy for  $e^+e^-$  pair from the inelastic signal inside the BDX detector is shown Fig. 31.

We now focus on the parameter space that can explain the discrepant  $(g - 2)$  of the muon. Figure 32 shows the BDX projection for  $10^{22}$  EOT in terms of the  $A'$ -DM coupling  $\alpha_D$  as a function of dark-photon mass in the  $m_\chi \ll m_{A'}$  limit. We also show the excluded parameter space from both visibly decaying ( $A' \rightarrow e^+e^-$ ) and invisibly decaying ( $A' \rightarrow \chi\chi$ ) constraints; for sufficiently small  $\alpha_D$ , the visible decays dominate

so the constraint is independent of  $\alpha_D$ . Note that the parameter space for a purely visibly decaying dark photon is completely ruled out, so the only *viable* explanation is in the predominantly invisibly decaying region (white, unshaded); everything below is excluded.

Figure 33 shows the BDX yield projections for electron scattering with a 300 MeV energy threshold for thermal relic DM in two representative scenarios. For both plots, the relic target is proportional to the variable on the  $y$  axis, so it does not change as the assumption on  $\alpha_D$  varies, but some experimental bounds do shift since they constrain a different combination of couplings. Nonetheless, for  $\alpha_D \sim \mathcal{O}(1)$ , all the gaps in the parameter space are revealed; making  $\alpha_D$  smaller only moves the projections down further, so the most conservative choice corresponds to a large, perturbative  $\alpha_D = 0.5$ ; larger values require UV completions with additional field content to avoid strong coupling near the GeV scale [55]. In the top plot, we show the projected sensitivity to thermal relic DM coupled to a leptophilic  $U(1)_{e-\mu}$  gauge boson ( $A'$ ). Here we plot  $y = \alpha_D \epsilon^2 (m_\chi/m_{A'})^4$  vs.  $m_{A'}$  where  $\epsilon \equiv g_V/e$ ,  $g_V$  is the  $U(1)_{e-\mu}$  gauge coupling, and  $\alpha_D \equiv g_D^2/4\pi$  where  $g_D$  is the  $A'$ -DM coupling constant. Also plotted is the thermal relic target for the direct annihilation regime  $m_{A'} > m_\chi$ . The bottom panel corresponds to the expected sensitivity to a dark photon,  $A'$ . Here  $\alpha_D$  is the dark photon's coupling to the DM and  $e\epsilon$  is the effective coupling between  $A'$  and charged SM fermions.

In Fig. 34 we show the BDX reach in the parameter space  $\epsilon^2 - m_{A'}$  (for  $m_\chi \ll m_{A'}$ ). We show this parameter space for  $\alpha_D = 0.1$  and  $\alpha_D = 10^{-7}$  to illustrate how different constraints scale with different assumptions about the  $A'$ -DM coupling – note that for sufficiently small values of  $\alpha_D$ , invisible decay bounds weaken whereas the  $(g-2)_\mu$  favored region remains unaffected, since it is independent of the DM coupling. Thus, for the remaining portion of the viable parameter space, an  $A'$  explanation for this anomaly is revealed for  $\alpha_D \sim 10^{-6}$  and smaller as displayed in Fig. 32. However, for even smaller values  $\alpha_D \sim 10^{-10}$ , the value of  $\epsilon$  required to explain the anomaly is sufficiently large that the  $A'$  branching ratio is dominated by the visible channel  $A' \rightarrow e^+e^-$ , for which the  $(g-2)_\mu$  explanation has already been ruled out (as shown in lower gray shaded region in Fig. 32, so BDX has the potential to test nearly all of the remaining dark photon parameter space consistent with a dark-photon solution to this discrepancy.

Finally, in Fig. 35 we show the same  $\epsilon^2$  vs.  $m_{A'}$  parameter space, but for a value of  $m_\chi$  below the kinematic threshold of LSND, so that constraint does not bound this slice of the parameter space.

In all the aforementioned scenarios the region potentially covered by JLab would therefore significantly extend the parameter space already excluded by previous experiments.

## 5.2 Systematic checks

In case of positive result, there is a list of possible checks that can be done to confirm that any observed excess of counts would be related to a real signal.

- **Measurements during shielding installation:** Measurements of beam-related and cosmi-ray backgrounds can be made during construction as material is added to shield the detector both from the beam stop and from cosmic-rays. These measurements can be used to validate the MC calculations.
- **Beam-related backgrounds:** due to the expected forward-peaked kinematics of the  $\chi$ , a measurement off-axis ( $\sim 1\text{m}$ ) will provide a check that the detected signal is really associated to the electron beam interactions.
- **Cosmic background:** a precise measurement of the cosmic background in the detector will be possible by accumulating data during the about 4 years of experiment time. In this way a more precise subtraction of the cosmic background will be possible.

The proposed BDX experiment, tacking advantage of the high intensity, high energy electron beam available at JLab has the unique capability of extending the possible reach by order of magnitude with respect to the previous (un-optimized) measurements getting close to the unreducible background due to the neutrinos produced in the beam-dump interaction. The BDX experiment at Jlab may represent the ultimate beam-dump experiment with an intense electron beam proving a wide category of light DM models.

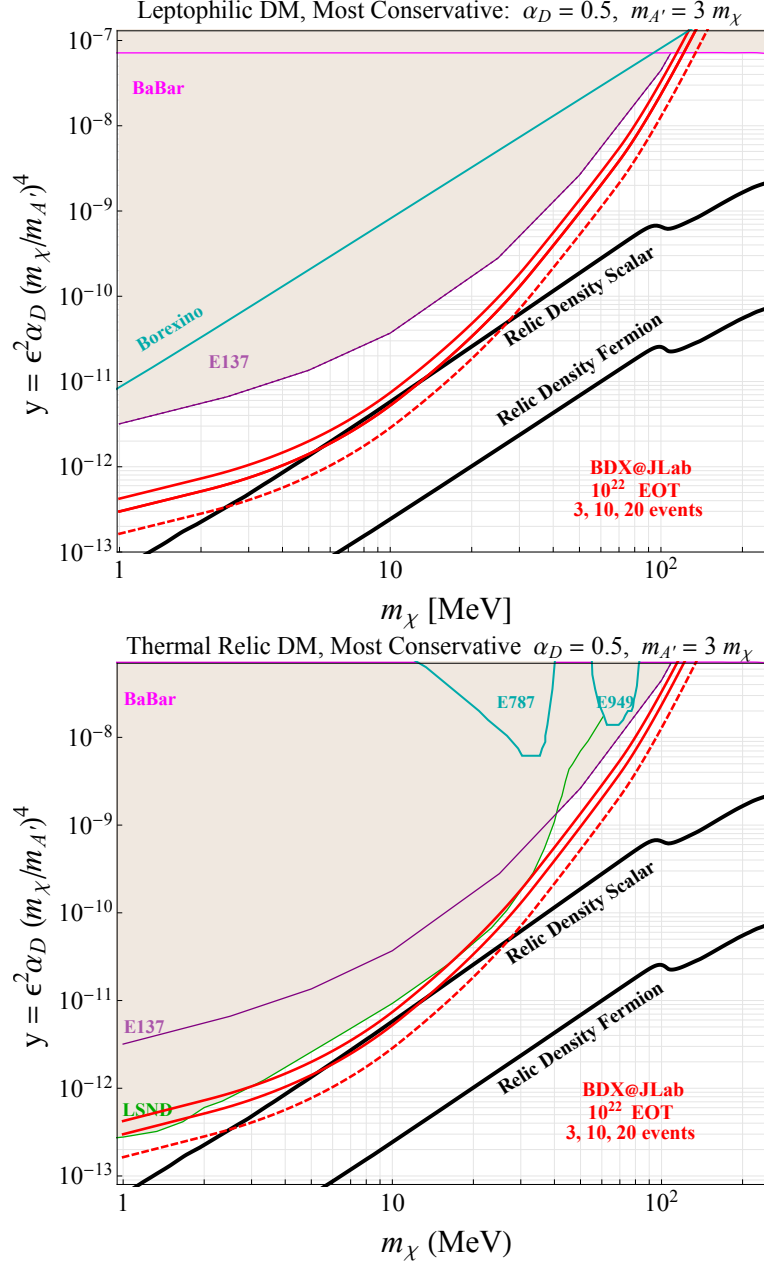


Figure 33: Red curves show 3, 10, and 20 event for BDX yield projections for electron scattering with a 300 MeV energy threshold for thermal relic DM in two representative scenarios. Top: thermal relic DM coupled to a leptophilic  $U(1)_{e-\mu}$  gauge boson ( $A'$ ). Bottom: here the  $A'$  is a kinetically mixed dark photon coupled to the electromagnetic current. Here the thermal target — where the model predicts the correct observed DM abundance — is shown in solid black.



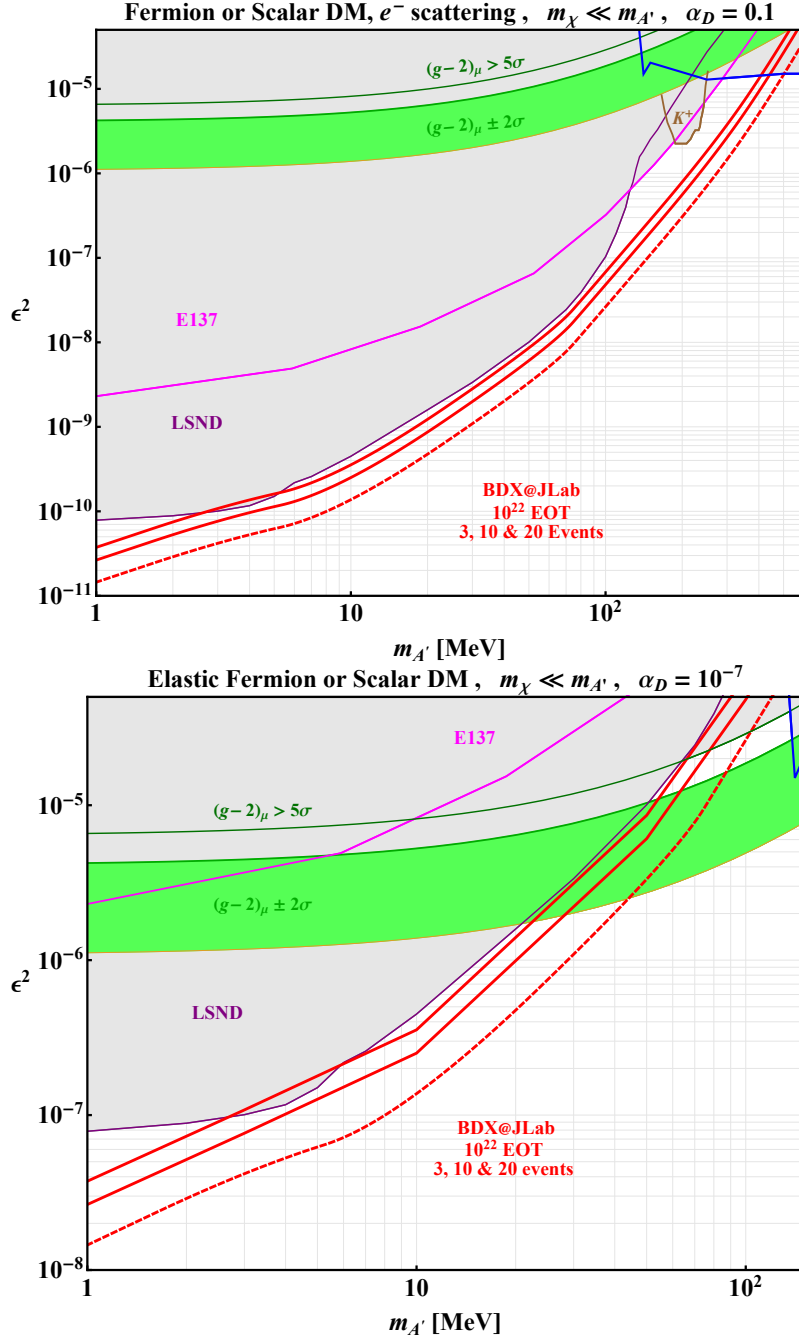


Figure 34: Red curves show 3, 10, and 20 event BDX yield projections for electron scattering with  $10^{22}$  EOT and a 300 MeV recoil energy threshold. Here  $A'$  is a kinetically mixed dark photon coupled to DM with  $\alpha_D = 0.1$  and  $\alpha_D = 10^{-7}$ .

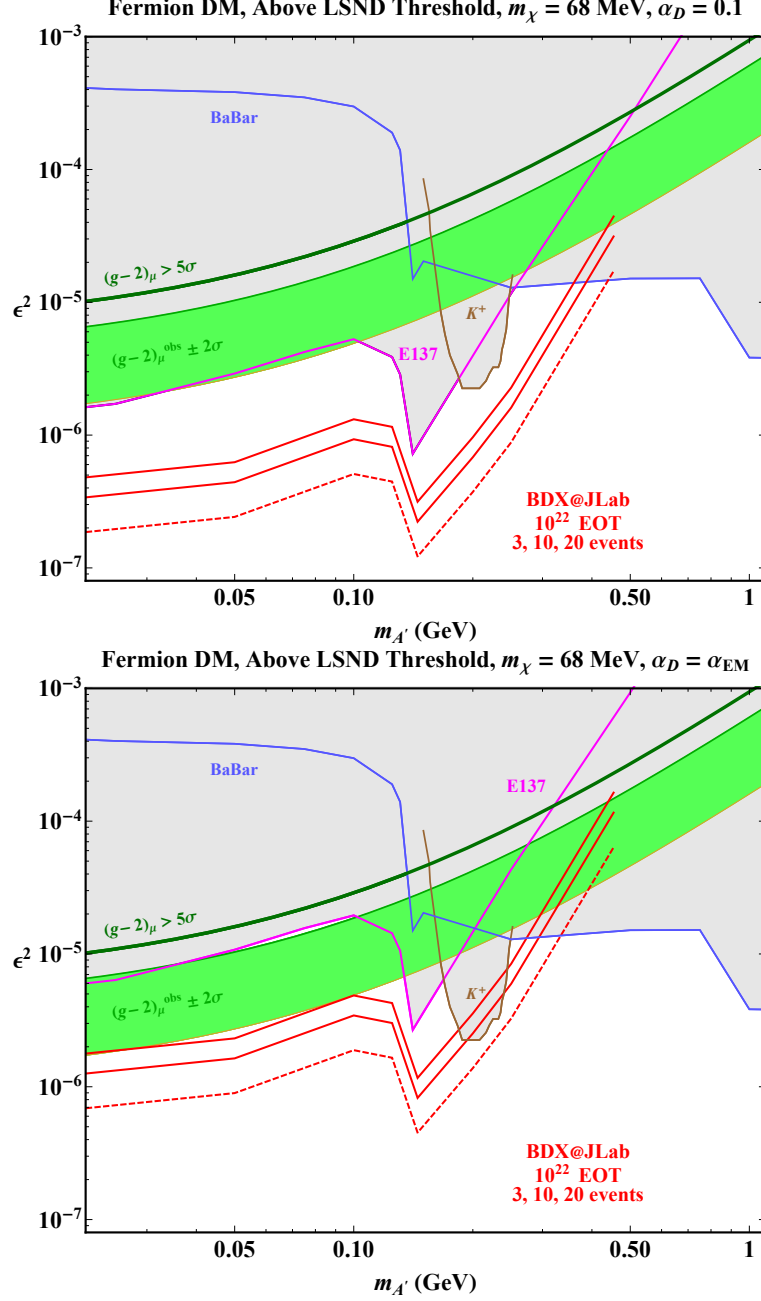


Figure 35: Same as Fig. 34 only here  $m_\chi = 68$  MeV and we adopt  $\alpha_D = 0.1$  and  $\alpha_D = \alpha_{EM}$  for the two panels. This choice of  $m_\chi$  represents the kinematic limit beyond which LSND can no longer produce pairs of  $\chi$  via  $\pi^0 \rightarrow \chi\chi$ . Note that for  $m_{A'} < 2m_\chi$  the dark photon will no longer decay to DM pairs and may be constrained by visible searches, but this is model dependent.

## 6 Summary and Conclusions

We propose to run an experiment to search for weakly interacting particles produced in the interaction of the electron beam in the dump. The Beam Dump eXperiment (BDX) will look for these particles using an electromagnetic calorimeter surrounded by active and passive vetos in a new underground facility located downstream of the Hall-A beam dump. This experiment will have strong, unprecedented sensitivity to dark matter in the MeV – GeV mass range. The experimental setup proposed for BDX at JLab, combining a state-of-the art electromagnetic calorimeter with the high energy and high intensity CEBAF electron beam, will hit the limit of this class of experiment reaching the wall of the *irreducible* background produced by CC interactions of beam-related  $\nu_e$  in the detector.

Searches for particles in this mass range are motivated by models that feature a dark matter particle  $\chi$  whose interactions with the Standard Model (SM) through a new massive dark photon generically appear with strength  $\epsilon$  near  $10^{-4} - 10^{-2}$  [2]. Such models can also explain the persistent  $3 - 4\sigma$  discrepancy between theoretical predictions and experimental observations of the muon’s anomalous magnetic moment.

The experiment would detect the elastic scattering of  $\chi$ s off atomic electrons in a detector situated about 20 m from the beam dump by measuring the electron recoil energies. The experiment would also be capable of accessing complementary information from  $\chi$ -nucleon scattering. Additionally, the BDX experiment would be uniquely suited to look for DM models where the DM scatters inelastically in the detector.

The sensitivity of BDX was evaluated by measuring the cosmic background under conditions similar to those proposed and estimating the beam-related background using GEANT4 MonteCarlo simulations. Results were extrapolated (projected) to the requested accumulated charge of  $10^{22}$  electrons on target. In the absence of a signal, electromagnetic shower thresholds between 0.3 and 0.5 GeV can be used to set limits on the production of dark matter that exceed the expected sensitivity of previous, existing, and proposed experiments by up to two orders of magnitude.

## A Evidence and production of dark matter

The overwhelming evidence for the existence of DM is based on multiple, independent astrophysical and cosmological observations. Stellar rotation curves in galaxies and dwarf-galaxies; the power spectrum of temperature fluctuations in the Cosmic Microwave Background (CMB); the power spectrum of matter density fluctuations; the ratios of light element yields from Big Bang Nucleosynthesis (BBN); the morphology of galaxy cluster collisions; and astrophysical mass measurements based on gravitational lensing, all consistently indicate that 85 % of the matter and 25 % of the total energy of our universe comprises an electrically neutral, non relativistic population of “dark matter” (for a comprehensive review of this evidence, see [56]).

Although the Standard Model (SM) contains several neutral particles, none serves as a viable dark matter candidate. The Higgs boson and neutron are unstable with respective lifetimes of  $\sim 10^{-22}$  and  $\sim 10^3$  sec, so both decay too rapidly to accommodate a cosmologically metastable abundance. Neutrinos, whose masses satisfy  $m_\nu \lesssim 0.1$  eV [10], are relativistic throughout much of cosmological evolution and would have inhibited the formation of large scale structure had they constituted a significant fraction of DM. Thus, the existence of DM is “smoking gun” evidence of physics beyond the SM and uncovering its particle identity is top priority in fundamental physics.<sup>§§</sup>

However, this task remains elusive because the entire body of evidence for dark matter is based on its gravitational influence on visible matter in astrophysical and cosmological contexts. Given the weakness of the gravitational force,  $G_N/G_F \sim 10^{-35}$ , these data are unable to reveal DM’s short distance properties, which remain completely unknown to date. Indeed, absent further assumptions about its non-gravitational interactions or cosmological history, the lower bound on the average DM particle mass is  $m_{\text{DM}} \gtrsim 10^{-22}$  eV; lower masses correspond to de Broglie wavelengths larger than the smallest DM dominated dwarf galaxies [58]. The upper bound arises from the observed stability of large binary stellar systems, which requires  $m_{\text{DM}} < 100 M_\odot$  [59], so the viable mass window is dauntingly difficult to test without the existence of additional interactions between DM and the SM particles.

There is a popular class of models that call for additional DM-SM interactions. In this paradigm, DM survives as a relic from an era of thermodynamic equilibrium with the SM in the early universe, and its abundance was set when its interaction rate with the SM became subdominant to the expansion rate of the universe — a mechanism

---

<sup>§§</sup> The accelerated expansion of the universe (“Dark Energy”) can be interpreted as evidence of physics beyond the SM [56], but this phenomenon can be accommodated with a small cosmological constant within minimal General Relativity, so no new physics is strictly required. Similarly, dynamically generating the observed baryon asymmetry of the universe [57] requires physics beyond the SM, however, in principle, this could be accommodated with fine-tuned initial conditions; a similar argument applies to the appeal for new physics motivated by cosmic inflation.

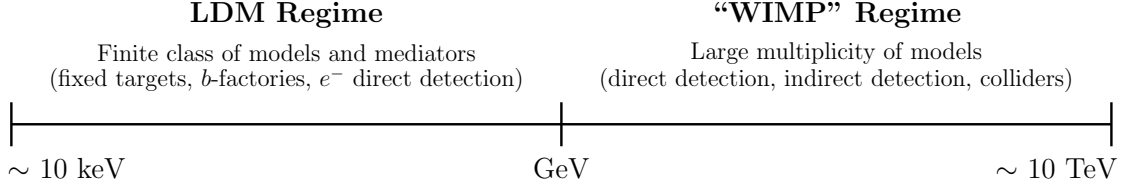


Figure 36: The viable mass window for DM with a thermal cosmological history. The upper half of this parameter space covers traditional WIMP models in which DM carries SM charges under the weak force and is tested using direct detection (if it scatters elastically off nuclear targets), indirect detection (if its abundance is particle-antiparticle symmetric), and collider production. The lighter half of this window, the aim of the BDX collaboration, is comparatively less well studied, and can primarily be tested using intensity frontier methods including fixed target accelerator techniques. Below  $\sim 10$  keV, DM is too hot to accommodate viable large scale structure formation; above  $\sim 10$  TeV, the DM annihilation rate compatible with a thermal origin violates perturbative unitarity and nontrivial model building is required.

commonly known as “freeze-out”. A thermal origin imposes a requirement on the DM: its mass is restricted to be  $m_{\text{DM}} > 10$  keV. Otherwise it remains relativistic until late times and thereby erases the observed structure on small scales [60].

In this paradigm of a thermal origin for DM, DM would have been in equilibrium with the SM in the early universe through DM annihilation into two or more SM final states. On general grounds, the annihilation cross section times velocity for such a process scales roughly as  $\sigma v \sim g_{\text{DM}}^4/m_{\text{DM}}^2$ , where  $g_{\text{DM}}$  is some DM coupling constant. To achieve the observed DM abundance,  $\Omega_{\text{DM}} = 0.243 \pm 0.004 \propto 1/\langle\sigma v\rangle$  [10], the thermally averaged annihilation cross section must be of order  $\langle\sigma v\rangle \sim 3 \times 10^{-26} \text{ cm}^3 \text{ s}^{-1}$  [61]. For DM masses near  $m_{\text{DM}} \gtrsim 10$  TeV, an annihilation rate of this magnitude requires  $g_{\text{DM}} \gtrsim 4\pi$ , corresponding to cross sections that violate perturbative unitarity in minimal models [59].<sup>¶¶</sup> Thus, the simple, physically motivated criterion of thermal equilibrium between dark and visible matter requires:

- A minimum annihilation cross section  $\langle\sigma v\rangle \geq 3 \times 10^{-26} \text{ cm}^3 \text{ s}^{-1} \equiv \langle\sigma v\rangle_{\text{relic}}$ , where the equality corresponds to particle-antiparticle symmetric DM for which the annihilation is responsible for the full relic abundance and the inequality corresponds to asymmetric DM, for which annihilation merely eliminates thermal antiparticles. The asymmetric DM scenario that we refer to throughout this proposal refers to the case where there is an asymmetry between particles and

<sup>¶¶</sup>It is possible to circumvent such a hard requirement with composite or strongly interacting dark sectors, but many additional degrees of freedom are required for a complete model [62].

anti-particles in the DM sector, in analogy to the baryon and lepton asymmetries in the SM.

- The DM mass must fall in the viable window between  $\sim 10 \text{ keV} - 10 \text{ TeV}$ , which dramatically focusses the scope of the experimental discovery effort regardless of other model-specific details.

The above considerations apply to *any* DM scenario that reaches thermal equilibrium with visible matter in the early universe. Figure 36 shows a schematic diagram representing the viable mass range for thermal DM.

On the heavier half of this allowed mass range,  $m_{\text{DM}} \in [\text{few GeV}, 10 \text{ TeV}]$ , the particle physics model landscape for DM and its interactions is often connected to the electroweak scale. For instance, heavy thermal DM can arise as the lightest neutral superpartner in supersymmetric extensions of the SM, motivated to address the electroweak hierarchy problem (e.g. the MSSM or similar model variants) [63]. Other solutions to the electroweak hierarchy problem including composite Higgs models [64, 65, 66, 67], twin Higgs models [68], flat [69] and warped [70] extra dimensions, also include weak scale DM candidates. In many such scenarios, the DM candidate is a Weakly Interacting Massive Particle (WIMP) which freezes-out via SM gauge interactions; this  $\langle \sigma v \rangle_{\text{WIMP}} \sim \langle \sigma v \rangle_{\text{relic}}$  coincidence is the so-called “WIMP miracle,” for which no additional interactions are required to yield the observed DM abundance.

DM-SM interactions in this class of WIMP models can be tested with a rich variety of experimental techniques including direct detection, indirect detection, and collider production searches. If the leading DM-SM non relativistic scattering process is elastic and spin independent, existing direct detection experiments like LUX [71], XENON-100[72], and CDMS [73] and future experiments including XENON-1T [74], LZ [75], and Darwin[76] can probe much of the remaining parameter space compatible with WIMP DM. If the DM abundance is particle/antiparticle symmetric with a thermal cosmological history, DM annihilation in high density astrophysical regions (e.g. the galactic center) can be observed using ground and space based instruments, such as the *Fermi*-LAT [77]. Heavy DM can also be tested at the LHC in events with missing (transverse) energy in association with visible SM states [17, 78].

However, for Light Dark Matter (LDM) on the lower half of the viable thermal window,  $m_{\text{DM}} \in [10 \text{ keV}, \text{GeV}]$ , these well known experimental strategies become highly ineffective. Typical direct detection sensitivity thresholds require the incoming, elastically scattering DM candidate to deposit  $E \gtrsim \text{keV}$  scale energies onto a nuclear target. However, the recoil energy of a 2-body scatter scales as  $E_{\text{rec.}} \sim \mu v^2$ , where  $\mu = m_N m_{\text{DM}} / (m_N + m_{\text{DM}})$  is the nucleus-DM reduced mass and  $v \sim 10^{-3}c$  is their relative velocity in the terrestrial lab frame. Thus, for  $m_{\text{DM}} \lesssim \text{GeV}$ , this energy deposition is below typical sensitivity thresholds at direct detection experiments. For indirect detection, the energies of daughter particles resulting from DM annihilation are in the

sub-GeV range where complicated astrophysical backgrounds are poorly understood and difficult to distinguish from a potential DM signal. At collider experiments, LDM can appear as missing energy in association with other visible objects; however, unlike heavier DM, LDM does not significantly recoil against the visible object(s) and is, therefore, difficult to distinguish from SM backgrounds (e.g.  $Z + \text{jets}$  or mis-measured missing energy in multijet events).

## A.1 Generic features of the theory of Light Dark Matter

We now focus our attention on the parameter space of LDM, in particular on the simple models that accommodate thermal-relic LDM. If LDM were merely a WIMP with a smaller mass, its annihilation rate via  $\text{DM DM} \rightarrow Z^* \rightarrow \text{SM SM}$  would scale as

$$\langle\sigma v\rangle_{\text{LDM,WIMP}} \sim G_F^2 m_{\text{DM}}^2 = 1.3 \times 10^{-29} \text{cm}^3 \text{s}^{-1} \left( \frac{m_{\text{DM}}}{100 \text{MeV}} \right)^2 \ll \langle\sigma v\rangle_{\text{relic}} , \quad (21)$$

which is insufficient to accommodate efficient annihilation in the early universe and similar arguments apply to other annihilation processes (e.g. virtual Higgs boson exchange). As a consequence, while one can still have the DM achieve thermal equilibrium, one will overproduce DM, so LDM WIMPs without additional interactions are not viable. Thus, thermal LDM is conceptually distinct from heavy WIMP DM in two key respects:

- LDM requires additional forces with correspondingly light, sub-GeV force carriers to achieve the observed DM abundance.
- Both the DM and the new force carriers (“mediators”) must be neutral under the SM gauge group, otherwise they would have been discovered in direct searches at previous experiments (*e.g.*, LEP).

Given that there is no room for new SM charged matter at the GeV scale, the gauge and Lorentz symmetries of the SM greatly restrict the ways in which the mediator can couple to the SM. One expects the dominant interactions to be the so-called renormalizable portals: those interactions consisting of SM gauge singlet operators with mass dimension  $< 4$ :

$$\hat{\mathcal{O}}_{\text{portal}} = H^\dagger H \quad , \quad LH \quad , \quad B_{\mu\nu} \quad , \quad (22)$$

and a new SM-neutral degree of freedom, which can be a scalar  $\phi$ , a fermion  $N$ , or a vector  $A'$ . Here  $H$  is the SM Higgs doublet with charge assignment  $(1, 2, +\frac{1}{2})$  under the SM gauge group  $SU(3)_c \times SU(2)_L \times U(1)_Y$ ,  $L$  is a lepton doublet of any generation

transforming as  $(1, 2, -\frac{1}{2})$ , and  $B_{\mu\nu} \equiv \partial_\mu B_\nu - \partial_\nu B_\mu$  is the hypercharge field strength tensor. Although there could also be higher dimension effective operators to connect to the mediators, direct searches for the states that resolve such operators require suppression scales in excess of the electroweak scale, which generically would reintroduce the DM overproduction problem if these were the predominant interactions that set the DM relic abundance.

If the mediator is a scalar particle  $\phi$ , the only allowed renormalizable interactions are through the Higgs portal via  $\phi H^\dagger H$  and  $\phi^2 H^\dagger H$  which induce mass mixing between  $\phi$  and the SM Higgs boson after electroweak symmetry breaking – we consider this possibility in more detail in Sec. A.3.

If the mediator is a fermion  $N$ , its interaction with the SM proceeds through the neutrino portal  $\sim y_\nu L H N$  and it plays the role of a right handed neutrino with a Yukawa coupling  $y_\nu$ . If DM is *not* thermal in origin,  $N$  can itself be a viable, cosmologically metastable DM candidate in a narrow mass range [79]. Since  $N$  is stipulated to be sub-GeV, obtaining the observed neutrino masses (without additional field content) requires Yukawa couplings of order  $y_\nu \lesssim 10^{-12}$ , which are too small to allow thermalization to take place at early times [80].

If the mediator is a vector force carrier from an additional  $U(1)_D$  gauge group under which LDM is charged, the “kinetic mixing” interaction  $\epsilon_Y B^{\mu\nu} F'_{\mu\nu}$  is gauge invariant under both  $U(1)_D$  and  $U(1)_Y$ . Here  $\epsilon_Y$  is, *a priori* a free parameter, though it often arises in UV complete models after heavy states charged under both groups are integrated out at a high scale, so it is generically expected to be small ( $\epsilon_Y \sim 10^{-3} - 10^{-5}$  depending on the loop order at which it is generated). Such a radiative origin for  $\epsilon_Y$  is required if either  $U(1)$  group is a subset of a nonabelian group for which kinetic mixing is not a gauge invariant interaction; it can only be generated after a spontaneous symmetry breaking phase transition which preserves an unbroken  $U(1)$  subgroup.

## A.2 Defining thermal targets

For all mediators and LDM candidates  $\chi$ , there is a basic distinction between “secluded” annihilation to pairs of mediators (via  $\chi\chi \rightarrow \text{MED MED}$  for  $m_\chi > m_{\text{MED}}$ ) followed by mediator decays to SM particles [81], and “direct” annihilation to SM final states (via virtual mediator exchange in the  $s$ -channel,  $\chi\chi \rightarrow \text{MED}^* \rightarrow \text{SM SM}$  for  $m_\chi < m_{\text{MED}}$ ) without an intermediate step.

For the secluded process, the annihilation rate scales as

$$(\text{“secluded” annihilation}) \quad \langle \sigma v \rangle \sim \frac{g_D^4}{m_\chi^4}, \quad (23)$$

where  $g_{\text{DM}}$  is the coupling between the mediator and the LDM, and there is no



dependence on the SM-mediator coupling  $g_{\text{SM}}$ . Since arbitrarily small values of  $g_{\text{SM}}$ , the SM-mediator coupling, can be compatible with thermal LDM in this regime, the secluded scenario does not lend itself to decisive laboratory tests;

The situation is markedly different for the direct annihilation regime in which  $m_\chi < m_{\text{MED}}$ , where the annihilation rate scales as

$$(\text{“direct” annihilation}) \quad \langle \sigma v \rangle \sim \frac{g_D^2 g_{\text{SM}}^2 m_\chi^2}{m_{\text{MED}}^4} , \quad (24)$$

and offers a clear, predictive target for discovery or falsifiability since the dark coupling  $g_D$  and mass ratio  $m_\chi/m_{\text{MED}}$  are at most  $\mathcal{O}(1)$  in this  $m_{\text{MED}} > m_\chi$  regime, so there is a minimum SM-mediator coupling compatible with a thermal history; smaller values of  $g_D$  require nonperturbative dynamics in the mediator-SM coupling or intricate model building.

In the direct annihilation regime, up to order-one factors, the minimum annihilation rate requirement translates into a minimum value of the dimensionless combination

$$y \equiv \frac{g_D^2 g_{\text{SM}}^2}{4\pi} \left( \frac{m_\chi}{m_{\text{MED}}} \right)^4 \gtrsim \langle \sigma v \rangle_{\text{relic}} m_\chi^2 , \quad (25)$$

which, up to order one factors, is valid for every DM/mediator variation provided that  $m_{\text{DM}} < m_{\text{MED}}$ . We will use this target throughout this document to assess experimental sensitivity to various LDM scenarios; reaching this benchmark sensitivity suffices to decisively discover or falsify a large class of simple direct annihilation models.

### A.3 Excluding scalar mediated direct annihilation

From the above listed class of portal mediators, the scalar Higgs portal scenario with a scalar mediator is compelling in its simplicity: a real singlet scalar  $\phi$  couples to the SM by mixing with the SM Higgs boson and interacts with fermions in direct proportion to their masses. Assuming a fermionic DM particle for concreteness, the lagrangian for this theory is

$$\mathcal{L} \supset g_D \phi \bar{\chi} \chi + \frac{m_\phi^2}{2} \phi^2 + A H^\dagger H \phi + \frac{m_f}{v} H \bar{f}_L f_R + h.c. , \quad (26)$$

where  $f$  is a SM fermion with mass  $m_f$ ,  $A$  is a dimensional coupling constant, and  $v$  is the SM Higgs vacuum expectation value (VEV). After electroweak symmetry breaking, the replacement  $H \rightarrow v$  induces a mass mixing term between  $\phi$  and the

neutral component of the Higgs doublet. Diagonalizing this mixing yields a coupling between  $\phi$  and SM fermions  $g_{\text{SM}} \equiv \sin \theta m_f / v$ , where  $\sin \theta$  is the higgs- $\phi$  mixing angle.

In the  $m_\chi < m_\phi$ , the relic density is achieved via  $\chi\chi \rightarrow \phi^* \rightarrow ff$  direct annihilation and the thermal target for a given final state  $f$  is

$$y \equiv g_D^2 \sin^2 \theta \left( \frac{m_f}{v} \right)^2 \left( \frac{m_\chi}{m_\phi} \right)^4 > \langle \sigma v \rangle_{\text{relic}} m_\chi^2, \quad (27)$$

Since LDM requires annihilation to light SM fermions with  $m_f \ll v$ , the mixing angle must satisfy  $\sin \theta \sim \mathcal{O}(1)$  over most of the  $m_\chi < \text{GeV}$  range [82]. However, such a large value predicts unacceptably large branching ratios for  $B \rightarrow K\phi$  which contributes irreducibly to  $B^+ \rightarrow K^+ \nu \bar{\nu}$  and  $K^+ \rightarrow \pi^+ \nu \bar{\nu}$  observables. This process, which is generated by loops of virtual tops whose coupling to  $\phi$ , is enhanced by scales as  $m_t/m_f$  relative to the corresponding coupling for  $\chi\chi \rightarrow ff$  annihilation. Thus, scalar mediated annihilation through the Higgs portal is completely ruled out; “secluded” annihilation for  $m_\chi > m_\phi$  via  $\chi\chi \rightarrow \phi\phi$  is still viable, but offers no thermal target [82].

## A.4 Vector mediated models

While scalar direct annihilation is ruled out and the neutrino portal is not easily compatible with thermal LDM, the vector portal, where a new vector  $A'$  couples to the SM hypercharge, is largely unexplored for the parameter space of LDM. Therefore, we take this scenario as a basis for determining the sensitivity of the experiment. Consider a spin-1 mediator  $A'$ , which kinetically mixes with the SM hypercharge via  $\epsilon_Y B^{\mu\nu} F'_{\mu\nu}$ . Here,  $A'$  can be thought of as the gauge boson from a spontaneously broken  $U(1)_D$  gauge group, and DM is charged under this gauge group<sup>\*\*\*</sup>. The 1 for this setup is [2]

$$\mathcal{L}_{A'} \supset -\frac{1}{4} F'_{\mu\nu} F'^{\mu\nu} + \frac{\epsilon_Y}{2} F'_{\mu\nu} B_{\mu\nu} + \frac{m_{A'}^2}{2} A'_\mu A'^\mu + g_D A'_\mu J_\chi^\mu + g_Y B_\mu J_Y^\mu, \quad (28)$$

where  $F'_{\mu\nu} \equiv \partial_\mu A'_\nu - \partial_\nu A'_\mu$  is the dark photon field strength,  $B_{\mu\nu} \equiv \partial_\mu B_\nu - \partial_\nu B_\mu$  is the hypercharge field strength,  $g_D \equiv \sqrt{4\pi\alpha_D}$  is the dark gauge coupling, and  $J_\chi^\mu$  and  $J_Y^\mu$  are the DM and SM hypercharge matter currents, respectively. After

---

<sup>\*\*\*</sup> Reinterpreting the results from the kinetic mixing model into other scenarios – for instance gauging both  $\chi$  and the SM under one of the anomaly free combinations of SM global quantum numbers:  $U(1)_{B-L}$ ,  $U(1)_{e-\mu}$ ,  $U(1)_{e-\mu}$ ,  $U(1)_{e-\tau}$ ,  $U(1)_{\mu-\tau}$  – is trivially accomplished by appropriately rescaling coupling constants by the kinetic mixing parameter  $\epsilon$ . The key phenomenological difference in these models is that the mediator couples appreciably to neutrinos with equal strength, whereas the dark photon couples predominantly to the electromagnetic current

electroweak symmetry breaking, the hypercharge kinetic mixing  $\epsilon_Y$  induces mixing with the photon and  $Z$  boson

$$\frac{\epsilon_Y}{2} F'_{\mu\nu} B_{\mu\nu} \longrightarrow \frac{\epsilon}{2} F'_{\mu\nu} F_{\mu\nu} + \frac{\epsilon_Z}{2} F'_{\mu\nu} Z_{\mu\nu} , \quad (29)$$

where  $\epsilon \equiv \epsilon_Y / \cos \theta_W$ ,  $\epsilon_Z \equiv \epsilon_Y / \sin \theta_W$ , and  $\theta_W$  is the weak mixing angle. Diagonalizing away this mixing yields dark photon interactions with dark and visible matter

$$g_D A'_\mu J_\chi^\mu + g_Y B_\mu J_Y^\mu \longrightarrow A'_\mu (g_D J_\chi^\mu + \epsilon e J_{\text{EM}}^\mu) , \quad (30)$$

where  $J_{\text{EM}}^\mu$  is the usual SM electromagnetic current and we have omitted terms higher order in  $\epsilon$ . The dark photon  $A'$  couples to the LDM current  $J_\chi^\mu$ , which can represent either a scalar or fermionic DM candidate. For the remainder of this document we will assume the predictive, direct annihilation regime  $m_{A'} > 2m_\chi$  (see right column of Fig. 1).

Regardless of the LDM candidate whose current is given by  $J_\chi$ , the thermal target from Eq. (27), corresponding to the direct annihilation in Fig. X (c), can be written as

(vector mediator target)  $y \equiv \epsilon^2 \alpha_D \left( \frac{m_\chi}{m_{A'}} \right)^4 ,$

(31)

where the precise value of this target depends on the choice of LDM candidate. This class of models is compatible with a finite set of LDM candidates which can be either fermions or scalars, cosmologically particle-antiparticle symmetric or asymmetric, and may couple elastically or inelastically to the  $A'$ . We now consider these permutations in turn.

## A.5 LDM candidates with vector mediator

### Symmetric Fermion LDM

If the LDM candidate is a fermion, the current in Eq. (28) is

$$(\text{fermion LDM current}) \quad J_\chi^\mu \equiv \bar{\chi} \gamma^\mu \chi , \quad (32)$$

where  $\chi$  is a four component Dirac fermion with mass  $m_\chi$ . The abundance in this scenario is symmetric with respect to particles and antiparticles, so the annihilation rate must satisfy  $\langle \sigma v \rangle \approx 3 \times 10^{-26} \text{cm}^2 \text{s}^{-1}$  to achieve the observed relic abundance.

However, for Dirac fermions, the annihilation cross section is  $s$ -wave

$$\langle\sigma v\rangle\propto\epsilon^2\alpha_D\frac{m_\chi^2}{m_{A'}^4}\sim\frac{y}{m_\chi^2},\quad(33)$$

and therefore constant throughout cosmic evolution, including during the epoch of the CMB near  $T\sim\text{eV}$ . Although the abundance has frozen out by this point, out-of-equilibrium annihilations to SM particles can re-ionize hydrogen at the surface of last scattering and leave an imprint in the SM ionized fraction [5]. For a particle-antiparticle symmetric population of  $\chi$ , this scenario is comprehensively ruled out by measurements of the CMB power spectrum so we will not consider it further [6].

### Asymmetric Fermion LDM

If the cosmic abundance of Dirac fermion  $\chi$  is set by a primordial asymmetry, then

the annihilation process depletes antiparticles during the CMB epoch so the effective abundance of antiparticles is suppressed by factors of  $\sim\exp(-\langle\sigma v\rangle)$ . Thus, the CMB re-ionization bound does not rule out this scenario.

### Majorana (Pseudo-Dirac) LDM

The dark photon has a non-zero mass  $m_{A'}$ , which means that the  $U(1)_D$  in the dark

sector is a broken gauge theory — unlike the SM electromagnetism, which is unbroken, as evidenced by the photon being massless. A generic possibility in this broken gauge theory is that the fermion LDM candidate has both a  $U(1)_D$  preserving Dirac mass and  $U(1)_D$  breaking Majorana mass — possibly induced by the mechanism responsible for spontaneous symmetry breaking in the dark sector. This same mechanism could be responsible for giving the dark photon a mass  $m_{A'}$ . As a result, the Weyl spinors in the four component  $\chi$  will be split in mass and the dark photon couples predominantly to the *off-diagonal* current

$$(\text{off} - \text{diagonal fermion LDM current})\quad J_\chi^\mu\equiv\bar{\chi}_1\gamma^\mu\chi_2+h.c.\,,\quad(34)$$

where  $\chi_{1,2}$  are Majorana spinors split in mass by  $m_2-m_1\equiv\Delta$ ; all interactions with the  $A'$  are off-diagonal in this mass eigenbasis. Note that, like the Dirac scenario, this variant has the same degrees of freedom (2 Weyl spinors) but different global symmetries in the fermion mass sector, so this kind of coupling arises generically if those symmetries are broken. Note that  $\chi_2$  is unstable and decays via  $\chi_2\rightarrow\chi_1 f\bar{f}$  for  $m_{A'}>m_1+m_2$ , which is required for the direct annihilation scenario.

Unlike the Dirac case, the direct annihilation for the pseudo-Dirac scenario requires *both* eigenstates to meet via  $\chi_1\chi_2\rightarrow A'\rightarrow ff$ , so at late times  $T\ll\Delta$  this process shuts off. For small  $\Delta\ll m_\chi$  this annihilation rate has the same parametric

scaling as the Dirac fermion scenario

$$\langle\sigma v\rangle\propto\epsilon^2\alpha_D\frac{m_\chi^2}{m_{A'}^4}\sim\frac{y}{m_\chi^2}+\mathcal{O}\left(\frac{\Delta}{m_\chi}\right)\,,\quad(35)$$

so the same  $y$  target applies. However, the CMB bound is now removed because the excited state  $\chi_2$  is typically absent at late times, thus shutting off the tree-level annihilation  $\chi_1\chi_2\rightarrow A'\rightarrow ff$ . It's worth noting that the setup of Majorana LDM with a dark photon that mixes with hypercharge falls within the popular class of models known as “inelastic DM” [83].

### Scalar LDM

If the LDM candidate is a complex scalar coupled to the dark photon, the current in Eq. (30) is

$$(\text{scalar LDM current})\quad J_\chi^\mu\equiv i(\chi^*\partial^\mu\chi-\chi\partial^\mu\chi^*)\,,\quad(36)$$

where momentum dependence in the coupling to the  $A'$  leads to a  $p$  wave annihilation rate  $\chi\chi\rightarrow A'\rightarrow ff$

$$\langle\sigma v\rangle\propto\epsilon^2\alpha_D\frac{m_\chi^2v^2}{m_{A'}^4}\sim\frac{yv^2}{m_\chi^2}\,,\quad(37)$$

where  $v$  is the velocity. Note that compared to the fermion scenario, for fixed  $m_\chi$ , the thermal target for  $y$  is  $\mathcal{O}(10)$  larger to compensate for the  $v^2\sim 0.1$  rate reduction due to the DM velocity at freeze out,  $T\sim m_\chi/20$ , when the relic abundance is set.

In summary, by far, a new spin-1 light degree of freedom, a  $A'$  that kinetically-mixes with the SM hypercharge, gives the most viable scenario for models of LDM with a thermal origin. This is the scenario targetted in the proposal and serves as a basis for defining the sensitivity for the experiment.

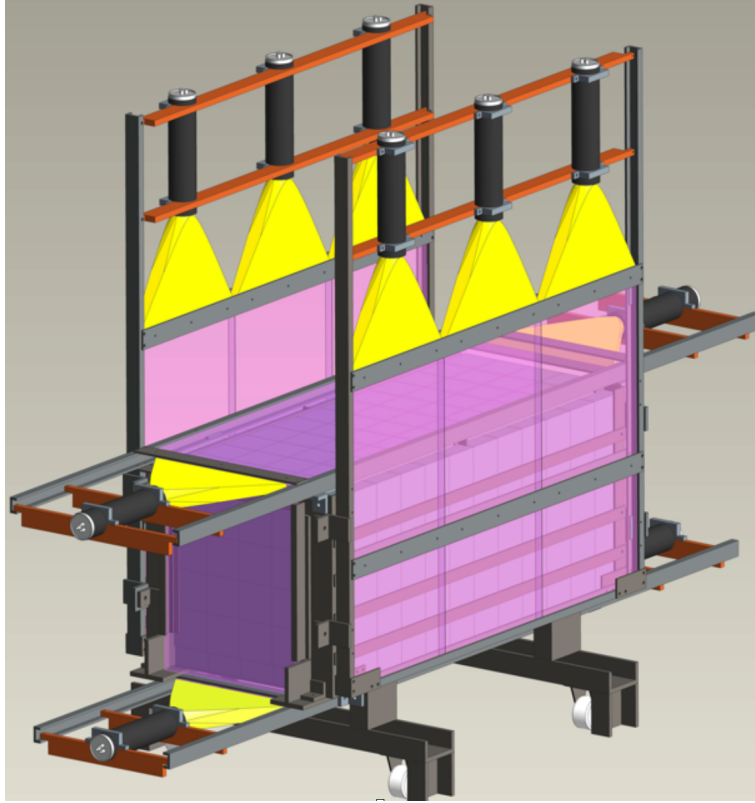


Figure 37: The CAD drawing of the BDX prototype detector: the Outer Veto (OV) with light guides and PMTs are visible together with the lead vault (in transparence).

## B The BDX prototype

In this Appendix we report the results of a dedicated campaign of measurements performed in Catania, Italy (INFN-CT) and Laboratori Nazionali del Sud (LNS) with a prototype of the BDX detector. The measurement provided information useful for the full detector design and expected performance in a realistic configuration. We tested the proposed technology for the BDX detector: CsI(Tl) crystals read by SIPM, plastic scintillator read by PMT for the OV and plastic scintillator coupled to SIPM by WLS fibers; we validated the background model for cosmic muons and neutrons; we checked the effect of the lead shielding and the overburden, and, eventually, we derived the single crystal rates as a function of the energy threshold in combination (anti-coincidence) with the veto system. In Sec. 4.4 these measurements have been extrapolated to the full experiment (scaling to the detector size and the measurement time) providing a reliable estimate of the expected cosmogenic background. To validate Monte Carlo simulations in a standard and well-controlled configuration, cosmic

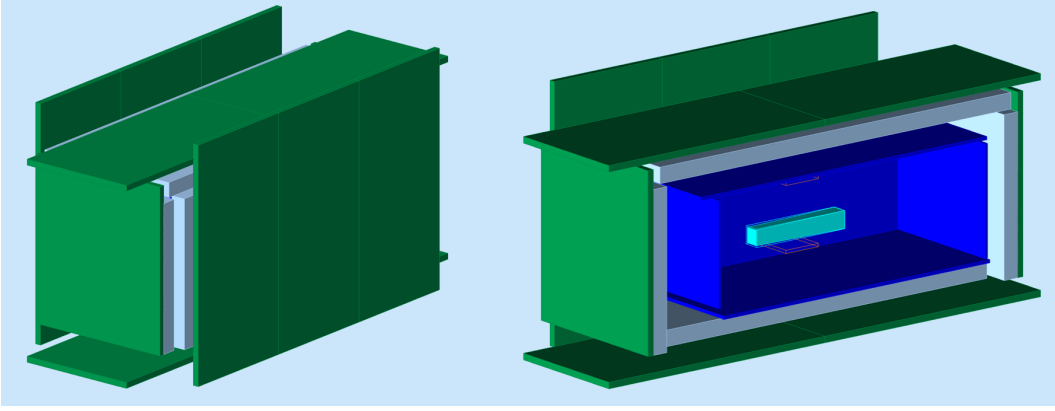


Figure 38: The implementation of the BDX prototype in GEMC. The OV (green), the lead vault (gray), IV (blue), and the crystal (cyan) are visible in the drawing on the right panel.

data were initially taken exposing the prototype to cosmic rays with minimal shielding (15 cm of concrete roof of INFN-CT). Then the prototype was moved into a bunker at LNS with a surrounding overburden of about 5 meters of concrete corresponding to an effective thickness of  $1080 \text{ g/cm}^2$  similar to  $1165 \text{ g/cm}^2$  expected at JLab.

In order to prove the detection capability of the BaBar crystals for low energy protons with the new improved readout sensor and electronics, we studied the response of the CsI(Tl) crystal to a low energy proton beam ( $T_p$  from 2 MeV to 24 MeV) provided by the LNS-Tandem Van der Graaf. The results of these measurements are reported in the last paragraph.

## B.1 The BDX prototype

The BDX prototype is made by a single BaBar CsI(Tl) crystal surrounded on all sides by a layer of veto detectors (Inner Veto or IV), a vault of lead bricks, and a second layer of veto detectors forming the Outer Veto (OV, Fig. 37). The combined use of two charged-particle veto-counter systems allows to compensate for their inefficiencies and better reject background. Between the inner and the outer veto, the 5cm thick lead vault shields the crystal from radiogenic low energy gammas. Two additional small-area plastic scintillator pads ( $12 \times 12 \times 1 \text{ cm}^3$ ) were placed inside the inner veto, one above and one below the CsI(Tl), to trigger on cosmic rays for energy calibration, timing and efficiency measurements. The full GEANT4 implementation of the BDX prototype is shown in Fig. 38 while a picture of the experimental set-up mounted at INFN-CT and LNS is shown in Fig. 39.

The CsI(Tl) crystal is one of those formerly used in the BaBar Ecal end cap with



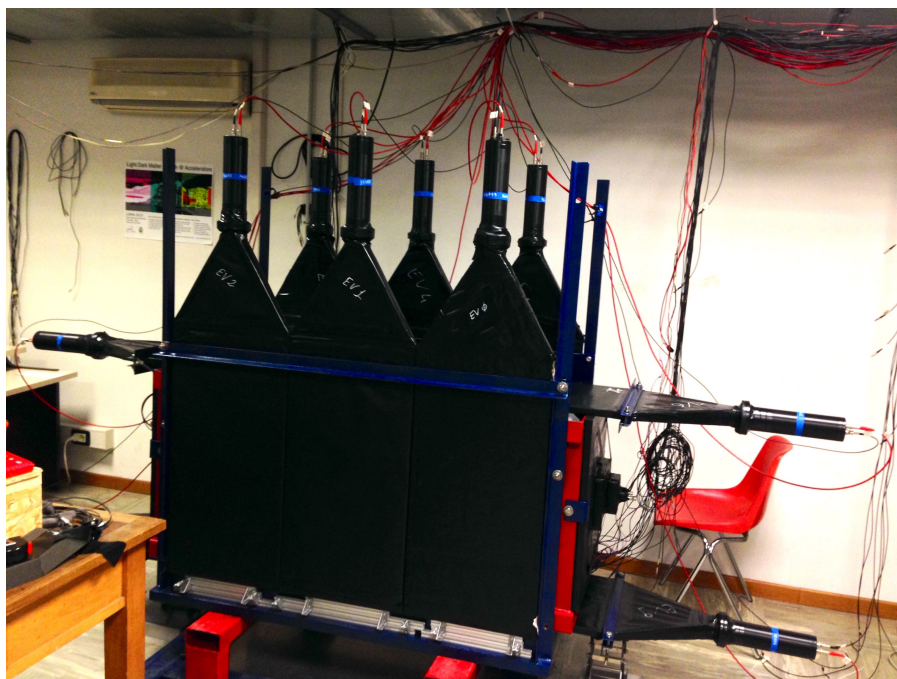


Figure 39: The prototype mounted and cabled at the INFN- Sezione di Catania (top) and inside the LNS bunker (bottom).



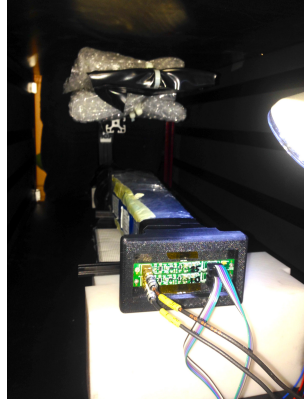


Figure 40: A picture of the CsI(Tl) crystal inside the prototype. The two charge-preamplifiers coupled to the SiPM are visible together with the two additional small plastic scintillators.

a brand new SiPM-based readout. It is 31cm long and has a trapezoidal shape with a  $4.7 \times 4.7 \text{ cm}^2$  front face and a  $6 \times 6 \text{ cm}^2$  back face (Fig. 40). Two  $3 \times 3 \text{ mm}^2$  SiPMs (Hamamatsu S13360-3025CS and S13360-1350CS), with pixel size of 25 and  $50 \mu\text{m}$ , are glued to the crystal front-face (leaving untouched the existing pin diode used by BaBar on the opposite side). The  $50 \mu\text{m}$  cell-size has an higher PDE (35%), more suitable for low energy signals while the  $25 \mu\text{m}$ , having a larger number of pixels has a lower PDE (22%) but results in a fairly linear response for higher energy signals. Both sensors are coupled to custom trans-impedance amplifiers [84] with different gains:  $G_{50\mu\text{m}}=230$  and  $G_{25\mu\text{m}}=40$ . The lower gain  $G_{25\mu\text{m}}$  results in an extended dynamic range allowing the measurement of the high-energy part of the spectrum, up to about 500 MeV. Bias voltage for the two SiPMs was provided by a custom designed board, with an on-board tunable DC-DC converter, working with 5V input voltage.

The Inner Veto (IV) is made by plastic scintillators, 1cm thick, forming a nearly hermetic parallelepiped (Fig. 41). Two  $35 \times 42 \text{ cm}^2$  EJ200 scintillators are used for the downstream and upstream caps. On each of them a spiral groove hosts a WLS fiber used to collect and transfer the light to a SiPM (Fig. 41 bottom-left). Three  $35 \times 140 \text{ cm}^2$  EJ200 scintillators form the top, left and right sides of the veto. In this case, the WLS fibers are inserted into four linear grooves running parallel to the long side of the plastic (Fig. 41 bottom-right). This solution results in an high detection efficiency ( $> 99.5\%$ ), almost independent on the hit point, but still providing some information also on the hit position, by correlating the quantity of light detected by each of the four independent SiPMs. Finally, in order to test another possible technology for the IV, the bottom side was made by four bars of extruded plastic scintillators,  $8 \times 140$

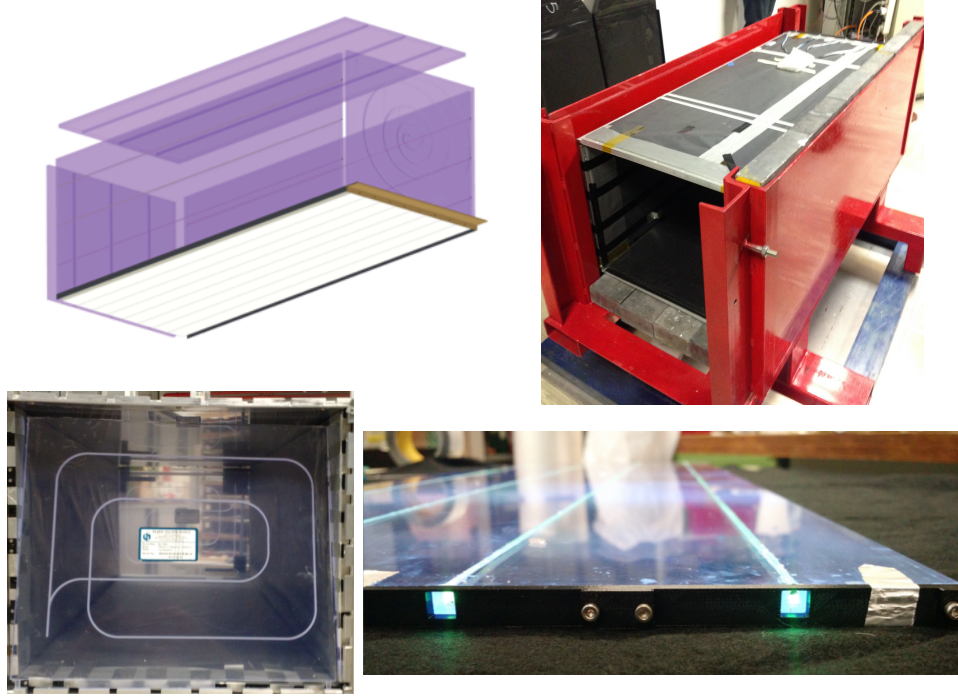


Figure 41: A sketch of the Inner Veto (top-left), the detector mounted inside the mechanical structure of the prototype (top-right), and two pictures of the upstream (bottom-left) and top (bottom-right) paddles.

$\text{cm}^2$ , individually readout by a SiPM coupled to WLS fibers inserted in the middle of each bar.

The Outer Veto is made by 2cm thick NE110 plastic scintillators. The top (bottom) side is made by two  $80 \times 40 \text{ cm}^2$  paddles as shown in Fig. 42. Three scintillators of the same area are vertically arranged to cover each of the two lateral sides. A “fish tail” shaped PMMA light guide, glued on one side of the scintillator, directs the light to a 2” photomultiplier tube (Thorn EMI 9954A) optically matched with the light guide trough optical grease. A smaller paddle ( $56 \times 50 \text{ cm}^2$ ) forms the upstream (downstream) cap. In this case, light is readout by a 1” Photomultiplier tube (R1924A Hamamatsu) placed in the middle of the plastic surface and directly coupled to it through optical grease. A detection efficiency  $> 99.5\%$  was measured for each OV paddle for cosmic rays selected by triggering on the coincidence of two small paddles placed above and below the scintillator, uniform over the whole scintillator surface.

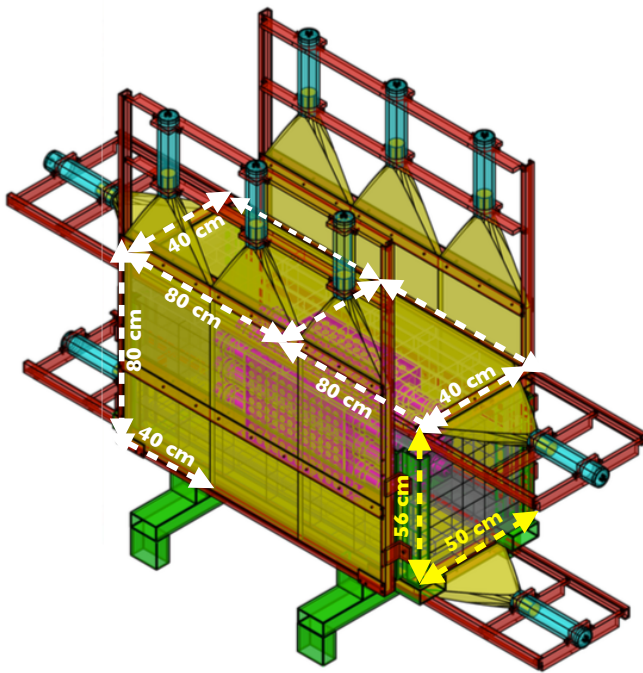


Figure 42: A CAD image of the prototype (left). The OV detectors and light guides are in yellow, the PMT in blue and their mechanical supports in red. On the right, an OV detector is shown inside the mechanical support used to glue the light-guide to the scintillator.

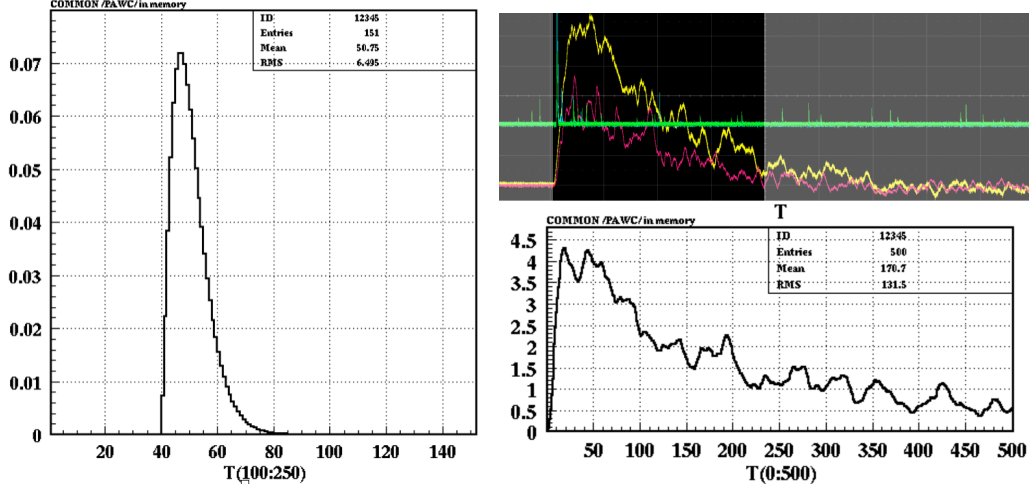


Figure 43: Left: Response of the preamplifier to a single p.e. (time is shown in 4 ns samples). Right: comparison of the response to a crossing muon (top) and the result of the simulation (bottom). The simulation is limited to the highlighted  $2\mu s$  window (time is shown in 4 ns samples).

Data acquisition is based on VME-VXS JLab fa250 digitizers with 12 bit resolution, 250 MHz sampling rate and  $2\mu s$  readout window. The main trigger is generated by a signal over threshold in the CsI(Tl) crystal, namely from the logic OR of the two SIPMs. The output signals are split by a 50 Ohm-50 Ohm divider: one copy is sent to the FADC and the other one to a Leading-Edge Discriminator with thresholds set to 15mV and 50mV for the 25 and 50  $\mu m$ , respectively. These thresholds correspond to about 5 p.e. for both SIPMs and, as derived from the proton beam measurements (see Sec. B.6), they correspond to an energy threshold for protons of about 2 MeV. Three other secondary triggers, conveniently pre-scaled, were also included for monitoring, calibration and efficiency studies: logic AND of the two small paddles, logic AND of two or more IV signals, logic AND of two or more OV detectors.

## B.2 Simulation of the BDX prototype

The realistic geometry as well as the material composition of the BDX prototype have been implemented in GEMC (GEANT4) simulations. The response of individual components of the prototype (crystal, IV paddles and SIPM, OV paddles and lightguides plus PMTs) have been measured by means of cosmic muons, parametrized, and included in simulations. The resulting good agreement between data and MC for both cosmic muons and low energy protons will be shown in the next Sections.

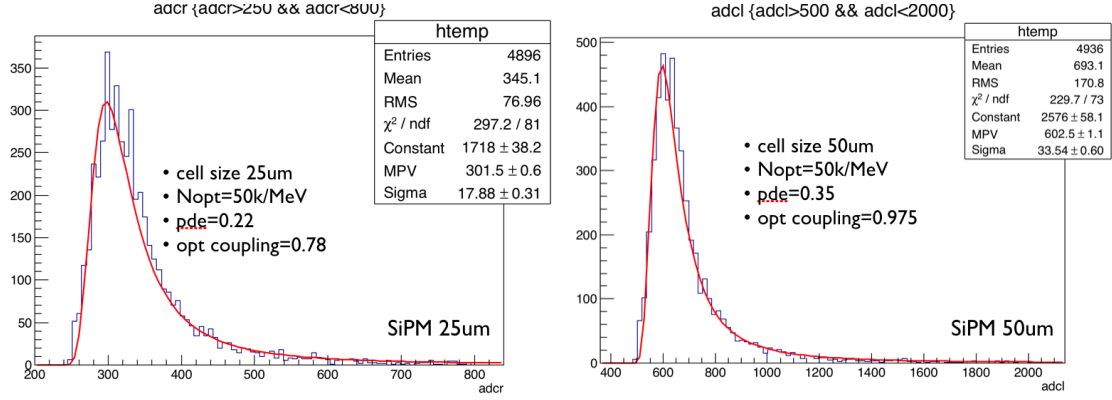


Figure 44: Simulated response of the crystal to crossing muons. Left and right panels correspond to the 25 and 50 $\mu\text{m}$  cell size respectively.

### B.2.1 The crystal response

The CsI(Tl) crystal is coupled to two 3x3 mm<sup>2</sup> SiPMs sensitive to a single p.e. The signal is then amplified by a trans-impedance preamplifier whose response to a single p.e. has been measured and parametrized as reported in the left plot of Fig. 43. Due to the sizable scintillation time of CsI(Tl), the response to  $N_{p.e.}$  can be described as a convolution of the single p.e. response with the time distribution of the scintillation signal. A comparison of the measured signal for a cosmic muon and the results of the simulation is reported in the right plot of Fig. 43. For highly ionizing particles, light quenching has been included in the simulation using a Birk constant of 3.2e-3 g/(MeV cm<sup>2</sup>) (see Ref. [85]). A light emission yield of 50k  $\gamma$ /MeV, as reported by the BaBar Collaboration [40] and checked in Genova, and an attenuation length of  $\sim 60\text{cm}$ , as measured exposing the crystal to a focused proton beam (see Sec. B.6), have been used in the simulations. The absolute energy calibration has been obtained by matching the crossing muon Landau distribution to what obtained by the simulations. The resulting simulated signals measured by the two SiPMs are reported in Fig. 44

### B.2.2 The IV and OV response

Since a detailed description of the light collection in WLS fibers, transmission to the SiPM and coupling strongly depends on the manufacturing of the detector (groove polishing, fiber polishing, gluing ..), we decided to measure the response of the Inner Veto, parametrize it and implement it in the simulations. Figure 45 shows the position of the four fibers in the X-Y plane. Being the plastic transparent and the four grooves not optically separated, each SiPM is mainly sensitive to the area around the fiber but can also detect light produced farther. The combination (.OR.) of the four SiPM

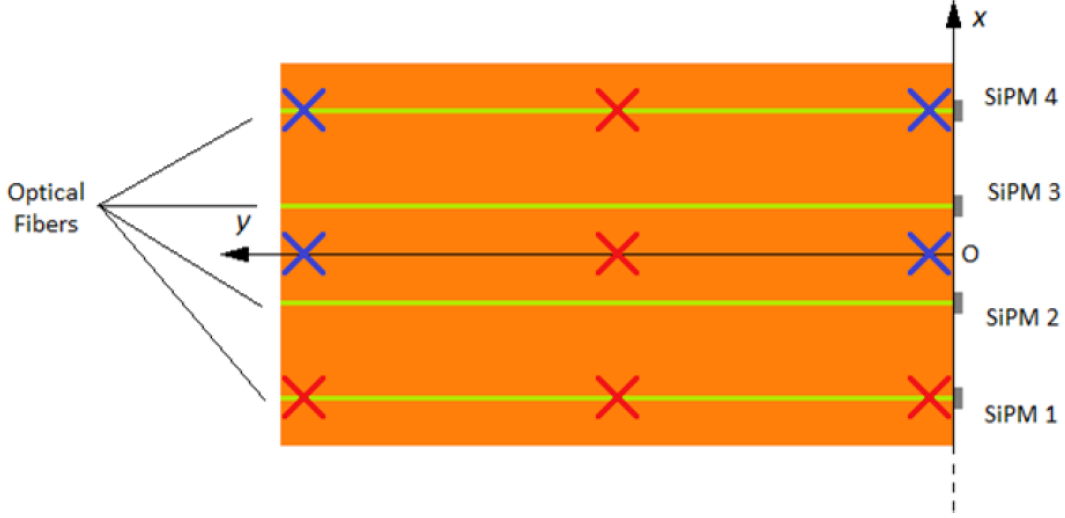


Figure 45: Position of the four fibers and SiPMs in the X-Y plane of an IV paddle.

signals strongly reduce the paddle inefficiency to a crossing particle since the four independent photo sensor are always involved. The  $N_{p.e.}$  response of each SiPM, for each paddle, as a function of the hit position has been measured, fitted to a polynomial function and included in the simulations. As an example, Fig. 46 shows the response of the first and the third SIPM of the TOP paddle. Similar results were obtained for the other paddles. The simulated response include the  $N_{p.e.}$  Poissonian statistics as well a Gaussian spread that has been derived by the shape of the measured Landau distributions for crossing cosmic muons.

Due to the more traditional technology used in the OV, plastic scintillator couple to a PMT via a plexiglas light guide, the response of the Outer Veto was parametrized using some standard techniques: plastic light yield, attenuation length, optical coupling, PMT quantum efficiency, ratio of the optical area. The results for crossing muons have been compared to measured distributions and the Landau peak positions adjusted to the data.

### B.3 The INFN-CT and LNS configurations

As mentioned at the beginning of this Section, we exposed the prototype to cosmic rays in two different experimental set up. The first set of data was taken with the prototype placed in a room on the last floor of the INFN-CT. The concrete roof was the only shielding present. We use this configuration as a benchmark to validate the model of the cosmic muons and cosmic neutrons implemented in the simulations. The



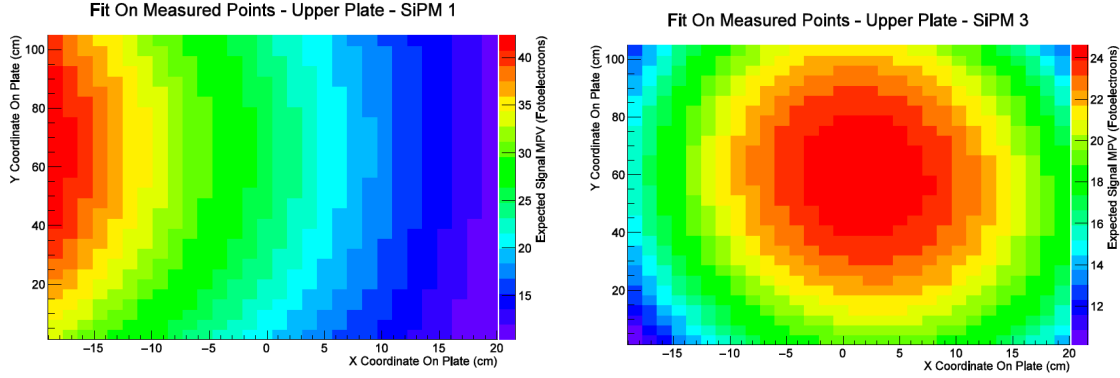


Figure 46: Response of SIPM 1 and 3 of the IV upper paddle. The SIPM is sensitive not only to the region in front of it but also to the all hit positions.

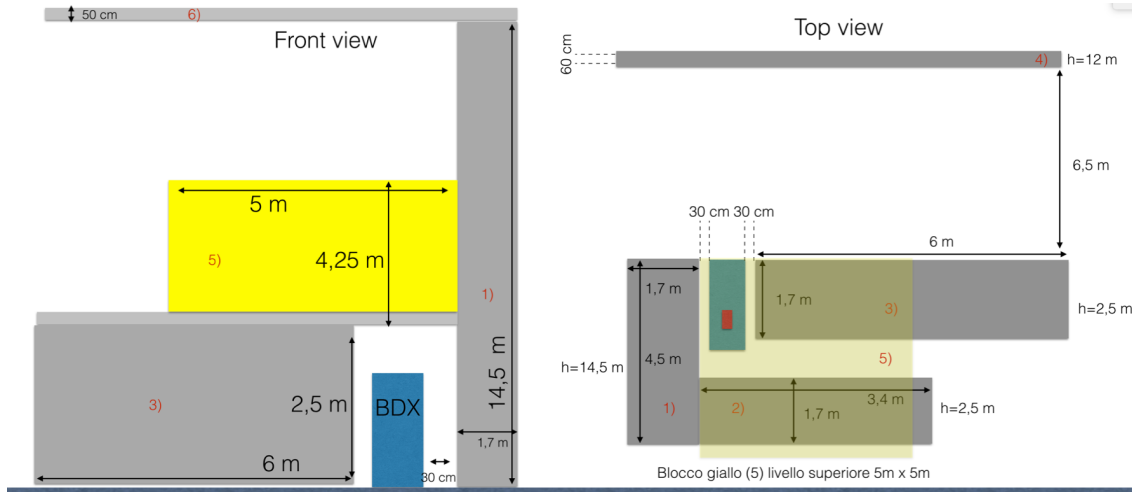


Figure 47: Front (left) and top (right) view of the LNS set up. The precise BDX prototype position is shown in the two drawings.

second, and current, set-up positioned the prototype in a bunker at LNS shielded by 470 cm of concrete walls. This configuration is very similar to the JLab overburden proposed for this experiment. Figure 47 shows the front and the top view of LNS set up. The two configurations were implemented in a simplified way into GEMC considering the detector located within a cube made of concrete 15 cm (470 cm) thick for the INFN-CT (LNS) configurations, respectively.

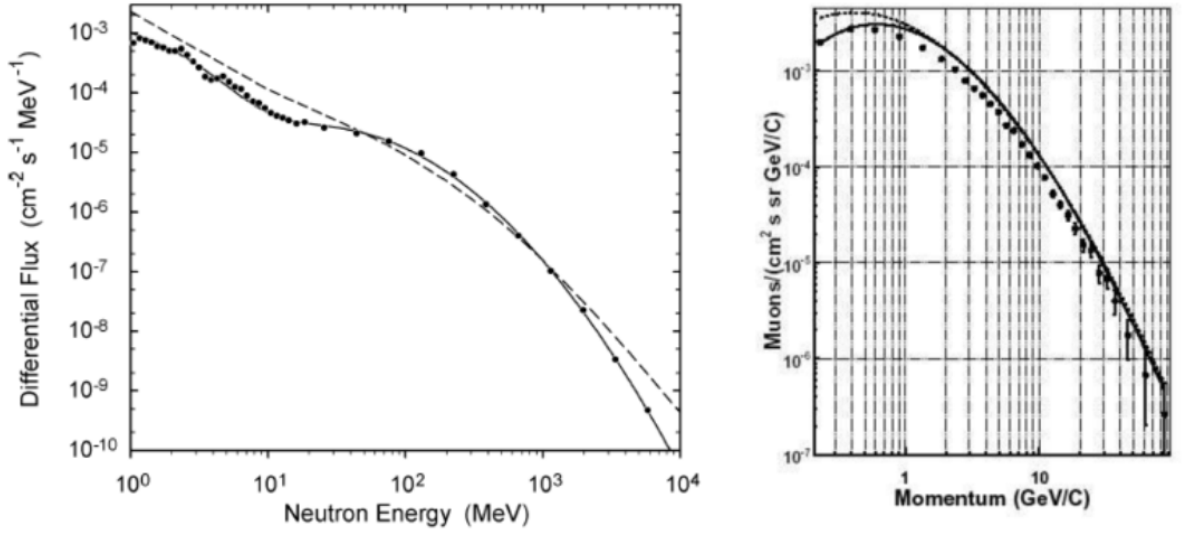


Figure 48: Flux of cosmic neutron (left) and muons (right).

#### B.4 Cosmic muons and cosmic neutrons

The cosmic muon and cosmic neutron energy spectra have been implemented directly in GEMC. For muons, we used the energy and angular distribution reported in Ref. [86], for neutrons the parametrization from Ref. [87, 88]. Fig. 48 shows the two energy spectra. Cosmic particles were generated in a fiducial volume big enough to contain the detector and a careful normalization has been performed to correctly take into account the crossing on the lateral sides (the correction with respect to a flat top surface is on the order, at most, of 20%, depending on the generation volume). Particles found to cross the fiducial volume where then projected far away and the production vertex extracted outside the shielding. This procedure is not completely correct for neutrons and low energy muons that may undergo a significant multiple scattering effect or produce other particles hitting the shielding and, indeed, not crossing any more the detector. This effect was corrected keeping the generation volume big enough to account for deviation in the trajectory and include contributions from secondary produced in the surrounding materials. The generation has been limited to the upper half of the solid angle, considering a null direct flux from the bottom (this does not prevent secondaries to bounce on the floor and enter in the fiducial volume).



## B.5 Results of cosmogenic background

The absolute rates of muons crossing the crystal considering different conditions on veto counters (no conditions, OV anti-coincidence, IV anti-coincidence) compare well (at level of 10%) to the experimental rates providing a validation of the simulations (for both the used cosmic spectra and the detector response). The remaining rate ( $\sim 1.8 \cdot 10^{-3}$  Hz for the LNS configuration, with 10 MeV threshold) measured by the crystal when both OV and IV are in anti-coincidence shows a significant difference indicating that a neutral component is present in the data and not fully understood<sup>†††</sup>. Nevertheless the good agreement obtained between simulations and data for crossing muons in different experimental conditions (INFN-CT and LNS) and the good agreement between simulated LNS and Jefferson Lab set up proof that experimental results obtained with the prototype at LNS can be safely extrapolated to the full detector in the JLab setup.

### B.5.1 Results from INFN-CT data

The first measurement campaign with the BDX-prototype has been conducted at INFN-CT, with the primary goal of measuring the absolute rates of muons crossing the crystal to compare it with simulations. Also, the simplified setup permitted to commission the detector before moving it to the final position at LNS, as well as to implement and validate the data-reconstruction framework. Data was measured in February - March 2016, for about 1 month of data-taking.

The following data-reconstruction procedure was adopted. For the CsI crystal, both waveforms were numerically integrated within a  $1 \mu\text{s}$  time windows to obtain the corresponding charge, that was then converted in MeV units by using calibration constants deduced from the cosmic-rays Landau distribution most probable value. In doing so, the following effect was observed: due to the long CsI scintillation decay time, events with low energy deposition (less than 10 MeV) could result in a signal with a rising edge not monotonic, but dominated by single phe signals. The trigger crossing time could thus be artificially delayed, due to the signal reaching the analog threshold later in time. This results in a time disalignment between the FADC sampling window and the veto signals, that are not recorded for these events. Therefore, particular care was taken in order to reject these cases from the analysis, by evaluating the CsI SiPM waveforms pedestal average and standard deviation, event by event, and comparing these with reference values. The fraction of rejected events is

---

<sup>†††</sup>The experimental rate of the crystal when both the OV and IV are put in anti-coincidence, does not scale as the product of the two separate OV and IV inefficiency as indicated by the simulation. We believe that a contribution from neutron or gamma, not correctly implemented or reproduced by the simulations, is responsible for this tiny but important contribution.

$\simeq 55\%$  for 10 MeV deposited energy, and flattens to  $\simeq 70\%$  at higher energies. All the event rates have been corrected for this effect.

For the inner-veto, after numerical integration, a tight coincidence cut (100 ns) was applied for SiPM signals referring to the same plastic scintillator counter, requiring a multiplicity equal or greater than two SiPMs. This permitted to use a very-low threshold (2.5 phe), while maintaining the contribution of thermal-induced signals negligible (the latter was evaluated by a random pulser trigger, and found to be less than 5%). For counters with single-SiPM readout, an higher threshold was applied (12.5 phe), resulting to the same thermal-induced signals contribution. For the outer-veto and for the two small inner paddles, each PMT signal was numerically integrated, and after this a 100 keV energy threshold was applied.

To evaluate the rate of cosmic muons crossing the crystal, the following events topologies were considered:

- All events
- Events with the Top and Bottom inner-veto counters in coincidence
- Events with the Top and Bottom outer-veto counters in coincidence
- Events with both inner-veto and outer-veto Top and Bottom counters in coincidence

For each topology, the CsI energy distribution of selected events was fitted with a Landau function convoluted with a Gaussian response, plus a proper background contribution. For the latter, different functional forms were employed for each topology (exponential, polynomial, ...). An example of fit is reported in Fig. 49. The expected rate was obtained by integrating the signal component, and then dividing by the corresponding measurement time. The same procedure was adopted for MC simulations. The most important uncertainty contribution to the results, reported in Table 6, is the systematic error in the background parametrization and in the fitting range. This has been evaluated to be of the order of 10 – 20%, depending on the considered topology.

### B.5.2 Results from LNS data

After commissioning the detector and validating MC results, the BDX-prototype was moved to the final position at LNS. Here, after repeating the cosmic ray measurement rate and comparing it again with simulations, absolute rates for different anti-coincidence configurations were measured, as a function of the deposited energy

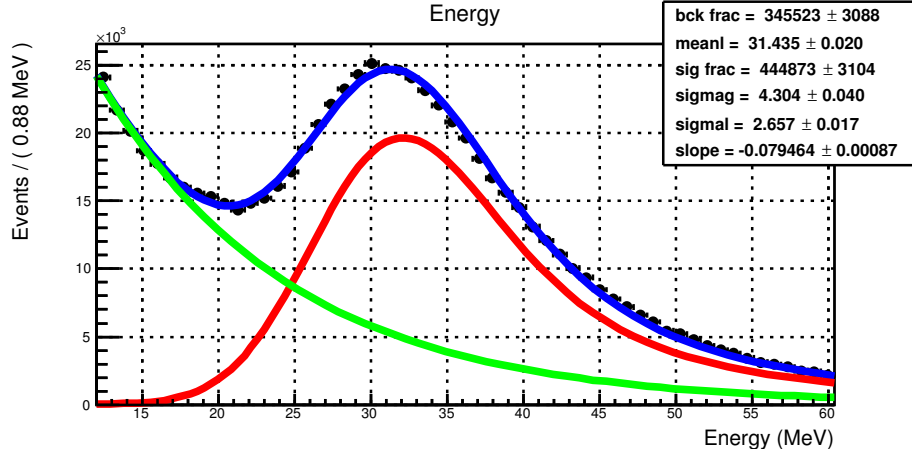


Figure 49: Example of a Maximum Likelihood fit to the CsI energy spectrum to measure the rate of cosmic muons crossing the crystal. The fit has been performed modeling the background (green) with an exponential function. The event yield has been obtained by integrating the signal (red) in the full energy range.

in the crystal. The results were then extrapolated to the full BDX detector configuration, as described in Sec. 4.4. The measurement campaign started in April 2016: the results here presented corresponds to about 1 month of data-taking.

The same event reconstruction procedure described in the previous section was adopted. We also excluded from the analysis events corresponding to periods with activity in one of the nearby LNS accelerators, as reported by the LNS RadCon service. A comparison of the measured rate in the BDX-detector with RadCon data is reported in Fig. 50: a clear rate enhancement correlated with accelerator activities is visible. Although one would expect that this events would result in a low ( $< 1$  MeV) energy deposition in the crystal, we saw contributions up to 10 MeV, hence the decision of excluding these periods from the data-analysis.

The following anti-coincidence configurations were considered. By “anti-coincidence” we mean that we selected events with no activity in any of the veto counters.

- Anti-coincidence with inner veto
- Anti-coincidence with outer veto
- Anti-coincidence with both veto systems

Preliminary studies with anti-coincidence with one of the veto systems, but a signal in the other system were also performed, in order to study the possible inefficiencies.

Results corresponding to the low-energy part of the CsI energy spectrum are shown in Fig. 51. The integrated rate, requiring the anti-coincidence with both veto

Event Topology	INFN-CT			LNS		
	Data rate	MC rate	Ratio	Data rate	MC rate	Ratio
All events	1.40 Hz	1.32 Hz	1.06	0.46 Hz	0.31 Hz	1.48
Inner-veto coincidence	1.11 Hz	1.38 Hz	0.80	0.36 Hz	0.37 Hz	0.97
Outer-veto coincidence	0.99 Hz	1.25 Hz	0.79	0.33 Hz	0.36 Hz	0.92
Both veto systems coincidence	0.95 Hz	1.24 Hz	0.77	0.32 Hz	0.36 Hz	0.89

Table 6: Comparison between the measured rate of cosmic muons crossing the CsI crystal, for different selection criteria, and the predictions from MC simulations, for both the INFN-CT and LNS measurement campaigns. The statistical error on the above results is negligible, compared to the systematic contribution, of the order of 10 – 20%, depending on the event topology.

Energy threshold	Measured rate
5 MeV	$(4.63 \pm 0.03) \cdot 10^{-2}$ Hz
10 MeV	$(1.88 \pm 0.05) \cdot 10^{-3}$ Hz
15 MeV	$(6.58 \pm 0.03) \cdot 10^{-4}$ Hz
20 MeV	$(3.67 \pm 0.02) \cdot 10^{-4}$ Hz

Table 7: The inner-veto and outer-veto anti-coincidence rate for the BDX-prototype, measured in the LNS configuration.

systems, for a 10 MeV (20 MeV) threshold, is 1.7 mHz (0.37 mHz) - after applying all the necessary corrections. Results are summarized in Table 7.

The analysis of the high-energy part of the spectrum ( $E > 100$  MeV) is, instead, more critical, due to the low statistics. In particular, for the accumulated statistics, corresponding to  $1.9 \cdot 10^6$  s of measurement, the following events were observed:

- Two events with  $E \simeq 500$  MeV, in anti-coincidence with the outer veto, but with an intense activity in the inner veto. One of these two events was measured in a period with a non-zero activity of the nearby accelerators.
- One event with  $E = 260$  MeV, with no activity in any veto. A deep scrutiny of this event (looking at the acquired waveforms) shows the following criticities: the signal decay time is a factor 2 shorter than the expected CsI value (500 ns vs  $1\mu\text{s}$ ), and the signal measured by the  $50\ \mu\text{m}$  SiPM is 98% lower - although

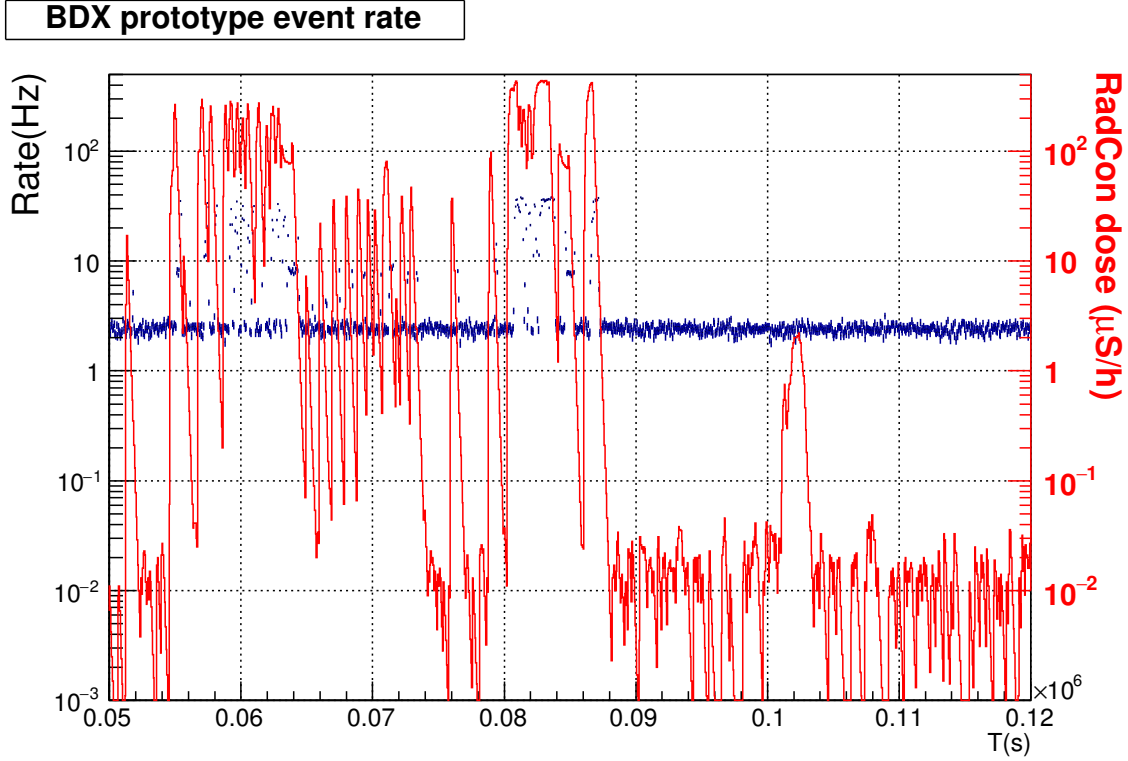


Figure 50: Comparison between the absolute event rate measured with the BDX prototype in the LNS configuration and the instantaneous dose measured close to the nearby accelerator, reported by the LNS RadCon, for a selected data-taking period. A clear correlation is visible. We also observed periods of significant accelerator activity with no corresponding increase in the overall event rate (for example, close to  $T = 0.1 \cdot 10^6$ s).

the corresponding PDE is about twice. Therefore, we decided to exclude this event from the analysis.

For the outer-veto anti-coincidence selection, the extrapolation of the single high-energy event (with  $E \simeq 500$  MeV, no activity in the outer veto, intense activity in the inner veto) to a final result is clearly problematic, and for the inner-veto anti-coincidence, with no measured events, the procedure is even more critical. Therefore, we decided to proceed as follows. We considered the lower part of the spectrum - where a significant statistics has been measured - and performed an extrapolation to the higher energy regime through a Maximum Likelihood fit, using an exponential function. The systematics associated with this procedure has been evaluated by changing the fit range and comparing the obtained results (see Fig. 52). Results are

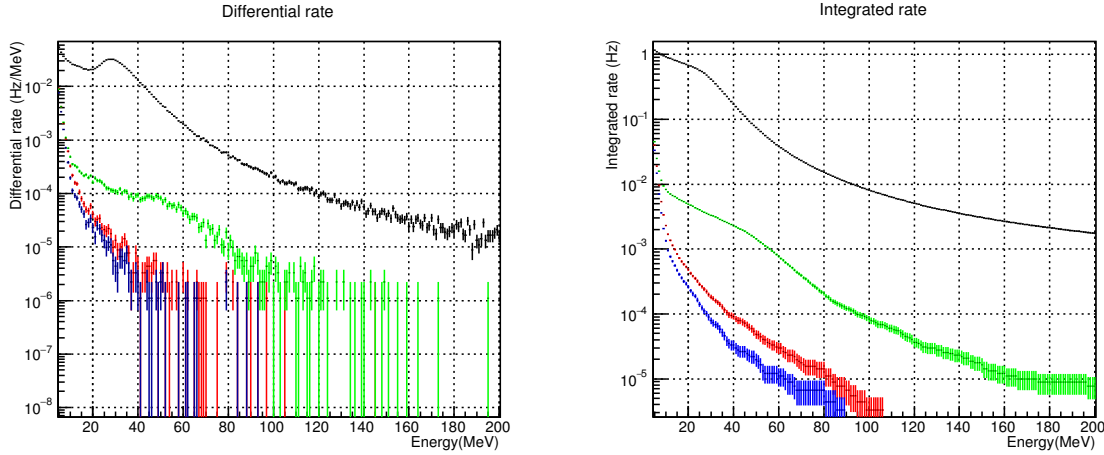


Figure 51: Left plot: the measured event rate as a function of deposited energy in the crystal. Different colors refer to the different anti-coincidence selections: black - all events, red - anti-coincidence with inner veto, green - anti-coincidence with outer veto, blue - anti-coincidence with both veto systems. Right plot: the integrated event rate as a function of the energy threshold (same color scheme).

reported in Tab. 8 for the inner-veto anti-coincidence selection and for different energy thresholds. In a conservative approach, the reported values refer to fit performed in the range 40 MeV - 150 MeV, resulting in the largest projection at high energy, and the quoted error is the RMS of the three results from fits performed starting from 20, 30, and 40 MeV. No higher ranges were considered for fitting, due to the lack of statistics.

## B.6 Results of on-beam measurements

The CsI(Tl) crystal was irradiated with mono-energetic protons of  $T_p$  24, 20, 18, 16, 14, 12, 10, 9, 8, 7, 6, 5, 4, 3 and 2.5 MeV. For each incident energy the beam was focused on 4 positions along the long side of the crystal. Each point was located at a different distance from the face hosting the two SiPM. For this purpose the long side of the crystal facing the beam was covered with a brass mask provided with four holes of 5mm of diameter located at 5, 12, 18.9 and 25.8 cm from the SiPMs. The 2 mm mask thickness prevents protons to hit the crystal out of the holes. For avoiding any possible energy loss, the measurement was performed inside a vacuum chamber. The beam was collimated by a 5 mm collimator, 60 cm long. The detector was placed on a moving plate which allowed to remotely center the beam on each hole. Two thermocouples have been used to monitor the SiPM temperature during the test.

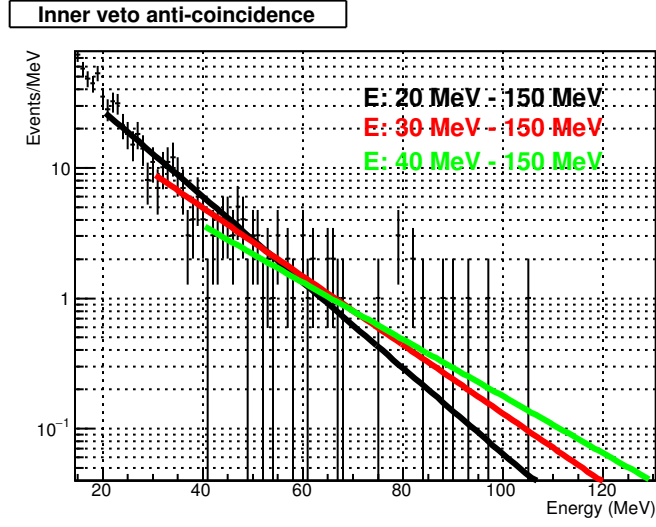


Figure 52: Extrapolation of the measured CsI energy spectrum in anti-coincidence with the inner veto from the low-energy region, where a non-zero event rate was measured, to the high energy region, where no events were detected. The three curves refer to Maximum Likelihood fits performed in different energy ranges.

Energy threshold	Extrapolated rate
200 MeV	$(3.6 \pm 1.5) \cdot 10^{-8}$ Hz
250 MeV	$(2.9 \pm 1.3) \cdot 10^{-9}$ Hz
300 MeV	$(2.4 \pm 1.1) \cdot 10^{-10}$ Hz
350 MeV	$(1.9 \pm 0.9) \cdot 10^{-12}$ Hz

Table 8: The inner-veto anti-coincidence rate for the BDX-prototype, measured in the LNS configuration, obtained by extrapolating from the low energy part of the spectrum.

The signal waveforms were digitized at 500 Msamples by a Lecroy WwaveRunner 620Zi oscilloscope. Fig. 53 shows two typical signals observed for protons of 24 and 2.5 MeV.

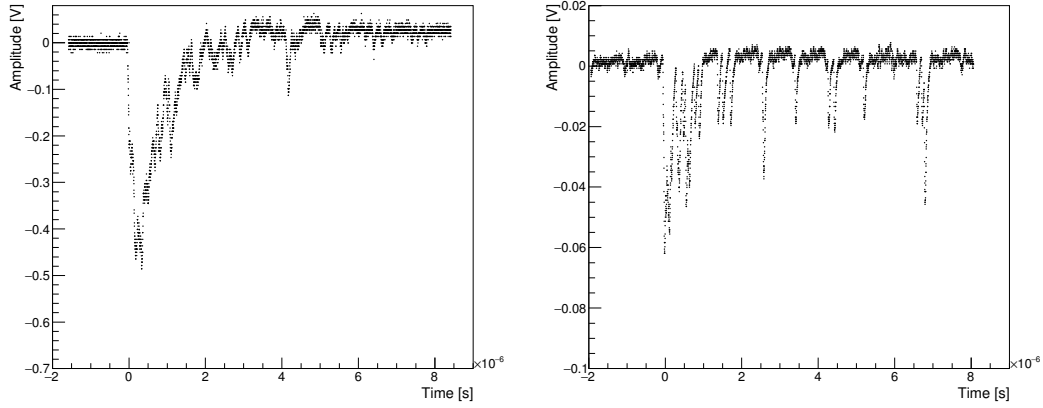


Figure 53: Signals generated by protons of 24 MeV (left) and 2.5 MeV (right) for the SiPM with a pixel size of  $25 \mu\text{m}$ .



Time jitter, calculated as the signal rise-time over the signal to noise ratio, is of the order of 1 ns for protons of 24 MeV, for both SiPMs. This result suggests that, despite the long scintillation time of the crystal (about 2-3  $\mu$ s), a few ns time coincidence is possible. Fig. 54 shows the number of p.e. collected by the two SiPMs as a function of the proton energy. The light quenching is correctly described by a Birk constant in the range of  $3.2 \times 10^{-3}$  g/(MeV cm<sup>2</sup>). The number of collected p.e. decreases linearly from 24 down to 2.5 MeV. It is worth noticing that protons of 2.5 MeV produce about 20 p.e. 25  $\mu$ m SiPM.

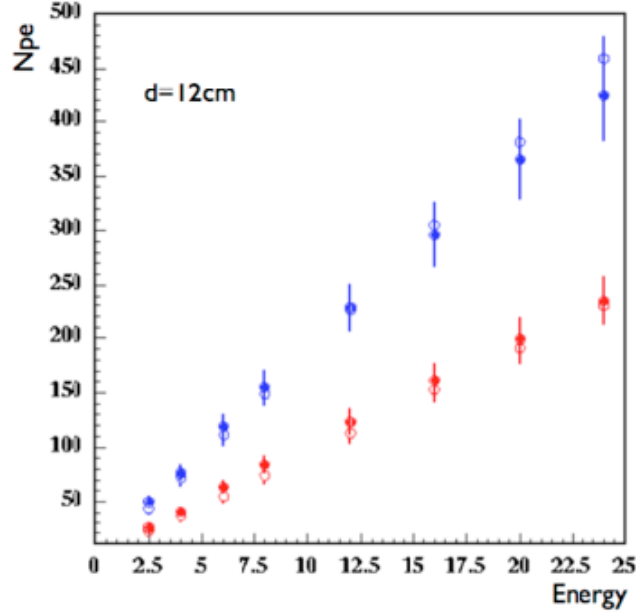


Figure 54: Number of detected p.e. as a function of the proton incident energy for the two SiPMs (full dots, blue for the 50  $\mu$ m and red for the 25  $\mu$ m pixel size). The beamSiPMs distance in this case was 12 cm. Empty dots represent the results of Monte Carlo simulations.

Fig. 55 shows the dependence of the relative energy resolution of the two SiPMs, defined as the FWHM over the mean value of the detected charge, as a function of the proton energy. As expected, resolution increases at higher energies reaching a value of  $\sim 15\%$ .

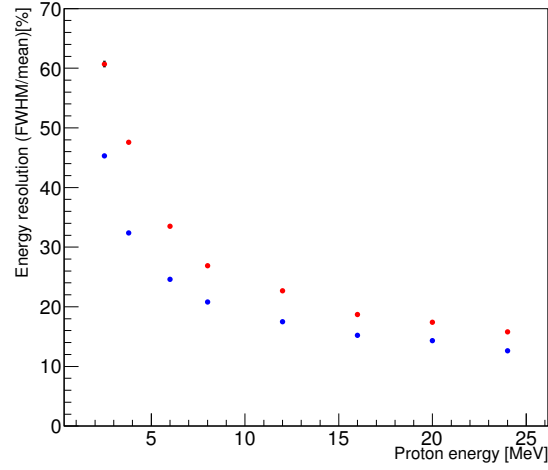


Figure 55: Relative energy resolution as a function of the proton incident energy for protons hitting the crystal at 12 cm from the SiPM. Blue dots refer to the 50  $\mu\text{m}$  SiPM and red dots to the 25  $\mu\text{m}$  one.

Fig. 56 shows, for protons of 24 MeV, the number of collected p.e. as a function of the distance between the SiPMs and the hit position. The behavior is well described by an exponential function with nearly the same attenuation length of about  $1/.016 \text{ cm}^{-1}$  ( $\sim 60 \text{ cm}$ ) for both SiPMs.

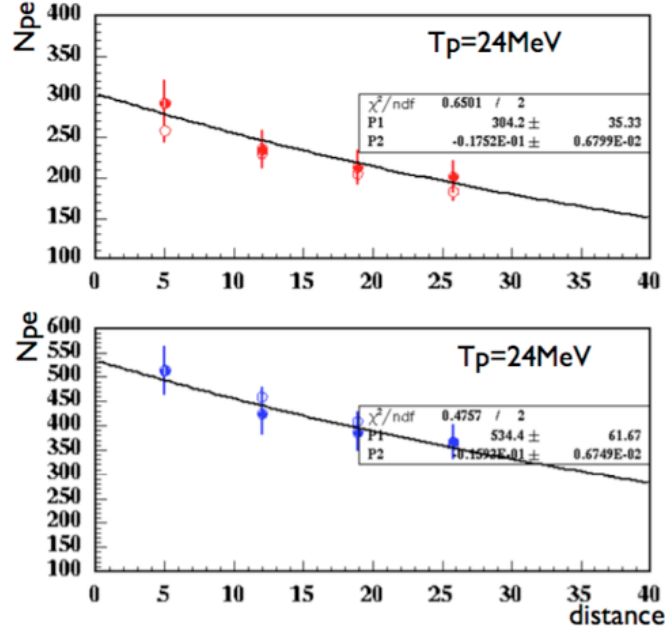


Figure 56: Number of detected photons as a function of the distance between the SiPMs and the point where the protons at 24 MeV hit the crystal, for the 50  $\mu\text{m}$  SiPM (top) and 25  $\mu\text{m}$  one (bottom). Empty dots represent the results of Monte Carlo simulations. The black line, for each SiPM, is the exponential function that best fit the data.

Notice that again a significant amount of p.e. is detected for protons of 2.5 MeV, even for those hitting the crystal at 25 cm from the SiPMs. These results prove the possibility of detecting low energy protons by using a large volume CsI(Tl) crystal coupled to the new readout based on small area SiPMs sensors. Figs. 54 and 56 show how data compare to GEANT4 Monte Carlo simulations (see Sec. B.2.1 for details). As it can be seen, the simulation well reproduces the number of p.e. as a function of both the proton energy and the incident position.

## C DRIFT-BDX

One of the advantages of a beam dump experiment is multiplicity. Having invested in shielding sufficient to block charged components and neutral hadronic components from entering the experimental hall behind the beam dump, multiple experiments can then look for a dark matter beam with high sensitivity. Because of the rare interaction rate these experiments can be stacked one behind the other. With the addition of the DRIFT-BDX detector, described below, the collaboration intends to take advantage of this feature and at the same time provide complementarity needed for a robust detection of dark sector dark matter. Specifically the addition of DRIFT-BDX will provide powerful cross-checks on backgrounds in the beam dump lab, utilizes a different physics channel for detecting dark sector dark matter and offers a powerful directional signature of dark matter recoils. Thus for marginal extra cost the DRIFT-BDX experiment adds much to the physics potential of this proposal.

### C.1 Capabilities

The Directional Recoil Identification From Tracks (DRIFT) project, with strong support from the NSF, has been in continuous development since 1998. The goal of the DRIFT collaboration is the detection of a directional signal from WIMP dark matter in our galaxy [89]. In order to accomplish this goal a unique, low-pressure, Negative Ion Time Projection Chamber (NITPC) technology has been developed [90]. The negative-ion drift allows DRIFT to have the lowest energy threshold and best inherent directionality of any limit-setting, directional, dark matter detector [91, 92]. In 2013 another feature of negative-ion drift was discovered paving the way for zero-background running of DRIFT [93]. As a consequence, DRIFTs sensitivity to dark matter, utilizing the current DRIFT-II detector in the Boulby Mine, is almost  $1,000\times$  better than the competitions [94]. With its unique directional and background rejection capabilities, the DRIFT NITPC technology is ideally suited to search for light dark matter at accelerators (LDMA). We propose to search for directional low-energy LDMA-induced, recoils utilizing the low-background NITPC technology developed for DRIFT. There is no other current dark sector experiment looking for dark matter via this coherent ( $Z^2$ ) channel.

### C.2 Detector

The design for the DRIFT-BDX detector is shown in Fig. 57. This design was developed based on our experience operating DRIFT; we know that such a design is feasible. The detector prototype would be 1 m long and 50 cm on a side filled with a mixture of 40 Torr  $\text{CS}_2$  and 1 Torr  $\text{O}_2$  and placed in the beamline, as shown. In the

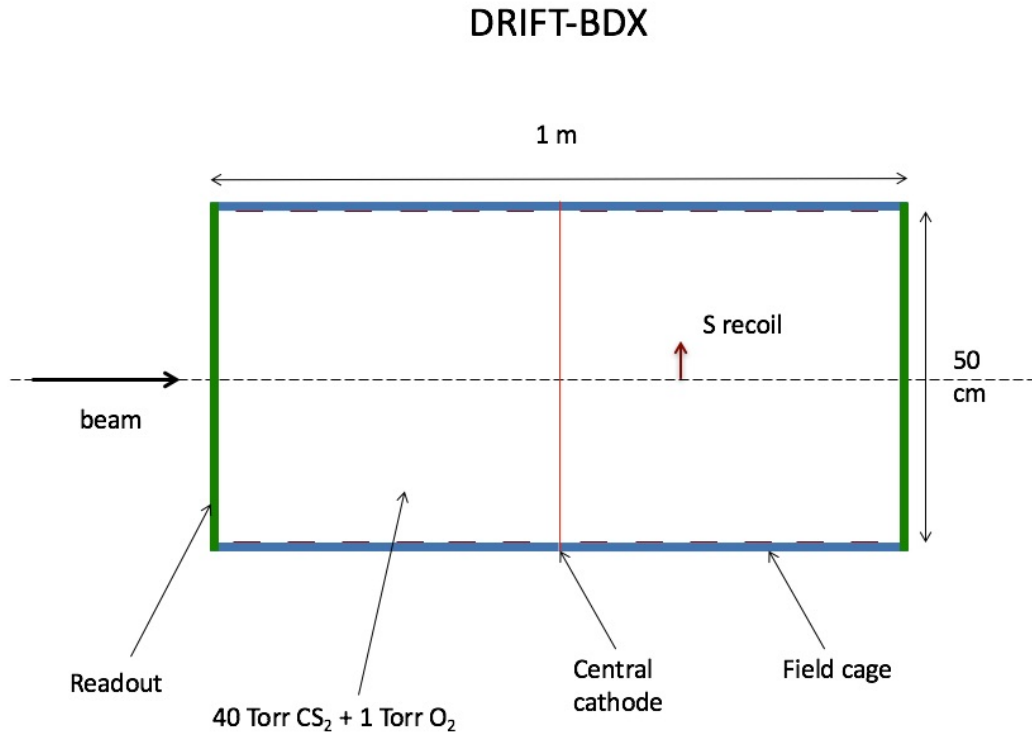


Figure 57: A schematic for the DRIFT-BDX experiment. Because of the prevalence of sulfur in the gas and the  $Z^2$  dependence for elastic, low-energy, coherent scattering, the recoils would be predominantly S.

event that this prototype can successfully be operated a larger, 10 m long detector could be made by replicating the 1 m long prototype 10 times.

The benefit of being able to detect 10-100 keV recoils is enormously enhanced sensitivity governed by the differential scattering cross section for coherent LDMA detection as shown in Eq. 38.

$$\frac{d\sigma}{dT} \approx \frac{8\pi\alpha\alpha_D\epsilon^2 Z^2 M}{(m_{A'}^2 + 2MT)^2} \quad (38)$$

where  $\alpha$  is the fine structure constant,  $\alpha_D$  is the dark sector fine structure constant,  $\epsilon$  is the coupling to the dark sector,  $Z$  is the charge of the nucleus,  $M$  is the mass of the nucleus,  $m_{A'}$  is the mass of the mediator and  $T$  is the kinetic energy of the recoil. Even for small thresholds the second term in the denominator tends to dominate so the full, coherent, scattering cross-section goes as  $\sim (1/T_{thresh})^3$ . With an order of magnitude, or more, lower threshold than other experiments this, alone, confers to DRIFT-BDX a huge increase in sensitivity. In addition because the momentum transfer is so small DRIFT-BDX can take full advantage of the  $Z^2$ , coherent, term in the numerator. These factors largely negate the density penalty for using a low-pressure gas detector. The limits achievable from DRIFT-BDX running in parallel with the BDX scintillator experiment are shown in Fig. 58. As can be seen the sensitivity of DRIFT-BDX is comparable to BDX.

### C.3 Backgrounds

Backgrounds in LDMA experiments are beam-related or beam-unrelated. The goal, as with the DRIFT experiment, is zero accepted background events. In the event that is not possible DRIFT-BDX has powerful signatures, discussed below, to pull signals out of the noise.

**Beam-related  $\nu$ s** Generically electron beam-dump experiments generate far fewer  $\nu$ s than proton beam-dump experiments [13]. The collaboration estimates  $\sim 10^{17}$  will be produced by  $10^{22}$  EOT. With a typical coherent, elastic scattering cross-section of  $10^{-39}$  cm<sup>2</sup> [95] a back-of-the-envelope calculation gives a background for DRIFT-BDX of  $\sim 0.03$  events. DRIFT-BDX will not observe backgrounds from coherent elastic neutrino-nucleus scattering in this experiment.

**Beam-related ns** It is difficult to simulate neutron backgrounds from  $10^{22}$  EOT. In the biggest GEANT simulation to date  $1.4 \times 10^9$  EOT produced no neutrons in the lab. Fortunately beam related neutrons were measured in the Stanford Linear Accelerator Center (SLAC) milliQ experiment [96]. In that experiment 29.5 GeV electrons produced muons in the beam dump which then came to rest

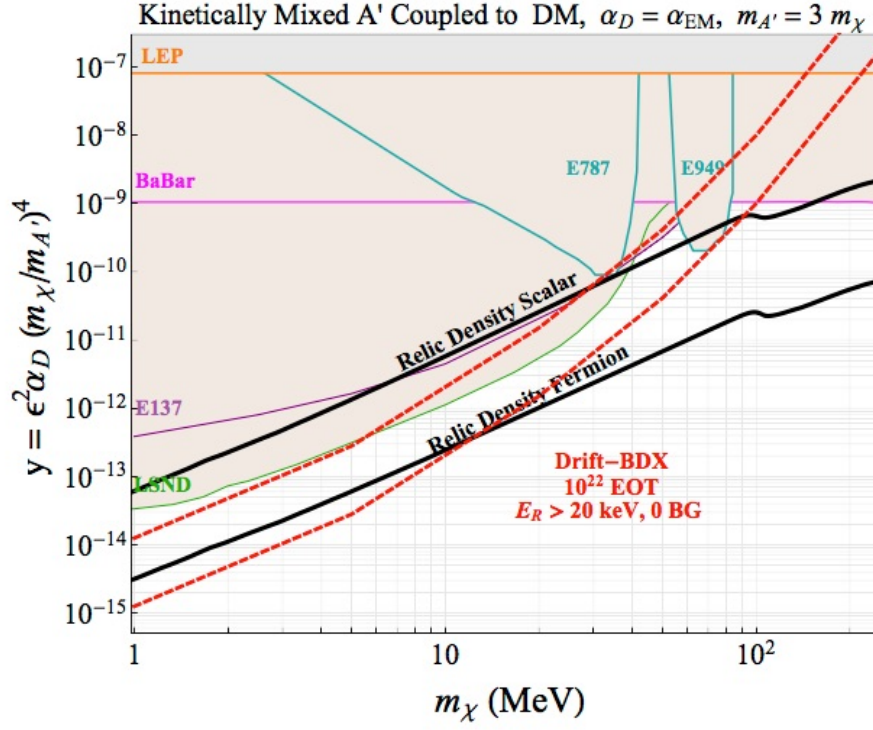


Figure 58: 90% C.L. exclusion bands for DRIFT-BDX shown in dashed red for a 1 m long DRIFT-BDX prototype detector, upper curve, and for a 10 m long detector, lower curve, in comparison with other limits.



in sandstone shielding, 5,000 g/cm<sup>2</sup> upstream of the detector. Neutron recoils were measured in the milliQ scintillators at a rate of 1 neutron recoil for every 10<sup>12</sup> EOT above a threshold of 20 keV proton recoil energy [97].

The current, preliminary design for the shielding has the muons ranging out 3300 g/cm<sup>2</sup> upstream of the detector though there is ample room to add the remaining 1700 g/cm<sup>2</sup> shielding. This calculation will assume the additional shielding. Scaling conservatively DRIFT-BDX could expect 400,000 neutron recoils from 10<sup>22</sup> EOT. GEANT-based simulations of neutron shielding for the DRIFT experiment we calculate that only 100 g/cm<sup>2</sup> of plastic shielding will be required to shield the DRIFT-BDX detector from beam-related neutron backgrounds.

This estimate is very conservative. The 29.5 GeV muons in the milliQ experiment would produce many more neutrons than the 11 GeV muons in the BDX JLab experiment. The beam overburden in the JLab experiment is significantly greater ( $\sim 1700$  g/cm<sup>2</sup> vs 1160 g/cm<sup>2</sup>) than for the SLAC milliQ experiment reducing neutron scatters in the atmosphere. And the milliQ detector had no overburden whereas DRIFT-BDX will have 1,000 g/cm<sup>2</sup> overburden. Finally the  $\sim 20$  keV proton-recoil threshold for the milliQ experiment corresponds to a  $\sim 5$  keV S recoil threshold for the DRIFT-BDX experiment after accounting for mass and quenching effects, far below the effective 20 keV S recoil threshold of DRIFT.

**Off-axis counting** Because  $\chi\bar{\chi}$  pairs are forward peaked (because of their small mass) and the proximity of the detector to the beam-dump, the event profile is expected to fall off rapidly from the beamline, especially at low masses. Backgrounds, however, are likely to be uniformly distributed. This will allow backgrounds to be measured and subtracted even for beam-related backgrounds.

**Beam-unrelated detector backgrounds** The underground operation of the DRIFT-II detector suggests that backgrounds from the detector are under control. In the strongest (unpublished) limit no events were observed in 55 live days of running at low threshold. Given the size difference between DRIFT-II and DRIFT-BDX this is equivalent to running DRIFT-BDX for 175 days background-free. This limit is expected to improve.

**Beam-unrelated neutrons** A DRIFT-BDX experiment run on the surface would be dominated by cosmic-ray neutron recoils. A GEANT-based simulation suggests 435 events per day above 20 keV. However DRIFT-BDX will be placed underground. An estimate made based on measurements done at almost identical depth [98] suggests that the flux of neutrons at the detector would be

approximately  $10\times$  less than the flux coming from the walls of the cavern. GEANT-based results give similar results. DRIFT has experience shielding neutrons coming from the walls. With only  $50\text{ g/cm}^2$  plastic shielding the 55 live day results suggest, for the same reasons as above, that DRIFT-BDX can run free from wall-neutron interactions in the fiducial volume of the detector for the requisite time. In this proposed experiment  $2\times$  this amount of shielding will be used to reduce beam-related neutrons to acceptable levels. Thus DRIFT-BDX will not be limited by cosmic-ray neutron recoils.

**Beam-unrelated muons** No reasonable amount of overhead shielding will reduce the flux of cosmic ray muons through the detector. However, the ionization density (due to the  $1/20$  atmosphere gas) of relativistic muons is  $350\times$  lower than a typical nuclear recoil. Thus unlike solid state detectors DRIFT-BDX can easily distinguish nuclear recoils from relativistic muons. In the event that muons are found to induce nuclear recoils, by muon induced neutrons inside the detector for instance, a muon veto will be considered.

**Beam-unrelated gammas** Gammas from the environment can Compton scatter in the gas of DRIFT-BDX and deposit ionization in magnitudes similar to nuclear recoils. However in a recent Co-60 exposure of DRIFT-IIId the equivalent of 24 live days of exposure of gammas from the walls of the underground lab was done and no events made it through the standard analysis. Gamma fluxes from shallow sites are thought to be equivalent to deep sites [99]. The size difference between DRIFT-IIId and DRIFT-BDX and the addition of shielding relative to the DRIFT-IIId experiment imply that beam-unrelated gammas will not affect DRIFT-BDX for the proposed experiment.

## C.4 Signature

Because of the prevalence of sulfur, S, in the gas and the  $Z^2$  dependence for elastic, low-energy, coherent scattering, the recoils would be predominantly S. The 10-100 keV S recoils produced by light dark matter would be scattered within a few degrees of perpendicular to the beam line due to extremely low momentum transfer scattering kinematics. The signature of light dark matter interactions, therefore, would be a population of S recoils with ionization parallel to the detector readout planes and uniformly oriented azimuthally. Straggling of recoils at these low energies is significant. Figure 48a shows the results of an SRIM [100] simulation of 1,000 50 keV S recoils oriented, originally, perpendicular to the beam, or  $z$ , or horizontal direction. As can be seen the signature, small dispersion in  $z$ , is degraded by straggling. In order to quantify the effect an assumption must be made about backgrounds. The

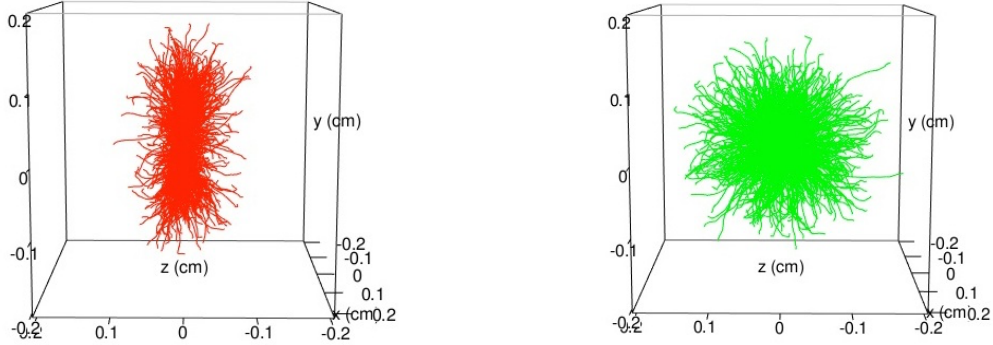


Figure 59: a) This figure shows the tracks produced by 1,000 50 keV S recoils originally oriented perpendicular to the beam or  $z$  axis according to an SRIM [100] simulation. b) This figure shows 1,000 50 keV S recoils oriented randomly as a comparison background.

simplest model for backgrounds is a uniform background. Fig. 59 shows an SRIM simulation of 1,000 50 keV S recoils oriented randomly. For each event, signal or background, the dispersion of the ionization of the track in  $z$ ,  $\sigma_z$ , was calculated. A simple Kolmogorov-Smirnov-based test then determined the number of signal events,  $N_s$ , required in the presence of a number,  $N_b$ , of background events for a 90% C.L. rejection of an isotropic background only. The results are shown in Fig. 60. The black curve in Fig. 60b shows  $N_s$  signal events required for a 90% C.L. detection in the presence of  $N_b$  background events for 50 keV S recoils. For zero-background 16 events would be required.

Thermal diffusion and various detector effects will contribute to the measured dispersion in  $z$  as discussed in Ref. [90]. The largest of these is thermal diffusion from a track 50 cm from the detector plane. Fortunately because the absolute position of the event,  $z$ , can be measured [93] this contribution to the measured dispersion can be subtracted in quadrature. We believe that various detector contributions can also be removed based on though the residual resolution, after subtraction, has yet to be fully characterized. As a result Figure 5 shows curves for 0 (black), 0.02 (green), and 0.05 (brown) cm residual resolution for 50 keV S recoils.

## C.5 Conclusion

The inclusion of the gas based DRIFT-BDX detector in the beamline with the scintillator based BDX experiment at JLab will allow for significantly enhanced capabilities. First both detectors are susceptible to different backgrounds with different thresholds

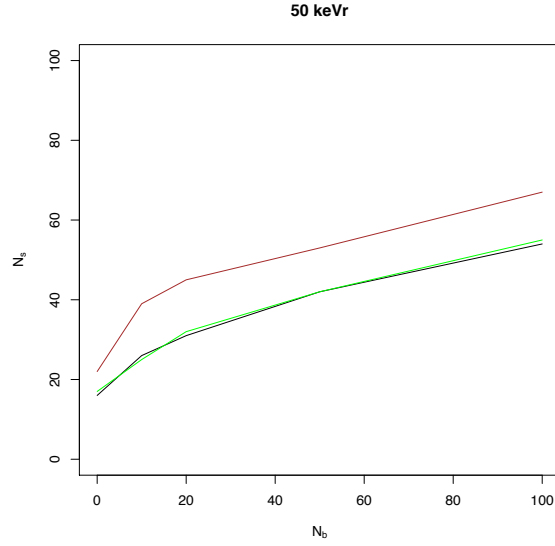


Figure 60: The figures above show the number of signal events,  $N_s$ , on the vertical axis required for a 90% C.L. detection in the presence of,  $N_b$ , background events for 50 keV S recoils. The black curve is for perfect detector residual resolution, see text. The green curve is are for a residual resolution of 0.02 cm. And the brown curve is for a residual resolution of 0.05 cm. For reference the range of a 50 keV S recoil in 40-1 Torr CS<sub>2</sub> O<sub>2</sub> is 0.086 cm.

allowing for a broader understanding of facility backgrounds. Second the sensitivity reach of the combined experiments will be significantly enhanced. And third, in the event of a detection DRIFT-BDX allows a powerful directional signature for verification.

## D Required equipment and future plans

In this section we report the list of the equipment required to run the BDX experiment, the future plans and possible improvement of the detector and data analysis.

### D.1 The BDX Collaboration

The BDX Collaboration is composed by more than hundred physicists from over seven countries in the World. It merges competences in scintillating and gaseous detector technology, high intensity, medium energy electron beam experiments and low energy proton/neutron detection. The BDX experimental program is supported by a strong theory group, whose leadership in the Light Dark Matter field is widely recognized. The BDX Collaboration is constantly in touch with the other Collaborations that are running or planning experiments to search for light dark matter with electron and proton beams: HPS, APEX, DarkLight, PADME, MMAPS, LDMX, NA64, MiniBoone. It is an active part and significant contributor of the rapidly growing Light Dark Matter search at Accelerator working group, organizing and participating to workshop conferences and common projects. The BDX *R&D* activity performed so far has been funded and supported by H2020-EU, INFN-Italy, DOE-US and NSF-US. Requests for grants have already been submitted to these and other (MIUR-Italy) funding agencies. If approved, the BDX Collaboration will be able to provide the necessary man power and seek for the necessary funds to target the experimental program described in this proposal.

### D.2 Required equipment

The most part of the equipment necessary to run the BDX experiment will be provided by the BDX Collaboration. The detector as well as the readout electronic will be assembled, tested and deployed at JLab by the BDX Collaboration requiring a minimal support from the lab. The Collaboration will be also responsible for detector maintenance and operation and data taking shifts. We rely on Jefferson Lab to build the new underground facility and instrument it with the necessary services (power, A/C, networking). JLab is also expected to be in charge of networking, data processing and storage as for the other experiments running in Hall A, B, C and D. Here below a summary of the different component of the BDX experiments.

#### **Detector: Calorimeter**

- CsI(Tl) crystals: provided by SLAC, refurbished and reassembled by the BDX Collaboration;

- Crystal readout: SIPM,  $6 \times 6 \text{ mm}^2$  area ,  $25 \mu\text{m}$  pixel size, to be procured by the BDX Collaboration;
- FE electronics: trans-impedance preamplifiers, to be procured by the BDX Collaboration;
- Services: LV, HV distribution, slow controls for SIPM to be procured by the BDX Collaboration;
- Mechanics: including crystal alveolus, supports, ..., to be provided by the BDX Collaboration.

#### **Detector: Vetos**

- Plastic scintillator: BC412 paddles 1 and 2 cm thick in various sizes, to be procured by the BDX Collaboration;
- Light guides: PMMA, tapered, to be procured and polished by the BDX Collaboration;
- WLS: Y-11, 1mm diameter, double cladding procured by the BDX Collaboration;
- Photomultipliers: 1 inch area , bialkali photocathode, to be procured by the BDX Collaboration;
- Photosensors: SIPM,  $3 \times 3 \text{ mm}^2$  area ,  $100 \mu\text{m}$  pixel size, to be procured by the BDX Collaboration ;
- FE electronics: trans-impedance preamplifiers, to be procured by the BDX Collaboration;
- services: LV/HV, slow controls for SIPM and PMTs to be procured by the BDX Collaboration;
- Mechanics: including support for PMTs and SIPM, walls, legs, ..., to be provided by the BDX Collaboration.

#### **Detector: Lead vault**

- lead bricks:  $20 \times 10 \times 5 \text{ cm}^3$  to be procured by the BDX Collaboration;

#### **Detector: DAQ**

- fADC: 250Mhz, 12 bit, 16 ch to be procured by the BDX Collaboration;

- Trigger: VTP boards to be procured by the BDX Collaboration;
- Other: VME-VXS crates, on-board CPU, workstations to be procured by the BDX Collaboration.

### **Data storage and data analysis Lab**

- Networking: fast connection between the Computer Center and the new facility to be provided by JLab;
- Data processing:  $8 \cdot 10^6$  CPU hours (single core) required to filter and process raw data, and run Monte Carlo simulations, to be provided by JLab;
- Data storage: 600 TB of permanent storage (tape) and 100 TB of disk space for raw, reconstructed and simulated data.

### **Beam dump facility**

- New underground beam-dump lab: including all necessary services to be provided by JLab;
- Shielding: iron, concrete and dirt to be provided by JLab.

## **D.3 Further improvements and tests**

Results show that, running at JLab high intensity Hall A beam-dump, it is possible to explore a wide range of model parameters. We believe that there is still room for improvement in the detector concept, active veto and shielding design. Moreover, the expected low counting rate coupled with the signal digitization of fADCs will allow us to optimize the off-line reconstruction algorithms, further enhancing the rejection capability.

In deriving the sensitivity curves we always applied a conservative approach. Here below is a list of items we are currently investigating or we are planning to implement in an upgraded version of the prototype and MC simulations:

### **Cosmogenic background**

- the cosmogenic background was evaluated scaling the single-crystal rate measured in the LNS set-up to a full detector: we are assembling a matrix of 4x5 BaBar crystals CsI(Tl) to obtain more accurate and realistic information about the possible correlations of inter-crystals rates;

- we are planning to continue the LNS prototype measurement campaign with the crystal matrix. A long statistics run ( $\sim 6$  months) will provide insight on high energy events ( $E_{seed} > 300$  MeV) for a safer extrapolation to JLab set up;
- the internal lead shielding could be further optimized changing thickness and number of layers, if necessary, and the effect of adding a further layer of an active inner veto is under investigation with both MC simulations and prototyping;
- the JLab overburden described in the proposal was chosen to mimic LNS conditions and provide a validated upper limit on cosmogenic rates in the detector: there is still some room for further optimization (e.g. replacing the dirt with concrete or heavier material or accumulating more dirt on top of the beam-dump facility); a more effective shielding will be studied by MC simulation and validated with measurement locating the prototype in a similar configuration at LNS;
- we are investigating the possibility of running the CEBAF machine with a beam macro-structure of  $1\mu s$  and keeping the bunch micro-structure of 250 MHz; if a charge per bunch of 1.3 pC (the same configuration of G0 experiment) would be possible, we could achieve a factor of 5 of cosmic background rejection; this would imply to run in dedicated-mode, whose compatibility with the Hall-A current physics program should be checked;.

### **Beam-related background**

- a thorough scrutiny of how hadronic processes contributing to the predicted neutrino flux are implemented in GEANT4 is underway;
- a detailed implementation of the  $\nu_e$ -nucleon scattering in the detector is being implemented for a precise evaluation of the electromagnetic shower induced by the  $\nu$ -N CC interaction;
- the use of other simulation tools, such as MCNP or FLUKA, may provide a more reliable treatment of the predicted low-energy background (gamma and neutrons); in addition, these tools, providing a statistical description rather than a particle-by-particle tracking, are better suited to deal with the large number of the EOT expected in BDX and, indeed, requiring a more limited extrapolation.

### **Signal optimization and data analysis**

- no directionality or other signal/background discriminating cuts, such as time correlation between veto and calorimeter or crystal multiplicity in the calorimeter, have been applied yet in the data analysis; we expect that the information



collected by the different sub-components of the BDX detectors will provide further discriminating power between signal and background;

- the effect of limiting the signal detection to a inner fiducial volume by exploiting the calorimeter segmentation and using the last layer of crystals as an additional veto is currently being studied by MC simulations;
- keeping the number of crystals compatible with the BaBar ECal end cap supply, changing the geometrical arrangement of the crystal array is under study;

The proposed BDX experiment, tacking advantage of the high intensity, high energy electron beam available at JLab has the unique capability of extending the possible reach by an order of magnitude with respect to the previous (un-optimised) measurements getting close to the unreducible background due to the neutrinos produced in the beam-dump interaction. The BDX experiment at Jlab may represent the ultimate beam-dump experiment with an intense electron beam challenging a wide category of light DM models.

## E Cover letter for BDX proposal submission to PAC44

This Proposal follows the Letter of Intent LOI-12-14-006 *Dark matter search in a Beam-Dump eXperiment (BDX) at Jefferson Lab* presented to PAC42 in 2014.

The recommendations included in the PAC42 Final Report document read as follow:

**“Summary and Recommendation:**BDX could become the definitive beam dump experiment at electron accelerators. Sited at Jefferson Lab, it would use the CEBAF high intensity beam and modern technologies for detector design, trigger, and data acquisition, to achieve the most stringent limits (or to make the first discovery) of a class of dark matter particles. The collaboration is encouraged to proceed with a full proposal to the laboratory, but the PAC emphasizes that the collaboration needs to meet a high standard in order to be eventually approved. Experimentally, a fully fleshed-out detector design needs to be presented, including both simulations and measurements (with CORMORINO or otherwise) that demonstrate its sensitivity to both detection channels as well as its ability to reject cosmic ray backgrounds with whatever necessary overburden. Theoretically, it must be made clear what models and attendant assumptions motivate this particular measurement, as well as the extent to which these models are (or are not) addressed in other experiments at other laboratories. Finally, the PAC realizes that the infrastructure costs to build and instrument a pit that would house this experiment will be extensive, and recommends that the laboratory require an approved proposal before scheduling onsite tests with beam as part of the design process.

Finally, we comment that BDX would obviously benefit from a low duty factor beam, as opposed to that provided by CEBAF, if a suitable high energy, high intensity accelerator could be identified.”

The BDX Collaboration believes that this proposal addressed all the concerns following the recommendations expressed by the PAC42:

- the theoretical motivation have been revised based on two-years of rapid evolution in the field: the thermal target is clearly indicated as a reasonable, well motivated, limit that BDX will be able to reach (at least for the *Relic density Scalar* scenario);
- we investigated options for beam dump experiments at other electron-beam facilities, including DESY, Frascati, Mainz and SLAC, and only JLab has the energy, high current, practical access and beam availability for this program;
- the growing activity at proton machines (FNAL and CERN) as well as other

experiments planned at electron/positron accelerator facilities (SLAC, Cornell and LNF) have been mapped and demonstrate that, due to the unique combination of high energy and intensity, BDX at JLab represents one of the best options for dark matter (DM) searches in beam-dump experiments;

- a full model of DM production in the beam dump, that realistically includes the effects of the electromagnetic shower formation, has been developed based on the state-of-the art tools (MADGRAPH and GEANT4);
- the BDX detector has been fully fleshed out: the core of the detector is an electromagnetic calorimeter that reuses the scintillating CsI(Tl) crystals formerly used in BaBar Ecal with a modern readout based on SIPMs and fADCs; active and passive vetos complement the calorimeter by reducing and/or vetoing cosmic background;
- a detector prototype has been built and has been running for several months under experimental conditions similar to those expected at JLab; the measured cosmic rates were extrapolated to the JLab configuration providing a solid, although conservative, basis for the expected beam unrelated backgrounds in the detector;
- full GEANT4 simulations of the detector, the beam dump, the new underground facility and the shielding have been validated with real data down to a detected energy of few MeV, and used to predict the beam-related background and the expected signal produced by DM interactions;
- the reach of the proposed experiment, for some of the predicted DM interaction processes, is only limited by the irreducible background (Charged Current  $\nu_e$  interaction) showing that BDX at Jefferson Lab represents the ultimate beam-dump experiment with intense electron beams;
- the concern related to the extensive infrastructure costs to build and instrument a new underground facility for this and other beam-dump experiments, has been addressed by providing a realistic and detailed quote that includes not only the construction but also instrumentation and services.

## References

- [1] Benjamin W. Lee and Steven Weinberg. Cosmological lower bound on heavy-neutrino masses. *Phys. Rev. Lett.*, 39:165–168, Jul 1977. [10](#)
- [2] Bob Holdom. Two U(1)’s and Epsilon Charge Shifts. *Phys. Lett.*, B166:196–198, 1986. [10](#), [69](#), [76](#)
- [3] Eder Izaguirre, Gordan Krnjaic, Philip Schuster, and Natalia Toro. Analyzing the Discovery Potential for Light Dark Matter. *Phys. Rev. Lett.*, 115(25):251301, 2015. [13](#), [18](#)
- [4] Maxim Pospelov. Particle physics catalysis of thermal Big Bang Nucleosynthesis. *Phys. Rev. Lett.*, 98:231301, 2007. [14](#)
- [5] Douglas P. Finkbeiner, Silvia Galli, Tongyan Lin, and Tracy R. Slatyer. Searching for Dark Matter in the CMB: A Compact Parameterization of Energy Injection from New Physics. *Phys. Rev.*, D85:043522, 2012. [18](#), [78](#)
- [6] Tongyan Lin, Hai-Bo Yu, and Kathryn M. Zurek. On Symmetric and Asymmetric Light Dark Matter. *Phys. Rev.*, D85:063503, 2012. [18](#), [78](#)
- [7] Silvia Galli, Fabio Iocco, Gianfranco Bertone, and Alessandro Melchiorri. Updated CMB constraints on Dark Matter annihilation cross-sections. *Phys.Rev.*, D84:027302, 2011. [18](#)
- [8] Mathew S. Madhavacheril, Neelima Sehgal, and Tracy R. Slatyer. Current Dark Matter Annihilation Constraints from CMB and Low-Redshift Data. *Phys.Rev.*, D89:103508, 2014. [18](#)
- [9] P.A.R. Ade et al. Planck 2013 results. XVI. Cosmological parameters. *Astron.Astrophys.*, 571:A16, 2014. [18](#)
- [10] P. A. R. Ade et al. Planck 2015 results. XIII. Cosmological parameters. 2015. [19](#), [70](#), [71](#)
- [11] Kenneth M. Nollett and Gary Steigman. BBN And The CMB Constrain Light, Electromagnetically Coupled WIMPs. *Phys. Rev.*, D89(8):083508, 2014. [19](#)
- [12] Bernard Aubert et al. Search for Invisible Decays of a Light Scalar in Radiative Transitions  $\nu_{3S} \rightarrow \gamma A_0$ . 2008. [19](#)
- [13] Eder Izaguirre, Gordan Krnjaic, Philip Schuster, and Natalia Toro. New Electron Beam-Dump Experiments to Search for MeV to few-GeV Dark Matter. *Phys. Rev.*, D88:114015, 2013. [19](#), [22](#), [45](#), [46](#), [105](#)

- [14] Rouven Essig, Jeremy Mardon, Michele Papucci, Tomer Volansky, and Yi-Ming Zhong. Constraining Light Dark Matter with Low-Energy  $e^+e^-$  Colliders. *JHEP*, 1311:167, 2013. [19](#)
- [15] Anson Hook, Eder Izaguirre, and Jay G. Wacker. Model Independent Bounds on Kinetic Mixing. *Adv.High Energy Phys.*, 2011:859762, 2011. [20](#)
- [16] David Curtin, Rouven Essig, Stefania Gori, and Jessie Shelton. Illuminating Dark Photons with High-Energy Colliders. *JHEP*, 1502:157, 2015. [20](#)
- [17] Vardan Khachatryan et al. Search for dark matter, extra dimensions, and unparticles in monojet events in protonproton collisions at  $\sqrt{s} = 8$  TeV. *Eur. Phys. J.*, C75(5):235, 2015. [20](#), [72](#)
- [18] James D. Bjorken, Rouven Essig, Philip Schuster, and Natalia Toro. New Fixed-Target Experiments to Search for Dark Gauge Forces. *Phys. Rev.*, D80:075018, 2009. [20](#)
- [19] Rouven Essig, Philip Schuster, Natalia Toro, and Bogdan Wojtsekhowski. An Electron Fixed Target Experiment to Search for a New Vector Boson  $A'$  Decaying to  $e^+e^-$ . *JHEP*, 02:009, 2011. [20](#)
- [20] M. Battaglieri et al. The Heavy Photon Search Test Detector. *Nucl. Instrum. Meth.*, A777:91–101, 2015. [20](#)
- [21] J. Balewski et al. The DarkLight Experiment: A Precision Search for New Physics at Low Energies. 2014. [20](#)
- [22] Eder Izaguirre, Gordan Krnjaic, Philip Schuster, and Natalia Toro. Physics motivation for a pilot dark matter search at Jefferson Laboratory. *Phys. Rev.*, D90(1):014052, 2014. [20](#), [22](#), [45](#)
- [23] S. Andreas et al. Proposal for an Experiment to Search for Light Dark Matter at the SPS. 2013. [20](#)
- [24] S. N. Gninenko. Search for MeV dark photons in a light-shining-through-walls experiment at CERN. *Phys. Rev.*, D89(7):075008, 2014. [20](#)
- [25] Mauro Raggi and Venelin Kozhuharov. Proposal to Search for a Dark Photon in Positron on Target Collisions at DAΦNE Linac. *Adv. High Energy Phys.*, 2014:959802, 2014. [21](#)
- [26] Mauro Raggi, Venelin Kozhuharov, and P. Valente. The PADME experiment at LNF. *EPJ Web Conf.*, 96:01025, 2015. [21](#)

- [27] G. Angloher et al. Results on light dark matter particles with a low-threshold CRESST-II detector. 2015. [21](#)
- [28] Rouven Essig, Aaron Manalaysay, Jeremy Mardon, Peter Sorensen, and Tomer Volansky. First Direct Detection Limits on sub-GeV Dark Matter from XENON10. *Phys. Rev. Lett.*, 109:021301, 2012. [21](#)
- [29] Rouven Essig, Marivi Fernandez-Serra, Jeremy Mardon, Adrian Soto, Tomer Volansky, and Tien-Tien Yu. Direct Detection of sub-GeV Dark Matter with Semiconductor Targets. 2015. [21](#)
- [30] Brian Batell, Maxim Pospelov, and Adam Ritz. Exploring Portals to a Hidden Sector Through Fixed Targets. *Phys. Rev.*, D80:095024, 2009. [21](#)
- [31] Patrick deNiverville, Maxim Pospelov, and Adam Ritz. Observing a light dark matter beam with neutrino experiments. *Phys. Rev.*, D84:075020, 2011. [21](#)
- [32] Patrick deNiverville, David McKeen, and Adam Ritz. Signatures of sub-GeV dark matter beams at neutrino experiments. *Phys. Rev.*, D86:035022, 2012. [21](#)
- [33] R. Dharmapalan et al. Low Mass WIMP Searches with a Neutrino Experiment: A Proposal for Further MiniBooNE Running. 2012. [21](#), [22](#)
- [34] Rouven Essig et al. Working Group Report: New Light Weakly Coupled Particles. In *Community Summer Study 2013: Snowmass on the Mississippi (CSS2013) Minneapolis, MN, USA, July 29-August 6, 2013*, 2013. [21](#)
- [35] L. B. Auerbach et al. Measurement of electron - neutrino - electron elastic scattering. *Phys. Rev.*, D63:112001, 2001. [21](#)
- [36] Miriam D. Diamond and Philip Schuster. Searching for Light Dark Matter with the SLAC Millicharge Experiment. *Phys. Rev. Lett.*, 111(22):221803, 2013. [22](#)
- [37] J. D. Bjorken, S. Ecklund, W. R. Nelson, A. Abashian, C. Church, B. Lu, L. W. Mo, T. A. Nunamaker, and P. Rassmann. Search for Neutral Metastable Penetrating Particles Produced in the SLAC Beam Dump. *Phys. Rev.*, D38:3375, 1988. [22](#)
- [38] Brian Batell, Rouven Essig, and Ze’ev Surujon. Strong Constraints on Sub-GeV Dark Sectors from SLAC Beam Dump E137. *Phys. Rev. Lett.*, 113(17):171802, 2014. [22](#), [45](#)

- [39] Na64 collaboration. <https://na64.web.cern.ch/content/visible-and-invisible-decays-dark-photons>. Accessed: 2016-05-26. 24
- [40] Bernard Aubert et al. The BaBar detector. *Nucl.Instrum.Meth.*, A479:1–116, 2002. <http://arxiv.org/abs/hep-ex/0105044>. 28, 37, 87
- [41] W.Wisniewski. Private Communication. 28
- [42] J. Brose, G. Dahlinger, and Klaus R. Schubert. Properties of CsI(Tl) crystals and their optimization for calorimetry of high-energy photons. *Nucl. Instrum. Meth.*, A417:311–324, 1998. 28
- [43] A.Freyberger. Private Communication. 30
- [44] H. Dong et al. Integrated tests of a high speed vxs switch card and 250 msp/s flash adcs. In *2007 IEEE Nuclear Science Symposium Conference Record*, volume 1, pages 831–833, Oct 2007. 32
- [45] C. Cuevas. Private Communication. 33
- [46] D. Lawrence. Multi-threaded event reconstruction with jana. *Journal of Physics: Conference Series*, 119(4):042018, 2008. 35
- [47] E.S. Smith. Reference Concepts for BDX. Technical Report BDX-NOTE-2015-001, Jefferson Lab, April 2015. <https://wiki.ge.infn.it/hps/index.php/BDX>. 36, 38
- [48] E.S. Smith. Civil Reference C1 for BDX. Technical Report BDX-NOTE-2015-002, Jefferson Lab, April 2015. <https://wiki.ge.infn.it/hps/index.php/BDX>. 36
- [49] M. Battaglieri et al. Dark matter search in a Beam-Dump eXperiment (BDX) at Jefferson Lab. 2014. 36
- [50] S.J. Freedman et al. Limits on neutrino oscillations from anti-electron-neutrino appearance. *Phys.Rev.*, D47:811–829, 1993. 37
- [51] Ungaro, M. CLAS12 GEANT4 Simulation Package GEMC, 2016. <http://gemc.jlab.org>. 44
- [52] Johan Alwall, Pavel Demin, Simon de Visscher, Rikkert Frederix, Michel Herquet, et al. MadGraph/MadEvent v4: The New Web Generation. *JHEP*, 0709:028, 2007. 45

- [53] Kwang Je Kim and Yung-Su Tsai. Improved Weizsacker-Williams Method and Its Application to Lepton and W-Boson Pair Production. *Phys. Rev. D*, 8:3109–3125, Nov 1973. 45
- [54] J. A. Formaggio and G. P. Zeller. From eV to EeV: Neutrino cross sections across energy scales. *Rev. Mod. Phys.*, 84:1307, 2012. 52
- [55] Hooman Davoudiasl and William J. Marciano. Running of the U(1) coupling in the dark sector. *Phys. Rev.*, D92(3):035008, 2015. 64
- [56] K. A. Olive et al. Review of Particle Physics. *Chin. Phys.*, C38:090001, 2014. 70
- [57] David E. Morrissey and Michael J. Ramsey-Musolf. Electroweak baryogenesis. *New J. Phys.*, 14:125003, 2012. 70
- [58] Mario Mateo. Dwarf galaxies of the Local Group. *Ann. Rev. Astron. Astrophys.*, 36:435–506, 1998. 70
- [59] Kim Griest and Marc Kamionkowski. Unitarity Limits on the Mass and Radius of Dark Matter Particles. *Phys. Rev. Lett.*, 64:615, 1990. 70, 71
- [60] Annika H. G. Peter. Dark Matter: A Brief Review. 2012. 71
- [61] Gerard Jungman, Marc Kamionkowski, and Kim Griest. Supersymmetric dark matter. *Phys. Rept.*, 267:195–373, 1996. 71
- [62] Gordan Krnjaic and Kris Sigurdson. Big Bang Darkleosynthesis. *Phys. Lett.*, B751:464–468, 2015. 71
- [63] Savas Dimopoulos and Howard Georgi. Softly Broken Supersymmetry and SU(5). *Nucl. Phys.*, B193:150–162, 1981. 72
- [64] David B. Kaplan and Howard Georgi. SU(2) x U(1) Breaking by Vacuum Misalignment. *Phys. Lett.*, B136:183–186, 1984. 72
- [65] David B. Kaplan, Howard Georgi, and Savas Dimopoulos. Composite Higgs Scalars. *Phys. Lett.*, B136:187–190, 1984. 72
- [66] Howard Georgi and David B. Kaplan. Composite Higgs and Custodial SU(2). *Phys. Lett.*, B145:216–220, 1984. 72
- [67] Michael J. Dugan, Howard Georgi, and David B. Kaplan. Anatomy of a Composite Higgs Model. *Nucl. Phys.*, B254:299–326, 1985. 72



- [68] Z. Chacko, Hock-Seng Goh, and Roni Harnik. The Twin Higgs: Natural electroweak breaking from mirror symmetry. *Phys. Rev. Lett.*, 96:231802, 2006. 72
- [69] Nima Arkani-Hamed, Savas Dimopoulos, and G. R. Dvali. The Hierarchy problem and new dimensions at a millimeter. *Phys. Lett.*, B429:263–272, 1998. 72
- [70] Lisa Randall and Raman Sundrum. A Large mass hierarchy from a small extra dimension. *Phys. Rev. Lett.*, 83:3370–3373, 1999. 72
- [71] D. S. Akerib et al. First results from the LUX dark matter experiment at the Sanford Underground Research Facility. *Phys. Rev. Lett.*, 112:091303, 2014. 72
- [72] E. Aprile et al. Dark Matter Results from 225 Live Days of XENON100 Data. *Phys. Rev. Lett.*, 109:181301, 2012. 72
- [73] Z. Ahmed et al. Dark Matter Search Results from the CDMS II Experiment. *Science*, 327:1619–1621, 2010. 72
- [74] Elena Aprile. The XENON1T Dark Matter Search Experiment. *Springer Proc. Phys.*, 148:93–96, 2013. 72
- [75] D. S. Akerib et al. LUX-ZEPLIN (LZ) Conceptual Design Report. 2015. 72
- [76] Laura Baudis. DARWIN: dark matter WIMP search with noble liquids. *J. Phys. Conf. Ser.*, 375:012028, 2012. 72
- [77] M. Ackermann et al. Constraining Dark Matter Models from a Combined Analysis of Milky Way Satellites with the Fermi Large Area Telescope. *Phys. Rev. Lett.*, 107:241302, 2011. 72
- [78] Georges Aad et al. Search for dark matter candidates and large extra dimensions in events with a jet and missing transverse momentum with the ATLAS detector. *JHEP*, 04:075, 2013. 72
- [79] Scott Dodelson and Lawrence M. Widrow. Sterile-neutrinos as dark matter. *Phys. Rev. Lett.*, 72:17–20, 1994. 74
- [80] Jonathan L. Feng. Dark Matter Candidates from Particle Physics and Methods of Detection. *Ann. Rev. Astron. Astrophys.*, 48:495–545, 2010. 74
- [81] Maxim Pospelov, Adam Ritz, and Mikhail B. Voloshin. Secluded WIMP Dark Matter. *Phys. Lett.*, B662:53–61, 2008. 74

- [82] Gordan Krnjaic. Probing Light Thermal Dark-Matter With a Higgs Portal Mediator. 2015. [76](#)
- [83] David Tucker-Smith and Neal Weiner. Inelastic dark matter. *Phys. Rev.*, D64:043502, 2001. [79](#)
- [84] E.Rauly. Private Communication. [83](#)
- [85] V. I. Tretyak. Semi-empirical calculation of quenching factors for ions in scintillators. *Astropart. Phys.*, 33:40–53, 2010. [87](#)
- [86] I. C. Appleton, M. T. Hogue, and B. C. Rastin. A study of the muon momentum spectrum and positive-negative ratio at sea-level. *Nucl. Phys.*, B26:365–389, 1971. [90](#)
- [87] M. S. Gordon et al. Measurement of the flux and energy spectrum of cosmic-ray induced neutrons on the ground. *IEEE Transactions on Nuclear Science*, 51(6):3427–3434, Dec 2004. [90](#)
- [88] M. S. Gordon et al. Correction to #8220 ”Measurement of the Flux and Energy Spectrum of Cosmic-Ray Induced Neutrons on the Ground”. *IEEE Transactions on Nuclear Science*, 52(6):2703–2703, Dec 2005. [90](#)
- [89] D. P. Snowden-Ifft, C. J. Martoff, and J. M. Burwell. Low pressure negative ion time projection chamber for dark matter search. *Phys. Rev. D*, 61:101301, Apr 2000. [103](#)
- [90] D. P. Snowden-Ifft and J.-L. Gauvreau. High precision measurements of carbon disulfide negative ion mobility and diffusion. *Review of Scientific Instruments*, 84(5), 2013. [103](#), [109](#)
- [91] S. Burgos et al. Measurement of the range component directional signature in a drift-ii detector using 252cf neutrons. *Nucl. Instr. and Meth. A*, 600(2):417 – 423, 2009. [103](#)
- [92] S. Burgos et al. First measurement of the headtail directional nuclear recoil signature at energies relevant to {WIMP} dark matter searches. *Astroparticle Physics*, 31(4):261 – 266, 2009. [103](#)
- [93] Daniel P. Snowden-Ifft. Discovery of multiple, ionization-created cs2 anions and a new mode of operation for drift chambers. *Review of Scientific Instruments*, 85(1), 2014. [103](#), [109](#)

- [94] J.B.R. Battat et al. First background-free limit from a directional dark matter experiment: results from a fully fiducialised {DRIFT} detector. *Physics of the Dark Universe*, 910:1 – 7, 2015. 103
- [95] Kate Scholberg. Prospects for measuring coherent neutrino-nucleus elastic scattering at a stopped-pion neutrino source. *Phys. Rev. D*, 73:033005, Feb 2006. 105
- [96] A. A. Prinz. The search for millicharged particles at slac. *SLAC Report*, 569, 2001. 105
- [97] M. Diamond and P. Schuster. Searching for light dark matter with the slac millicharge experiment. *Phys. Rev. Lett.*, 111:221803, Nov 2013. 107
- [98] A. Da Silva, B. Pritychenko, B.L. Dougherty, M. Gray, A. Lu, A. Smith, D.S. Akerib, D. Bauer, B. Cabrera, D.O. Caldwell, R.E. Lanou, B. Sadoulet, and S. Yellin. Neutron background for a dark matter experiment at a shallow depth site. *Nucl. Instr. and Meth. A*, 354(23):553 – 559, 1995. 107
- [99] P. Theodrsso. *Measurement of Weak Radioactivity*. World Scientific, New Jersey, 1996. 108
- [100] J.F. Ziegler, Biersack J.P, and U. Littmark. *The Stopping and Range of Ions in Solids vol. 1 of series Stopping and Ranges of Ions in Matter*. Pergamon Press, New York, 1984. 108, 109